

STUDY OF IMPURITY-HELIUM CONDENSATES FORMED BY MULTISHELL
NANOCLUSTERS

A Dissertation

by

SHUN MAO

Submitted to the Office of Graduate and Professional Studies of
Texas A&M University
in partial fulfillment of the requirements for the degree of

DOCTOR OF PHILOSOPHY

Chair of Committee,	David M. Lee
Committee Members,	Glenn Agnolet
	Vitaly Kocharovsky
	Hilty Christian
Head of Department,	George R. Welch

December 2014

Major Subject: Physics

Copyright 2014 Copyright Shun Mao

ABSTRACT

Impurity-helium condensates (IHCs) are porous gel-like materials created by injecting a mixed beam of helium gas and an impurity gas into superfluid ^4He . Van der Waals forces lead to the formation of clusters of impurities each surrounded by a thin layer of solid helium. Inside superfluid helium the clusters tend to aggregate into a gel-like structure with wide distribution of pore sizes. Matrix isolation of free radical impurities in IHCs leads to unusually high concentrations of these impurities.

Impurity-helium condensates (IHCs) containing nitrogen and krypton atoms immersed in superfluid ^4He have been studied via a CW electron spin resonance (ESR) technique. It was found that the addition of krypton atoms to the nitrogen-helium gas mixture used for preparation of IHCs increases efficiency of stabilization of nitrogen atoms. We have achieved high average ($5 \times 10^{19} \text{ cm}^{-3}$) and local ($2 \times 10^{21} \text{ cm}^{-3}$) concentrations of nitrogen atoms in krypton-nitrogen-helium condensates. High concentrations of nitrogen atoms achieved in IHCs provide an important step in the search for magnetic ordering effects at low temperatures.

Impurity-helium condensates created by injection of hydrogen (deuterium) atoms and molecules as well as rare gas (RG) atoms (Ne and Kr) into superfluid ^4He also have been studied via electron spin resonance (ESR) techniques. Measurements of the ground-state spectroscopic parameters of hydrogen and deuterium atoms show that the nanoclusters have a shell structure. H and D atoms reside in solid molecular layers of H_2 and D_2 , respectively. By monitoring the recombination of H atoms in the collection of hydrogen-neon nanoclusters, we show that nanoclusters form a gel-like porous structure which enables the H atoms to be transported through the structure via percolation. Observation of percolation in the collection of nanoclusters containing stabilized hydrogen atoms opens new possibilities for a search for macroscopic collective quantum phenomena at ultralow temperatures accessible by a dilution refrigerator.

DEDICATION

To my parents.
For their love and care.

ACKNOWLEDGEMENTS

This dissertation is a culmination of a perfect working relationship with my supervisor, David M. Lee, to whom I am eternally grateful. Dave brought me to the group and provided unreserved support during my PhD and generously paved the way for my development as a research scientist as well as a person. I have learned a great many from his humbleness and passion in both physics and life. In my eyes, he is always one of the greatest mentors and friends one can ever have in his life. My second supervisor, Vladimir Khmelenko, is a great person and experimental physicist, who generously taught me so many great experimental skills and techniques. It is he who helped me form the structure and framework of low temperature experimental physics. Also, Volodya is a true friend, who can give me honest advice on anything I request. I deeply thank him for being a good advisor and a great companion in the past four years. He and Dave always cared for me and made me feel this is my second family .

I also want to express my sincere gratitude to my colleagues. Patrick McColgan is a very helpful and diligent fellow, who is the first colleague I met when I came into the group. He contributed so much to the construction of the lab and always had a very good knowledge of all types of equipment. He is also very kind and willing to teach me whatever he knows. Without him, our lab would not have progressed so fast. I consider him to be one of my best friends. Trevor Dragon is a nice young undergraduate and very passionate on whatever he is told to do. I thank him for helping us build the ortho-para converter and some other experimental setups. Adil Meraki came a little later into the lab but soon got involved in all of the research projects. He is always kind and hard working. He generously gave me help whenever I requested it. I deeply thank him for helping me and accompanying me in almost every experiment.

The machine shop staff, Tom Weimer, Kevin Morris and Garrick Garza are continuously giving us advice and help on the construction. I learned many useful machining

skills from them and I think it will benefit me a life long. Steve Payne in the electronic shop is also a very helpful technician, who fixed the LR400 for us, thus making my life a lot easier. Also, I want to express my gratitude to the entire staff in the physics department. They took care of all the purchasing and transactions from our lab and did many tedious documentation work for us. Particularly, I thank Sandy and Sherree for giving me advice and help on my degree and graduation.

I am deeply grateful to my family for the love and support I have always received. All my friends, my life would have been incomplete without you! At Texas A&M I met a lot of people from physics department as well as other departments. For those who are still here as well as who already left for another place, I thank you for being my companion in these five years.

And finally, I want to thank my beloved wife Yan Wang for her love and encouragement during these years. Without her, my life would not have been so happy and colorful.

TABLE OF CONTENTS

	Page
ABSTRACT	ii
DEDICATION	iii
ACKNOWLEDGEMENTS	iv
TABLE OF CONTENTS	vi
LIST OF FIGURES	viii
LIST OF TABLES	x
1 INTRODUCTION	1
2 EXPERIMENTAL SETUP	6
2.1 Overall scheme of the setup	6
2.1.1 Janis helium-4 cryostat	8
2.1.2 Description of the homemade insert and sample preparation	9
2.1.3 System for ESR registration	13
2.1.4 System for optical registration	16
2.2 How does continuous ESR work	21
3 ESR STUDIES OF NITROGEN ATOMS STABILIZED IN AGGREGATES OF RG-N ₂ NANOCLOUDS IMMERSED IN SUPERFLUID HELIUM	22
3.1 Introduction	22
3.2 Theoretical background	24
3.2.1 Hyperfine structure of nitrogen atom	24
3.2.2 The origin of hyperfine splitting	27
3.2.3 Matrix effects	29
3.2.4 Dipolar broadening	30
3.2.5 Spin pair radicals	31
3.3 Experimental results	31
3.3.1 IHCs with N ₂ /Kr/He mixtures	31
3.3.2 Simultaneous registration of ESR and optical spectra of N(⁴ S) atoms during warming up of N-N ₂ -Kr-He samples	44
3.3.3 Optical spectra during final destruction of the sample	48
3.3.4 IHCs with N ₂ /Xe/He mixtures	50
3.4 Discussion and conclusion	56

4	PERCOLATION IN AGGREGATES OF NANOCLUSTERS IMMERSSED IN SUPERFLUID HELIUM	60
4.1	Introduction	60
4.2	Theoretical background	62
4.2.1	Hyperfine structure of hydrogen atom	63
4.2.2	Dipolar coupling of hydrogen electron and neighboring nuclei . . .	67
4.2.3	Quantum exchange chemical reactions	70
4.3	Experimental results	72
4.3.1	Studies of condensates formed by H-H ₂ -Ne-He nanoclusters	72
4.3.2	Studies of condensates containing alternate layers of D-D ₂ -He and H ₂ -RG-He nanoclusters	83
4.4	Discussion	92
4.5	Conclusions	98
	REFERENCES	100

LIST OF FIGURES

	Page
1.1 Structure of IHCs	2
2.1 Block diagram of the experimental setup	7
2.2 Low temperature insert for VTI used in the ESR investigation of IHCs . . .	10
2.3 ESR cavity	12
2.4 Microwave magnetic field distribution in the ESR cavity	14
2.5 Scheme for collection of luminescence from the sample inside ESR cavity . .	17
2.6 Quantum efficiency for Newton EMCCD camera	19
2.7 ESR signal modulation scheme	20
3.1 Energy diagram of N atoms in 4S ground state	26
3.2 ESR spectra of N atoms in an as-prepared sample	32
3.3 ESR spectra of N atoms in as-prepared N-N ₂ -Kr-He samples prepared from different gas mixtures.	34
3.4 Dependence of average concentration of N atoms stabilized in nitrogen- krypton-helium samples on the ratio of N ₂ /Kr in various gas mixtures. . . .	35
3.5 ESR spectra of spin pair radicals.	35
3.6 Dependence of average concentration of N atoms on the temperature for different samples.	36
3.7 Transformation of ESR spectra of nitrogen atoms stabilized in samples pre- pared with gas mixture N ₂ /Kr/He=1/2/600.	38
3.8 Decomposition of the ESR spectra.	42
3.9 Simultaneous measurement of ESR and optical spectra.	45
3.10 Optical spectrum during warming up of the sample.	46
3.11 Dynamic of ESR spectra of N atoms in N-N ₂ -Kr-He sample during warming.	47
3.12 Dynamics of the sample emission during explosive destruction.	49
3.13 ESR spectra of N(4S) atoms in nanoclusters prepared by different mixtures.	51

3.14	Decomposition of ESR spectra for sample $\text{N}_2/\text{Xe}/\text{He}=1/1/400$	54
3.15	Structure of nitrogen-krypton-helium nanoclusters with stabilized N atoms. .	58
4.1	Transitions between hydrogen hyperfine levels calculated from Fermi golden rule.	65
4.2	Energy spectrum of nucleus-electron pair of spins $1/2$ in a high field coupled by dipole-dipole interaction.	66
4.3	The position of the samples in the beaker and the structure of the samples. .	71
4.4	The ESR spectra of H atoms in sample A1	73
4.5	The dependence of the average concentration of H atoms and its reciprocal on time.	76
4.6	Dependence of ESR signal linewidths of H atoms on time	79
4.7	Two possible cases for collection of nanoclusters immersed in bulk superfluid helium.	82
4.8	The time dependence of average concentration of D atoms and H atoms in sample series B.	86
4.9	The time dependence of linewidth of D atoms and H atoms in sample series B.	89

LIST OF TABLES

	Page
3.1 Hyperfine structure constants, A, g factors, ΔH_{pp} , and local concentrations for N atoms in N/Kr/He condensates.	39
3.2 Hyperfine structure constants, A, and g factors for N atoms in N ₂ and Kr matrices.	41
3.3 Average concentration of N atoms in different N/N ₂ /Xe samples.	52
3.4 Analysis of ESR spectra of N atoms for different N/N ₂ /Xe samples.	55
4.1 Rate constants k for atom exchange reactions calculated by Takayanagi and Sato.	69
4.2 The recombination rate of H atoms for the three different H-H ₂ -Ne-He samples.	77
4.3 Hyperfine structure constants, A, and g-factors of H atoms in H-H ₂ -Ne-He samples, in the gas phase, in solid H ₂ and in Ne matrices.	80
4.4 Concentration and rate constants of sample series B.	84
4.5 Hyperfine structure constants, A, and g-factors for ESR spectra of H and D atoms in different environments.	87
4.6 Average Concentrations of H and D atoms before and after annealing of the samples B1 and B3.	90

1. INTRODUCTION

Impurity-helium condensates (IHCs) are porous gel-like materials created by injecting a mixed beam of helium gas and an impurity gas into superfluid ^4He by means of a method first introduced in 1974.[1] Van der Waals forces lead to the formation of clusters of impurities each surrounded by a thin layer of solid helium (see figure 1.1). Inside superfluid helium the clusters tend to aggregate into a gel-like structure with wide distribution of pore sizes.[2, 3, 4] Matrix isolation of free radical impurities in IHCs leads to unusually high concentrations of these impurities. IHCs have been attracting increasing interest in recent years as new porous nanomaterials became available, whose unique properties can be used for various purposes. For example, it has been proposed to use IHCs prepared from D_2 and D_2O impurities as moderators for obtaining ultracold neutrons.[5] Another promising practical application of condensates is for polarization of D_2 , and Xe nuclei in a strong magnetic field ~ 10 T at a temperature of ~ 1 mK.[6, 7] An additional application of IHCs, which has been the most important from the start, is the creation of new cryogenic materials with a high specific energy,[8] since record high concentrations of stabilized deuterium and nitrogen atoms have been achieved in IHCs.[9, 10] Other possible applications of IHCs include investigations of the unique properties of superfluid ^3He and ^4He in disordered porous materials,[11] determination of the rate constants of exchange tunneling chemical reactions, studies of atomic diffusion in disordered structures, research on quantum phenomena in condensates with high densities of stabilized hydrogen atoms and investigations of the magnetic and electronic properties of nanoclusters.[12]

The technique of IHC preparation is based on the injection of gas mixtures of helium and impurities into bulk superfluid helium (HeII).[1] In order to create samples containing high concentrations of atomic free radicals corresponding to high specific energy samples, the gas mixture is passed through a radio-frequency (rf) discharge zone

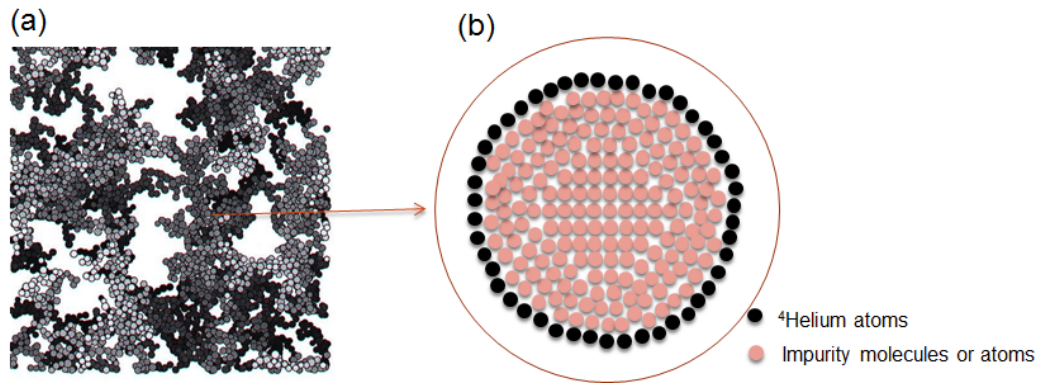


Figure 1.1: Structure of IHCs. a) The macroscopic view of IHC sample in which the "empty" space is filled with superfluid helium, b) Magnified view of each nanocluster in the sample.

which permits the accumulation of free radicals in the ensemble of nanoclusters forming impurity-helium samples. IHC samples can be made from a variety of atomic and molecular impurities: Ne, Ar, Kr, D₂, N₂, O₂, H₂O, C₂H₅OH, Ba and Na.[13, 14, 15, 16] IHCs are porous gel-like structures formed by impurity clusters with different sizes 3-10 nm and a low average concentration of the impurity substance $\sim 10^{20} \text{ cm}^{-3}$. [9, 17, 4] The skeleton of impurity material is formed in superfluid helium, and the sample usually remains stable even after the helium has evaporated (in this case we regard it as a dry sample) at higher temperatures. Studies of the relative (elemental) composition of helium and the various impurities in dry impurity-helium samples have shown for example, that there are on the order of 20 helium atoms for every Ne atom and N₂ molecule and 30-60 helium atoms for each Ar and Kr atom,[18, 19, 20] i.e., the samples consist mainly of solidified helium plus the remaining liquid helium in the pores. Thus IHCs are highly porous materials with a wide distribution of pore sizes (from 10 to 1000 nm) and an extremely large specific surface area.[3]

Various techniques such as optical spectroscopy,[21, 22, 23, 24] electron spin resonance (ESR),[25, 26, 27] x ray diffraction[4, 9, 17, 28, 29] and ultrasound[3, 4, 30] have been applied to characterize these samples and to determine why free radical stabilization in IHCs was so effective. Among these techniques, optical spectroscopy and ESR have been most significant for obtaining information about the properties of IHCs prepared with different impurities and many new effects have been revealed. Previous optical studies of IHCs containing nitrogen atoms performed in a glass dewar have shown that abundant atomic and molecular optical emissions can be excited during the sample preparation stage, in which the most prominent feature is the N(²D→⁴S)(α -group) emission of atomic nitrogen and O(¹S→¹D) (β -group) emission of atomic oxygen embedded in a solid molecular nitrogen matrix. Both α - and β - groups are extremely forbidden in the gas phase, whereas they are dramatically enhanced by the crystal field and phonons in the solid phase. Warming of the sample after removing the superfluid

helium from the sample cell initiates interesting chemiluminescence phenomena with participation of nitrogen and oxygen atoms as well as various molecules, and provides information about the structure and content of the nanoclusters. The ESR technique has also been extensively used to study the properties of IHCs. The spectroscopic characteristics such as hyperfine splitting, g-factor and linewidth can be extracted from the ESR spectra of various free radicals such as N, H and D atoms embedded in different matrix environments. Also by using the ESR method, chemical tunneling reactions between atoms and molecules of hydrogen isotopes were discovered and intensively studied in aggregates of nanoclusters forming IHCs.[31, 32, 33]

The overall objective of this work is to investigate the structure, composition and quantum properties of IHCs containing different types of impurities. In particular, we want to achieve IHC samples that can have highest concentration of free radicals like N and H atoms. First, different samples containing N atoms were prepared using gas mixtures with various impurity ratios such as N_2 -Kr-He, N_2 -Xe-He, N_2 -Ne-He mixtures and so on to search for best candidates which have highest concentrations. The electron spin resonance (ESR) technique is the main tool to characterize the properties of samples and to measure the concentration of free radicals. Spectroscopic parameters such as g-factors and hyperfine splittings for different radicals embedded in various matrices were obtained. It was found that the addition of Kr atoms to the condensed N_2 -He gas mixture leads to a record high average and local concentration of stabilized N atoms in N- N_2 -Kr-He condensates. Shell structure of the nanoclusters which formed the IHCs is confirmed by analyzing the shape of ESR spectra.

In addition, we studied the percolation between nanoclusters in IHCs containing stabilized H and D atoms. Our approach is based on the observation of H atom recombination or exchange tunnelling reactions between atoms and molecules of hydrogen isotopes from neighboring nanoclusters in the IHC samples using the ESR technique. H and D atoms each exhibit a different ESR spectrum, which makes it straightforward

to study the kinetics of the reactions involving these atoms. We studied percolation for two different types of IHCs in our experiments.

The structure of this dissertation reflects the fact that different samples were studied in our investigations of impurity-helium solids. Section 2 is dedicated to the description of the experimental system which was similar in all the experiments. Section 3 describes our results for IHCs containing stabilized N atoms. And in section 4, I discuss the percolation studies of IHCs containing H and D atoms.

2. EXPERIMENTAL SETUP

In this work, I present the results of various experiments involving IHCs. The electron spin resonance (ESR) technique and optical spectroscopy are the main tools used to investigate the samples. IHC sample preparation is realized in a specially designed environment at cryogenic temperatures. In this section, I shall describe the design and performance of our experimental setup that combines the sample preparation and investigation. The setup also enables simultaneous electron spin resonance (ESR) and optical studies of nanoclusters with stabilized free radicals. The sample preparation methods in the subsequent sections are almost the same as the one described here.

2.1 Overall scheme of the setup

The experimental setup is composed of five parts, including a Janis helium-4 cryostat, an ESR registration system, an optical registration system, a gas handling system with a flux controller, and a pumping system. Figure 2.1 shows a block diagram of the setup. The gas handling system is where the gas mixture is prepared and stored. Different types of gas mixtures can be made by mixing up to four different gases together. After the gases become uniformly mixed, the mixture is sent to the entrance of the quartz capillary, passes through the discharge zone and is then injected into the bulk superfluid helium in the sample beaker. A flux controller from Brooks Instruments is installed just before the quartz capillary entrance to maintain the gas mixture flux at 5.0×10^{19} atoms/sec. The pumping system is primarily used for pumping helium gas away from the variable temperature insert (VTI) to achieve temperatures below 4.2 K. It is composed of an Edwards 80 two stage vacuum pump and an Edwards EH 1200 mechanical booster (a roots blower) with the former as a back up pump for the latter. The combination of the two pumps provides efficiency of pumping helium gas up to 233

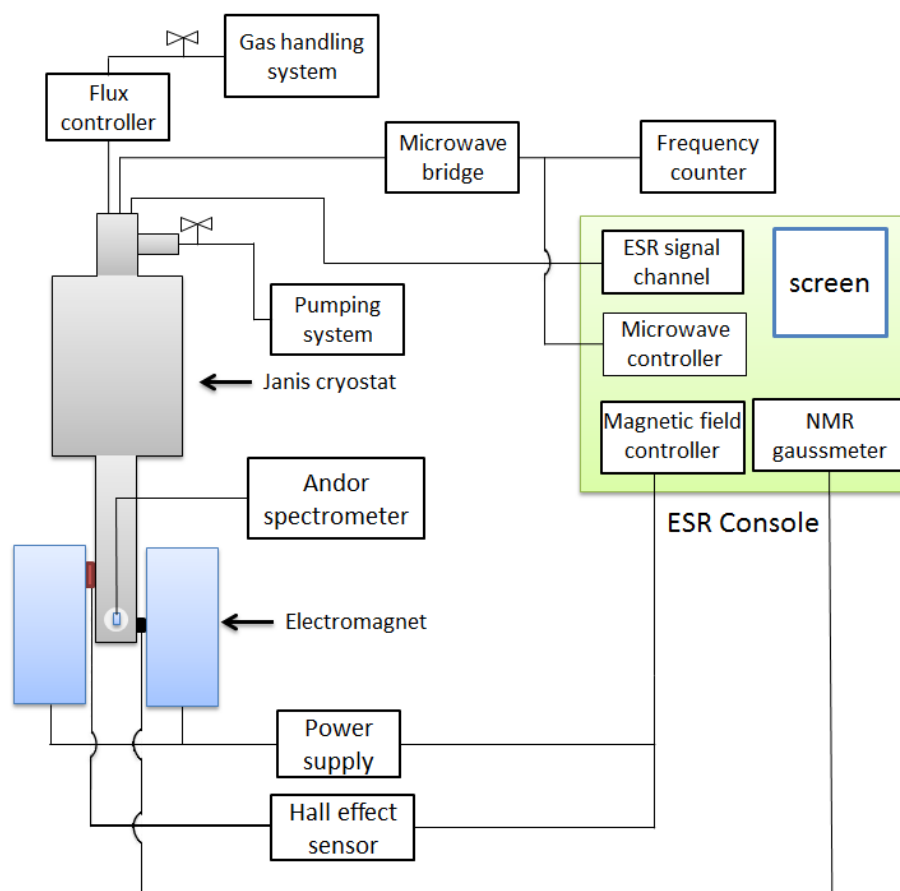


Figure 2.1: Block diagram of the experimental setup.

l/s and allows us to achieve sample temperatures down to 1.25 K. The rest of the setup is described in more detail below.

2.1.1 Janis helium-4 cryostat

The Janis SuperVariTemp(SVT) System is a research cryostat specially designed for ESR and optical studies that can be used to perform a wide variety of experiments in the temperature range from 1.25 K to 300 K. The system combines a variable temperature insert (VTI), a vacuum insulated dewar, and a temperature controller. Liquid helium is used to cool the sample as described below.

The SVT system uses flowing helium gas, obtained by vaporizing liquid helium, to cool or warm the sample which is located in the VTI within the operating temperature range. The main helium bath and the VTI are connected by a capillary. LHe exits the main bath through a needle valve, and enters a vaporizer at the bottom of the VTI. The vaporizer temperature is usually regulated by an automatic temperature controller, using a $25\ \Omega$ resistor for heating and a Lakeshore germanium thermometer installed at the sample cell. LHe flows into the vaporizer, evaporates, warms up to the desired temperature, and then enters the VTI. The helium vapor flows past the sample cell, warms or cools the sample, then exits through a vent port at the top of the cryostat. A vacuum isolation tube surrounds the VTI, preventing the heat conducted from the warm gas into the main helium bath.

The SVT system can also be operated with the sample immersed in liquid helium. Admitting LHe into the vaporizer while the control heat is turned off permits LHe to fill the VTI, cooling the sample to 4.2 K. Temperatures as low as 1.25 K can be achieved by reducing the pressure of the helium vapor above the LHe in the VTI using the pumping system.

The dewar consists of welded stainless steel main liquid helium and liquid nitrogen(LN₂) reservoirs, surrounded by an insulating vacuum space. A LHe and

LN₂ level sensor are installed in the main LHe and LN₂ reservoirs, respectively, to monitor the height of these cryogenic liquids. The dewar provides 15 liters LHe capacity and 12 liters LN₂ capacity. After the main helium bath is full of LHe, the temperature of the sample in the VTI can be stabilized at 1.3 K for as long as 8 hours before the next filling of liquid helium. Multiple refilling of the main bath with liquid helium while keeping experimental conditions unchanged ($T \sim 1.3$ K) in the VTI provides the possibility of running long term experiments.

The tail of the cryostat was placed between the pole pieces of the Varian electromagnet for CW ESR investigations. On each side of the tail, there is a round quartz window with diameter 3 cm. These windows coincide with the hole positions of the ESR cavity to provide optical excess to the sample.

2.1.2 Description of the homemade insert and sample preparation

We used a homemade insert for formation and investigation of atoms contained in the IHCs (see figure 2.2). For sample preparation, a mixture of impurity gases and helium gas was transported from a room temperature gas handling system to the cryogenic region. To provide atomic free radicals via dissociation of the gas molecules, high-power radio-frequency ($F \sim 50$ MHz, $P \sim 70$ W) was applied to electrodes which were placed around the quartz capillary carrying the mixed gases. The resulting jet of helium gas with a small fraction (1% - 4%) of impurity atoms and molecules emerging from the quartz capillary was directed onto the surface of superfluid ⁴He contained in a small beaker suspended above the VTI helium bath. The level of superfluid ⁴He in the beaker is maintained constant by a fountain pump which is placed at the bottom of the insert. The addition of helium gas to the gas mixture increased the efficiency of dissociation of impurity molecules in the discharge due to interaction between the impurity and metastable He atoms and molecules and also retarded agglomeration of impurity atoms and molecules in the gas jet. The gaseous jet penetrated the surface of

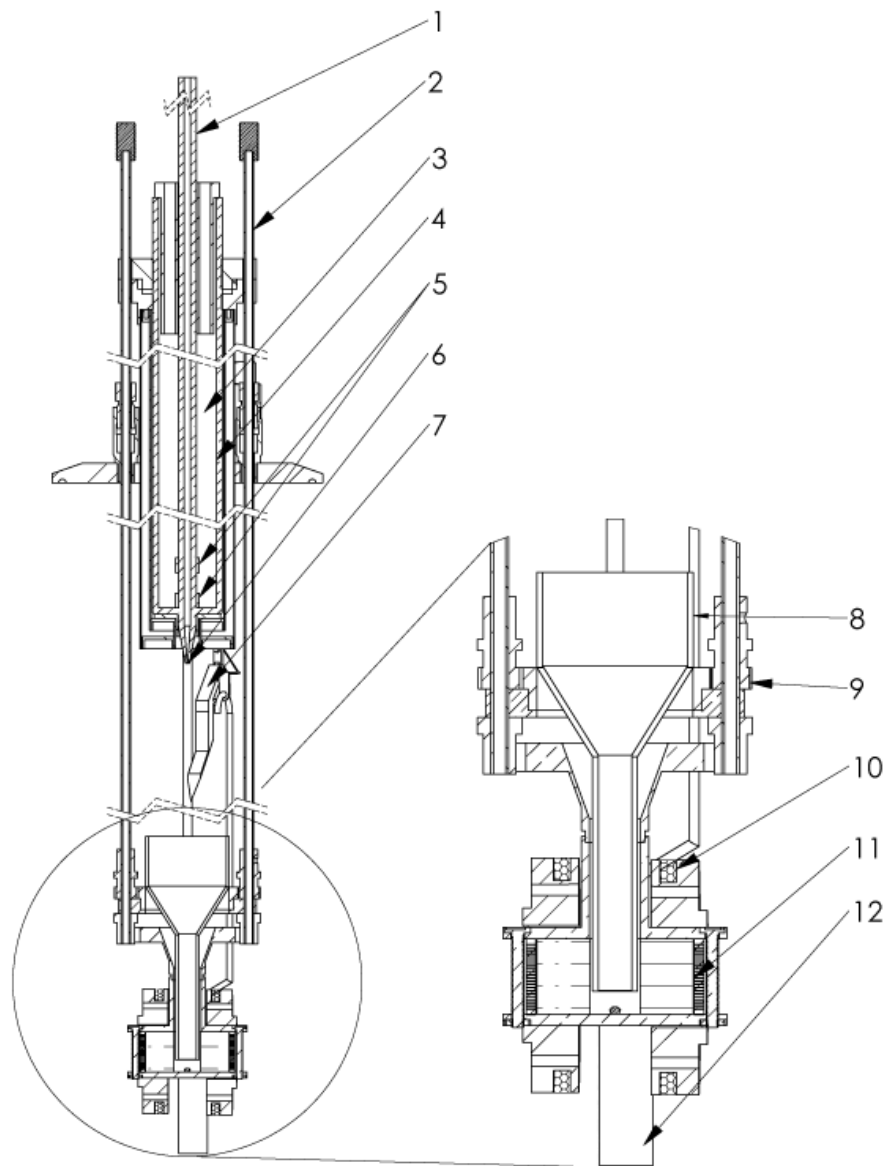


Figure 2.2: Low temperature insert for VTI used in the ESR investigation of IHCs. 1- quartz capillary, 2- tubes for displacement of the beaker in vertical direction, 3- liquid nitrogen, 4- quartz tube, 5- discharge electrodes, 6- orifice, 7- teflon blade, 8- sample collection beaker, 9- beaker rotation gear, 10- modulation coil, 11- horizontal slits on cavity, 12- fountain pump.

the liquid helium and a macroscopic snow-like translucent material was created. This material fell down through the liquid ^4He to form a porous solid at the bottom of the beaker. The temperature during sample preparation was 1.5 K. At the top of the beaker was a funnel (see figure 2.2) that caught the sample as it condensed below the helium surface, which was 2 cm below the end of the quartz capillary. A set of two teflon blades scraped the sample from the funnel while the beaker was rotated so that the sample could fall to the bottom of the cylindrical part of the beaker. A jet with a flux of $\sim 5 \times 10^{19}$ atoms and molecules per second yielded $\sim 0.3 - 0.4 \text{ cm}^3$ of sample in 10 minutes. After sample preparation, a pair of sliding tubes was used to lower the beaker containing the sample into the ESR cavity, which was situated at the bottom of the cryostat in the homogeneous field region of the Varian 7800 electromagnet.

The homemade cylindrical copper cavity with inner diameter 28 mm and height 13.5 mm was operated in the TE_{011} mode (see figure 2.3 and 2.4). The cavity has an axial hole to provide access for the beaker with sample. Unlike a normal cavity, 22 horizontal thin slits were cut through the cylindrical side wall of the cavity to prevent microwave excitation of the TM_{111} mode as well as to allow the modulation magnetic field to penetrate into the cavity. The slits were then filled with epoxy and the inner surface of the cavity was polished carefully. The modulation coil (see figure 2.2) with diameter 3.8 cm was made by winding 40 turns of tinned copper wire into the grooves of two phenolic discs. The separation between the two coils was $a = 1.9 \text{ cm}$, which satisfies the Helmholtz condition $R = a$. A fused silica quartz cylinder was placed inside the cavity in order to reduce its size and bring the resonance frequency down to about 8.9 GHz. The reason for using this quartz piece is because of the geometry restriction resulting from the rather small distance between the magnet's pole pieces. A small cylindrical hole with diameter 3 mm and height 4 mm was cut on the top of the quartz piece to provide space for a microwave coupling loop. The distance between this hole and the center of the cavity is 9 mm. The coupling loop was made by bending

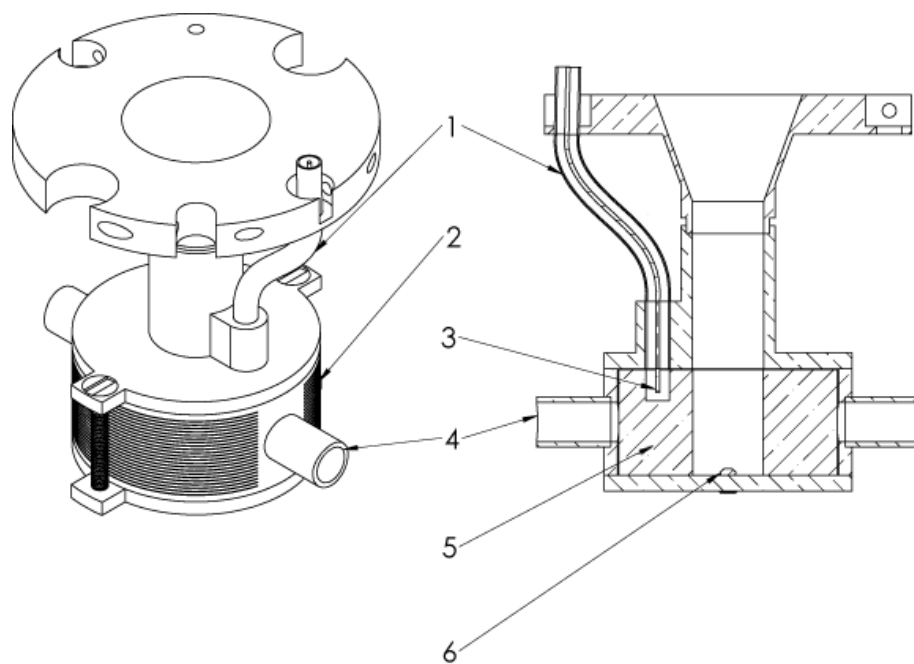


Figure 2.3: ESR cavity. 1- coax, 2- horizontal slits in the cylindrical surface of the cavity, 3- microwave coupling loop, 4- holes for optical access, 5- fused silica cylinder with the hole for the beaker, 6- ruby crystal.

the inner pin of a coax cable. The loop plane was oriented perpendicular to the radial direction of the cavity to provide a favorable condition for microwave excitation of the TE_{011} mode. In addition, two round holes were cut in the middle of the cavity side wall to allow the possibility of optical access to the sample. The transmission of fused silica in our wavelength range 200 nm-1100 nm is $\sim 95\%$ so that it does not affect the light collection appreciably. A ruby crystal was permanently attached using epoxy at the center of the bottom of the cavity to provide a reference point for ESR signals of atoms under study.

We performed calculations of the characteristics of the cavity by using the CST MICROWAVE STUDIOTM code. The distribution of the microwave magnetic field for operating mode TE_{011} is presented in figure 2.4a. From this figure, it can be seen that the symmetry of the magnetic field is disturbed by the presence of the loop in the hole. Figure 2.4b shows the dependence of the axial component of the microwave magnetic field along two orthogonal lines perpendicular and parallel to optical access direction crossing the cavity at the center. The axial microwave magnetic field is maximal in the region where the beaker with the sample was placed. The dependence of the axial magnetic field along the cavity axis is shown in figure 2.4c. Usually the height of the sample ranges from 5 to 10 mm. The calculated integrals of the microwave magnetic field in the sample volume allowed us to determine the filling factor and the absolute number of paramagnetic species in the samples.

2.1.3 System for ESR registration

The ESR registration system is composed mainly of four parts, including a Varian electromagnet, a microwave klystron bridge, a console and an ESR cavity. The Varian electromagnet can produce large steady magnetic fields with the field homogeneity better than 10 ppm over a 1 cm³ volume. A magnet power supply and a small Hall probe (mounted on one of the magnet pole pieces, see figure 2.1) are connected to the

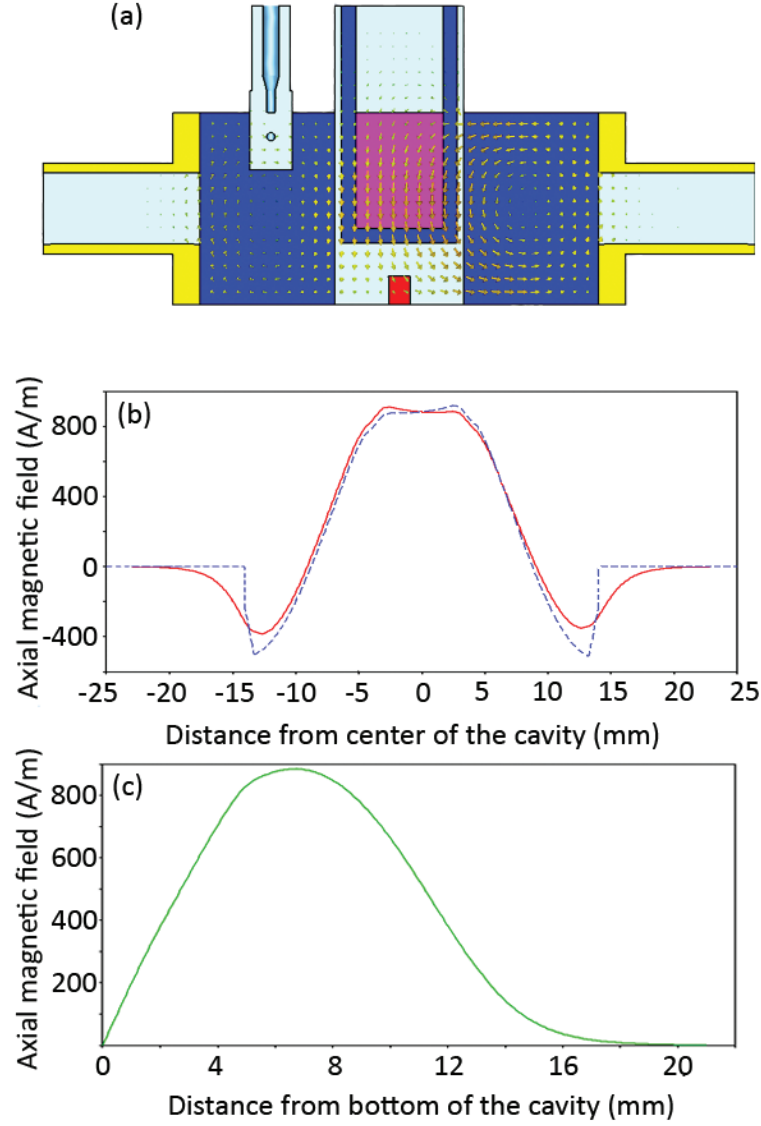


Figure 2.4: Microwave magnetic field distribution in the ESR cavity. a) simulated microwave magnetic field distribution in the cross section of the ESR cavity when the beaker with sample is place in the cavity, b) dependence of the magnetic field component H_z in the horizontal middle plane along the optical access hole direction (solid) and in the perpendicular direction (dotted), c) dependence of the magnetic field component H_z along the vertical axis.

field controller. The desired magnetic field is set up manually on the console. The field controller is capable of producing field sweeps from 5 s to 1 hour in duration and from 0.1 to 10^4 G in amplitude. The microwave radiation is derived from a coherent radiation source klystron. The source power is split into a power arm, used to both irradiate the sample and detect the signal, and a reference arm. The incident power is adjusted by a rotary vane attenuator and directed to the sample by a microwave circulator. The power can be controlled through the console in the range of $2\text{ }\mu\text{W}$ to 200 mW. The reference arm serves the dual function of biasing the detector diode and phase discriminating between the absorptive and dispersive components of the ESR signal. The biasing level is controlled by the reference arm attenuator while the phase discrimination is controlled by the reference arm phase shifter. The detector diode is biased to ensure that it operates in the linear regime. The diode detector current is a linear function of the voltage when the diode is biased to operate in this regime.

The Bruker EPR 300E console is a research grade scientific instrument. It is capable of routine measurements, as well as sophisticated and advanced experiments when equipped with the proper accessories. It is composed mainly of five modules (see figure 2.1) including an ESR signal channel, a microwave controller, a magnetic field controller, a nuclear magnetic resonance (NMR) gaussmeter and a computer display. The ESR signal channel is a signal enhancement and processing unit. It serves as a conventional lock-in amplifier to achieve a significant improvement in signal to noise ratio by virtue of bandwidth limitation. A frequency source derived from the signal channel serves to encode the signal response at the modulation frequency by amplitude modulating the DC magnet field. The ESR signal is detected as the first Fourier harmonic of the applied magnetic field modulation frequency and in-phase with the frequency of the lock-in reference arm. This process increases the S/N ratio by converting the signal to AC to avoid the large background DC where the microwave detector diode noise ($1/f$) is large, and by limiting the frequency bandwidth of the receiver. The modulation

frequency can be set at 100 kHz, 50 kHz, 25 kHz, 12.5 kHz, 6.25 kHz, 3.13kHz and 1.56 kHz. Most often, 100 kHz was used in our experiments. The magnetic field controller uses a Hall probe to detect the field and send a feedback signal to the power supply to control the magnet current. A gaussmeter was used for precise measurements of the applied magnetic field. The resolution of the measured field is about 2 mG.

During measurements, CW ESR signals were recorded by using a continuous microwave source operating near 8.9 GHz. Derivatives of the ESR absorption lines were detected at ~ 0.32 T by lock-in amplification using an additional small amplitude modulation field oscillating at 100 kHz as mentioned above. The number of atoms stabilized was measured by comparing the intensity of atomic signals with the intensity of a signal from a small ruby crystal that was used as a secondary standard. The ruby crystal was attached permanently to the bottom of the microwave cavity. The calibration of the absolute value of the number of spins in the ruby crystal was made by using a standard organic diphenyl-picrylhydrazyl (DPPH) sample with a known number $\sim 2.4 \times 10^{17}$ of spins. The atomic concentrations were calculated by dividing the number of atoms by the volume of the sample. The measurements were carried out at $T = 1.35\text{-}25$ K. For obtaining precise values of g-factors and hyperfine splitting constants of atoms under investigation, a frequency counter EIP 545B from Phase Matrix Inc. was used to precisely measure the microwave frequency at the resonance.

2.1.4 System for optical registration

Figure 2.5 shows the scheme for collecting light from the sample placed in the center of the cavity. During the warming up or destruction of the sample, the recombination of stabilized atoms are initiated and as a result, the sample produces luminescence. This light propagates through the holes in the cavity, passes through the window in the tail of the cryostat and is then collected by the focusing lens. The light collected is directed

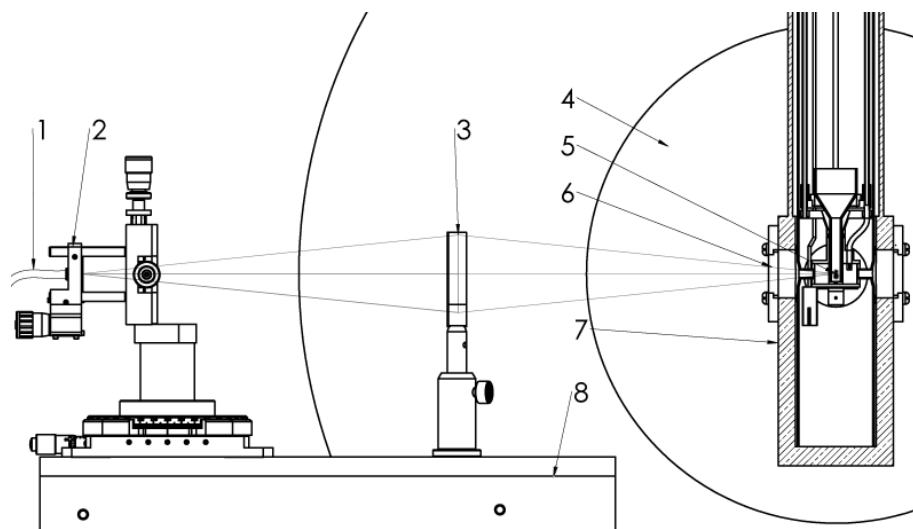


Figure 2.5: Scheme for collection of luminescence from the sample inside ESR cavity. 1-fiber, 2-fiber launch, 3-lens, 4-magnet, 5-sample, 6-quartz window of the tail, 7-tail of the cryostat, 8-optical table.

onto the center of a fiber which is fixed behind the lens. The fiber then feeds the light to the entrance of the Andor spectrometer.

The Andor spectrometer is composed of a Shamrock 500i spectrograph and a Newton EMCCD camera. The Andor Shamrock 500i spectrograph is based on the Czerny-Turner optical design with a focal length 500 mm. The spectrograph is equipped with three gratings, each with different resolution and effective wavelength range. The first grating has 150 lines/mm and a resolution 0.52 nm with effective wavelength range from 200 nm to 6915 nm. The second grating has 600 lines/mm and a resolution 0.13 nm with effective wavelength range from 200 nm to 1730 nm, while the third one has the highest resolution, 0.04 nm and 1800 lines/mm with effective wavelength range from 200 nm to 575 nm. All three gratings are motorized and can be controlled by software on the computer. In our experiments, the gratings are operated mainly in the visible spectrum range. The Newton EMCCD camera employs Andor's pioneering electron multiplying charge-coupled device (CCD) platform with exclusive sensor formats optimized for ultra-low light level spectroscopy applications. The minimum exposure time of the camera can be set at 3 msec. The camera is equipped with a thermo-electric cooling system, which can reach a minimum cooling temperature of -100°C without the inconvenience of using LN₂ in order to deliver optimal signal to noise performance. The effective wavelength range of the Newton EMCCD camera is from 200 nm to 1100 nm. The quantum efficiency curve for Newton EMCCD is shown in figure 2.6.

Due to the independence of the ESR and optical systems, it is possible to use both techniques at the same time. After sample preparation, the beaker is lowered into the cavity, where the bottom of the beaker can be seen through the holes in the cylindrical wall of the cavity.

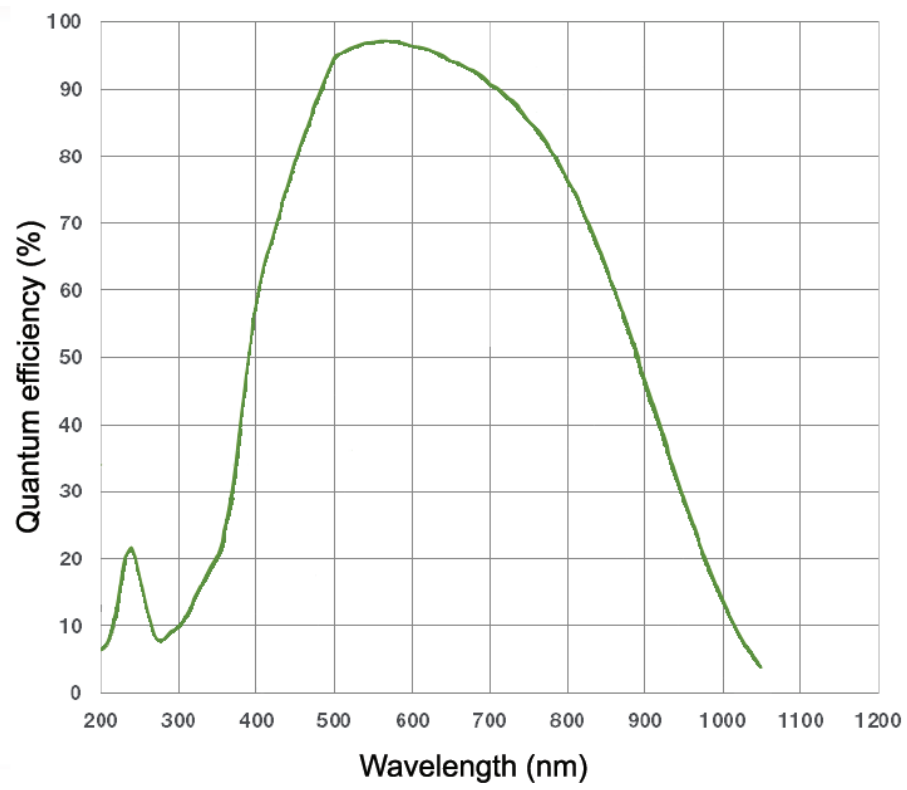


Figure 2.6: Quantum efficiency for Newton EMCCD camera.

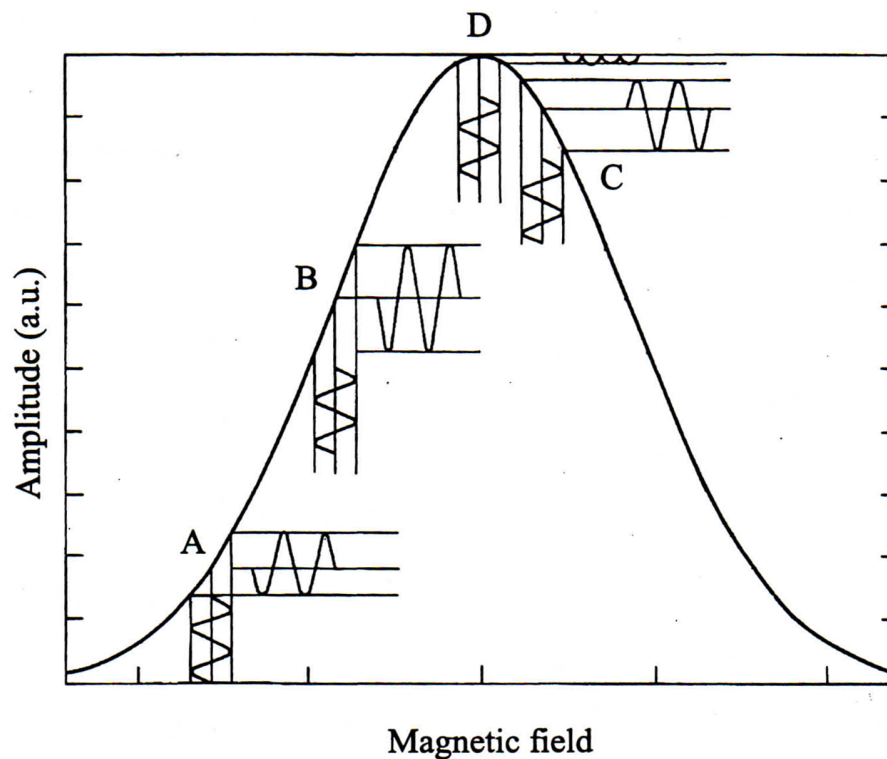


Figure 2.7: The ESR signal produced at various points on the resonant line during a slow sweep of the steady magnetic field and simultaneous application of 100 kHz modulation field. The modulation field is shown by vertical sine waves. Horizontal sine waves show the output taken at points A, B, C, and D. The output signal is proportional to the slope of the absorption curve: at point D it is the smallest, at point B - the biggest; point A and C show intermediate results.

2.2 How does continuous ESR work

The electron spin resonance is induced in the sample when the magnetic field \mathbf{H} is scanned through the resonant condition given by $h\nu = g\beta H$. Here h is Planck's constant, $\nu = 8.9$ GHz, the microwave frequency matched to the resonant frequency of the cavity, g is g-factor of electron, and β is the Bohr magneton. The change in absorption by the spins leads to a change in the reflected signal, which we detect. In reality this signal is very small. In order to increase the sensitivity of the method, a small 100 kHz modulation magnetic field is applied along with the large steady magnetic field. The principle behind this method is shown in figure 2.7. If the sweep through the resonance is slow compared with period of the 100 kHz modulation signal, then at every point on the absorption curve the small 100 kHz magnetic field gives a signal which is proportional to the derivative of the ESR absorption and modulated by 100 kHz. We can easily see from figure 2.7 that at the point of maximum change in the absorption curve, the output is the largest. At the absorption peak, on the other hand, the curve is flat and the output signal is close to zero. The conditions for this method to work properly are: the modulation amplitude has to be smaller than the linewidth, the sweep has to be slower than 100 kHz, and the passage has to be slow. For details see reference [34]. All of these conditions are satisfied in our experiments.

This 100 kHz modulated signal arrives at the crystal detector which filters out the 9 GHz microwaves and directs the 100 kHz signal through the amplifier to the 100 kHz lock-in detector (the lock-in reference signal is produced by the same signal generator as the one which powers the Helmholtz coils). From the output of the lock-in, the signal proportional to the derivative of the ESR absorption signal is sent to the computer for recording and for further data analysis.

3. ESR STUDIES OF NITROGEN ATOMS STABILIZED IN AGGREGATES OF RG-N₂ NANOCLOUDS IMMERSED IN SUPERFLUID HELIUM

Impurity-helium condensates (IHCs) containing nitrogen and rare gas (RG) atoms immersed in superfluid ⁴He have been studied via both CW electron spin resonance (ESR) and optical spectroscopic techniques. The IHCs are gel-like aggregates of nanoclusters composed of impurity species. It was found that the addition of krypton atoms to the nitrogen-helium gas mixture used for preparation of IHCs increases efficiency of stabilization of nitrogen atoms. We have achieved high average ($5 \times 10^{19} \text{ cm}^{-3}$) and local ($2 \times 10^{21} \text{ cm}^{-3}$) concentrations of nitrogen atoms in krypton-nitrogen-helium condensates. The analysis of ESR lines shows that three different sites exist for stabilization of nitrogen atoms in krypton-nitrogen nanoclusters. Nitrogen atoms are stabilized in the krypton core of nanoclusters, in the nitrogen molecular layer which covers the Kr core and on the surface of the nanoclusters. Similar results have been obtained also for the samples prepared from Xe/N₂/He mixtures. However, the expected higher average concentration of N atoms was not achieved. Simultaneous measurements of both ESR and optical spectra have been performed for the samples prepared from Kr/N₂/He mixtures to provide more information about the dynamic of the sample evolution during warming-up processes. High concentrations of nitrogen atoms achieved in IHCs provide an important step in the search for magnetic ordering effects at low temperatures.

3.1 Introduction

Early studies of matrix isolation of atomic free radicals at cryogenic temperatures were performed in a program initiated at the U.S. National Bureau standards in the 1950s. The goal of this work was to develop highly energetic materials for potential use as rocket fuels. Various techniques were developed to study samples formed in

this research including optical spectroscopy, electron spin resonance (ESR) and x ray diffraction. A comprehensive summary of the early work performed in this field has been provided in the book edited by Bass and Broida.[35] Although considerable new physics was uncovered, the goal of obtaining high enough concentrations for any conceivable applications was elusive. In the studies described, the concentrations above 1% of atomic nitrogen embedded in molecular nitrogen matrices were never obtained.

A new era in achieving high concentrations of free radicals in cryogenic matrix isolation research was ushered in by the experiment of E.B. Gordon, L.P. Mezhov-Deglin and O.F. Pugachev, the results of which were published in 1974.[1] The experiment was conducted in Chernogolovka, Russia (then the Soviet Union). The group developed a method which allowed them to achieve record concentrations of matrix isolated free radicals. The method involved introducing a gas sample at room temperature into a quartz tube extending down into a region cooled to superfluid helium temperatures. Electrodes were placed around the tube near its lower end for the purpose of dissociating gas molecules via a radiofrequency discharge into their atomic free radical constituents. The gas emerged into the main liquid helium region where it condensed into a sample beaker whose superfluid helium level was maintained by a fountain pump connecting the beaker to the main bath below. The method is favorable for the creation of very high concentrations of stabilized atoms because of the efficient cooling of the atoms by cold helium vapor, the rapid heat transfer by superfluid helium from the region of the sample formation and the high specific heat of liquid helium, which minimizes temperature increases from events involving the recombination of free atoms. This method not only allowed exceptionally high concentrations of stabilized atoms (up to 10% atomic nitrogen in N-N₂ samples)[2] but also provided for a variety of significant experiments. Optical spectroscopy[36, 21, 37, 38, 39, 23], ESR[40, 31, 41, 42, 43, 44, 45, 46, 47], x ray diffraction[17, 48, 49, 10, 9] and ultrasound techniques[50, 51, 30, 3] were used to characterize these samples and to determine why free radical stabilization was so

effective. It was found that the samples of impurity helium condensates formed inside superfluid helium have a porous structure composed of nanoclusters of impurity species with characteristic size of order 5 nm.[17] The impurity clusters are surrounded by layers of solid helium and the porous structure is filled with superfluid helium. Recent studies of deuterium-helium[26] and hydrogen-krypton-helium[27] condensates revealed that majority of stabilized atoms reside on the surfaces of nanoclusters of impurities. Also, it was found that the addition of Kr atoms to the condensed gas mixture substantially increased the concentration of stabilized hydrogen and deuterium atoms.[27, 52, 53]

In this work we studied the effect of adding Kr and Xe atoms to nitrogen-helium gas mixtures with the goal of achieving the highest possible concentration of stabilized nitrogen atoms. The experimental setup for investigating stabilized atoms in IHCs at low temperatures based on the technique discussed above was described in more detail in the previous section.

3.2 Theoretical background

In this work we performed ESR studies on atomic nitrogen in different samples. The ultimate goal of our experiments was to achieve the highest concentration of nitrogen atoms and to study the properties and structure of the sample. As a result of our investigations, we stumbled across a number of interesting phenomena including linewidth broadening and spin pair radicals. In order to explain these effects and also to produce a brief overview of the origin of electron spin resonance transitions between hyperfine levels, I will resort to the basic quantum theories.

3.2.1 Hyperfine structure of nitrogen atom

The ground electronic configuration of the nitrogen atom is $1s^2 2s^2 2p^3$, which forms the Russel-Saunders terms 4S , 2D , and 2P . The 4S state is the normal ground state; the doublet states are metastable. A nitrogen atom has three unpaired electrons with spin

$\mathbf{S} = \frac{3}{2}$ orbiting around the nucleus with nuclear spin $\mathbf{I} = 1$. The behavior of an atom in an external magnetic field \mathbf{H} is described by the Hamiltonian:

$$\mathcal{H} = g_J\beta_e\mathbf{H} \cdot \mathbf{J} - g_I\beta_n\mathbf{H} \cdot \mathbf{I} + hA\mathbf{I} \cdot \mathbf{J} \quad (3.1)$$

where g_J and β_e are the Landé splitting factor and Bohr magneton, respectively. And by analogy, g_I is for the nuclear moments and β_n is the nuclear magneton. The first term is just the electronic Zeeman effect. The second term is the so-called nuclear Zeeman effect resulting from the direct interaction of the magnetic field with the nuclear moment; it is usually negligible because β_n is $\sim 1/2000$ of β_e . The last term is the hyperfine interaction of the electron spin \mathbf{S} and the nuclear spin \mathbf{I} and its magnitude is proportional to the hf constant A . Here, since the ground state nitrogen atom 4S has $\mathbf{L} = 0$, we conclude $\mathbf{J} = \mathbf{S}$. Note that even when the magnetic field is zero, the hyperfine term involving $\mathbf{I} \cdot \mathbf{J}$ will produce a splitting of the energy levels. Measurement of the line positions in an ESR spectrum of an atom allows the calculation of g_J and A from the solution of the energy level problem.

For a ground state nitrogen atom, there are twelve magnetic sublevels in an external magnetic field according to the above equation. Since transitions between levels involve changes in magnetic moments, we are interested in magnetic dipole (as opposed to electric dipole) transitions and the selection rules pertaining to them. In strong fields, these selection rules require that only one spin (i.e., electronic or nuclear) flip at a time: $\Delta m_J = \pm 1$, $\Delta m_I = 0$ or $\Delta m_J = 0$, $\Delta m_I = \pm 1$. In ESR work where it is most convenient to vary the dc magnetic field and keep the inducing (microwave) field fixed, one is usually automatically limited to observing only the electron spin transitions $\Delta m_J = \pm 1$, $\Delta m_I = 0$ because of their larger energy difference. Therefore, there are nine allowed transitions for a nitrogen atom (see figure 3.1). In the pure strong-field

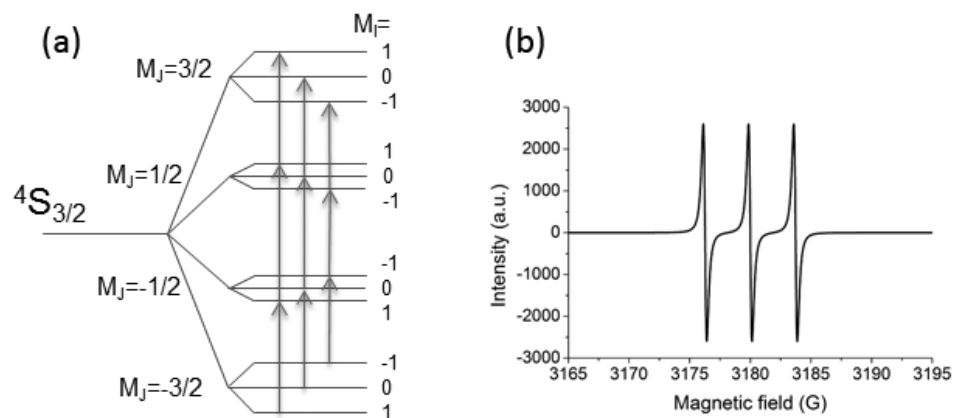


Figure 3.1: a) Energy diagram of N atoms in $4S$ ground state, b) ESR signal of ground state N atoms in gas phase.[54]

case these occur as three triply-degenerate lines, the separation of which is a measure of the magnetic hfs interaction constant A .

3.2.2 The origin of hyperfine splitting

The origins of the hyperfine splitting constant A for different atoms are different. Overall, A depends upon the wavefunction of the unpaired electrons in the atom, or more precisely, upon the difference in magnetic properties and interactions of all electrons with spin up and spin down. It may be described as isotropic (A_{iso}), as occurs for s electrons, and anisotropic or dipolar (A_{dip}), as occurs for p , d electrons. The hfs constant A is the sum of these two contributions, $A_{iso} + A_{dip}$. A_{iso} has no classical counterpart, whereas A_{dip} involves just the interaction between two magnetic dipoles.

(a) Isotropic Hyperfine Constant, A_{iso}

The isotropic interaction A_{iso} is also called the contact or Fermi interaction and depends upon the electron density at the nucleus, $|\Psi(0)|^2$, to which only s electrons significantly contribute. If only this interaction is involved, then the hyperfine structure constant is given by[55, 56]:

$$A_{iso} = \frac{8\pi}{3h} g_e \beta_e g_I \beta_n |\Psi(0)|^2 \quad (3.2)$$

Thus, A for the hydrogen atom in its $(1s^1)^2\mathbf{S}_{1/2}$ ground state is accurately given by the isotropic interaction in equation 3.2. Values of A_{iso} , and thereby $|\Psi(0)|^2$, have been determined for many atoms in the gas phase by optical and atomic beam spectroscopy. $|\Psi(0)|^2$ can also be obtained from *ab initio* theoretical calculations.[57] This interaction is isotropic because there is obviously no angular dependence. The magnetic field at the nucleus can be very large (10^6 G), and s character in the wavefunction, therefore makes a relatively large contribution to the hyperfine interaction.

(b) Anisotropic or Dipolar Hyperfine Constant, A_{dip}

The dipolar interaction energy arises classically from

$$E_{dip} = \frac{\boldsymbol{\mu}_J \cdot \boldsymbol{\mu}_I}{r^3} - \frac{3(\boldsymbol{\mu}_J \cdot \mathbf{r})(\boldsymbol{\mu}_I \cdot \mathbf{r})}{r^5} \quad (3.3)$$

where r is the distance between the magnetic dipoles of the electrons ($\boldsymbol{\mu}_J$) and the nucleus ($\boldsymbol{\mu}_I$). The corresponding quantum mechanical Hamiltonian is

$$\mathcal{H}_{dip} = g_e \beta_e g_I \beta_n \left[\frac{\mathbf{I} \cdot (\mathbf{L} - \mathbf{S})}{r^3} + \frac{3(\mathbf{I} \cdot \mathbf{r})(\mathbf{S} \cdot \mathbf{r})}{r^5} \right] \quad (3.4)$$

If the atom were truly hydrogenic one would find that the hyperfine interaction constant is:

$$A_{dip}(hydrogenic) = \frac{g_e \beta_e g_I \beta_n L(L+1)}{hJ(J+1)} \langle r^{-3} \rangle \quad (3.5)$$

Then for the $^{27}\text{Al}(^2P_{1/2})$ atom, for example, where the observed value of $A_{dip} = 502.0$ MHz,[58] one finds from equation 3.5 that $\langle r^{-3} \rangle_{3p} = 9.14 \times 10^{24} \text{ cm}^{-3}$. This may be compared with the value of $\langle r^{-3} \rangle = 8.92 \times 10^{24} \text{ cm}^{-3}$ found by those authors where small corrections were made for relativistic effects and for the mixing of higher configurations into the ground state $1s^2 2s^2 2p^6 3p^1$ configuration.

If the spin density of the electrons has spherical symmetry about the nucleus (synonymous $L = 0$), then this dipole-dipole interaction averages to zero. Thus for filled and also half-filled shells of electrons, A_{dip} is expected to be zero. Examples are the $(2p^3)^4S$ ^{14}N atom and $(3d^5)^6S$ ^{55}Mn atom. However, owing to higher-order effects, such as core polarization, these two atoms do exhibit small hf splittings. Detailed configuration-interaction (CI) calculations have been made to account for the small hfs (10.5 MHz) for ground state ^{14}N actually observed.

3.2.3 Matrix effects

For atoms and atomic ions possessing no orbital angular momentum, the values of g_J and A determined from their ESR spectra when isolated in the solid inert gas (neon, argon, etc.) are generally quite gaslike. However, it is often found that each expected ESR line observed in a matrix is split into two or more lines. For example, sodium is a $^2S_{1/2}$ ground-state atom with 100% natural abundance of the isotope ^{23}Na with $I = \frac{3}{2}$, one expects to observe just four hf lines centered about $g = 2.00$. However, six sets of lines were actually observed having slightly different g and A values.[59] This is attributed to the trapping of sodium atoms in various sites in solid argon where they experience slightly different perturbations by the surrounding matrix. Often this site structure in spectra can be partially, or even completely, removed by careful annealing of the initial matrix by warming. Because of the ubiquity of this phenomenon in matrices, annealing procedures and effects are usually reported when discussing experimental results.

In general, the exact nature of the sites in matrices is not known, and, of course, it will vary greatly with the properties of the trapped species. One speaks of substitutional and interstitial sites based upon a face-centered-cubic or hexagonal-close-packed structure for the crystalline rare-gas solid,[60, 61] but this is an idealized picture, since packing around the isolated atom will depend upon its size relative to that of the matrix atom. From overlap calculations, Ammeter and Schlosnagle conclude that all alkali, alkaline-earth, and transition-metal atoms are "too large" to fit into substitutional sites.

For N atoms having half-filled np shells and 4S ground states, one expects no hfs, since there is no s electron contribution, and the spherical symmetry of the atom causes the anisotropic hfs to also vanish. The small hfs that is observed in these cases is attributed to spin polarization, as mentioned earlier. For this atom, if trapped in a solid matrix, polarization effects are very sensitive to the environment. Following his earlier treatment of the trapped H atom, Adrian[62] has accounted for the shift in A of

atomic nitrogen in solid nitrogen matrices as largely due to van der Waals interactions that effectively introduce $(2s)(2p^4)$ excited states into the N atom wavefunction. Since the $2p$ shell was half-filled with α spin electrons, the $2s$ electron with β spin had to be excited into the $2p$ orbital, leaving a $2s$ electron with α spin providing increased hfs. These calculations have been repeated with improved wavefunctions by Jackel, Nelson, and Gordy[63] to provide better agreement with the experiment. P and As atoms in the solid rare gases also exhibit large matrix effects, and the theory of Adrian was generalized to account for those perturbations. Those authors indicate that the Group V atoms occupy substitutional lattice sites.

3.2.4 Dipolar broadening

In regular crystals, the width of the ESR absorption lines arising from the magnetic moment of the electron or nucleus is caused primarily by the interaction between the magnetic dipoles of different atoms. The dipolar broadening is caused by a spread in the local magnetic fields experienced by atoms. In general both random orientations of the spins of the atoms and random positions of the atoms lead to this effect. The local magnetic field \mathbf{H} produced by a magnetic dipole of spin \mathbf{S} at distance \mathbf{r} from its center is given by

$$\mathbf{H} = \frac{g_e\beta_e}{r^3}[\mathbf{S} - \frac{3\mathbf{r}(\mathbf{r} \cdot \mathbf{S})}{r^2}] \quad (3.6)$$

For H atoms, at the distance of the H_2 lattice constant $r = 0.379$ nm, the field is $\mathbf{H} \simeq 500$ G. Therefore, the dipole broadening is also a reflection of the concentration of the spins of atoms. When the concentration of spins is high, dipole moments are closer to each other and the local field generated by the nearby dipoles are higher than would be the case when dipoles are far apart. According to the calculation of Van Vleck, the dipole-dipole broadening of ESR lines in an fcc lattice is given by[9]

$$\Delta H_{dd} = 2.3g_e\beta_e\sqrt{S(S+1)}n_l \quad (3.7)$$

where ΔH_{dd} is in gauss and n_i is the concentration of atoms of spin S .

3.2.5 Spin pair radicals

An interesting case is that when two spins of atoms are very close to each other, it is possible that they could form spin pair radicals. The spins of the two nearby atoms are strongly coupled to form a triplet state. With three energy levels, two types of transitions are possible, namely, $\Delta M_s = \pm 1$ and $\Delta M_s = \pm 2$. For a radiation field of fixed frequency, the conservation of energy causes the $\Delta M_s = \pm 2$ transitions to occur at about half the average H for $\Delta M_s = \pm 1$ transitions.[64] Also, due to parity conservation, it is required that the direction of the radiation field is parallel to the external magnetic field instead of perpendicular as in the $\Delta M_s = \pm 1$ transition case.

3.3 Experimental results

3.3.1 IHCs with N₂/Kr/He mixtures

The sample preparation method and the ESR technique has been discussed in section 2. Here, we directly present the experimental results. We studied the effect of the addition of Kr atoms in the N₂/He gas mixture on the efficiency of stabilization of N atoms in IHCs. In figure 3.2 we display ESR spectra of N atoms contained in different IHC samples at 1.35 K. Curve 1 corresponds to the sample prepared from gas mixture [N₂]/[Kr]/[He]=1/5/1200. Curve 2 corresponds to the sample prepared from gas mixture [N₂]/[He]=1/1200. In these gas mixtures the ratio between the nitrogen molecules and helium was kept equal to 1/1200. In the experimental runs a series of ESR spectra of N atoms were recorded at T= 1.35 K for each sample. From this figure the effect of increasing the efficiency of stabilization of N atoms by adding Kr atoms to the condensed nitrogen-helium gas mixture is clearly seen. Firstly, the intensity of the ESR signal from N atoms is ~ 6 times larger for the sample formed with addition of Kr atoms indicating a substantial increase in the average concentration of N atoms in

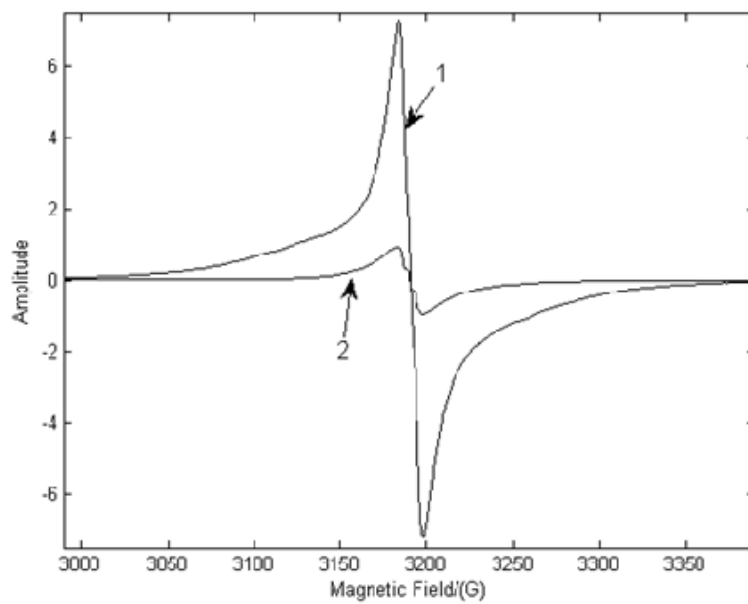


Figure 3.2: ESR spectra of N atoms in an as-prepared N-N₂-Kr-He sample at 1.35 K (1). The sample was prepared from a gas mixture with ratio $[N_2]/[Kr]/[He]=1/5/1200$. ESR spectra of N atoms in as-prepared N-N₂-He sample at 1.35 K (2). The sample was prepared from a gas mixture with ratio $[N_2]/[He]=1/1200$.

the sample. Secondly, unusually broad wings are seen in this signal, showing significant increase of the local concentration of stabilized N atoms.

With the goal of achieving maximum possible concentrations of stabilized N atoms in nitrogen-krypton-helium condensates, we studied the effect of adding different quantities of Kr gas to the condensed nitrogen-helium gas mixtures. The ratio between impurity species ($[\text{N}_2] + [\text{Kr}]$) and He in the gas mixture was kept constant and equal to 1/200. However, the ratio of nitrogen molecules to krypton atoms, $[\text{N}_2]/[\text{Kr}]$, in the mixture was changed from 1/50 to 4/1. In figure 3.3 the ESR spectra of N atoms in nitrogen-krypton-helium samples prepared with different $[\text{N}_2]/[\text{Kr}]$ ratios are shown. We obtained well resolved ESR spectra of N atoms stabilized in the IHC sample prepared from the gas mixture $[\text{N}_2]/[\text{Kr}]/[\text{He}] = 1/50/10000$ (figure 3.3a). Less resolved, broad ESR spectra of N atoms were detected for the sample prepared from the gas mixture $[\text{N}_2]/[\text{Kr}]/[\text{He}] = 1/5/1200$. Further increase of the $[\text{N}_2]/[\text{Kr}]$ ratio in the condensed gas mixture led to a decrease of the intensity and less broadening of the N atom signal.

The results of the measurements of the average concentrations of N atoms in nitrogen-krypton-helium condensates prepared by using different $[\text{N}_2]/[\text{Kr}]$ ratios are shown in figure 3.4. For some gas mixtures, experiments were performed by using different values of the flux, ranging from 4.6×10^{19} to $5.4 \times 10^{19} \text{s}^{-1}$. Only the highest measured concentrations for each of the mixtures employed are presented in figure 3.4. It has been found that the best results for stabilization of N atoms were obtained for the highest flux used, $5.4 \times 10^{19} \text{s}^{-1}$. The largest average concentrations, of order $5.3 \times 10^{19} \text{cm}^{-3}$, were achieved for the gas mixture $[\text{N}_2]/[\text{Kr}]/[\text{He}] = 1/2/600$. This value is more than double the highest value achieved in IHCs prepared from nitrogen-helium gas mixtures[10] without the addition of Kr atoms.

As a result of the high concentration of N atoms achieved in N-N₂-Kr-He condensates, the atomic separation is short enough for the formation of nitrogen spin pair radicals. The strong dipole forces associated with unpaired spins make it favorable for

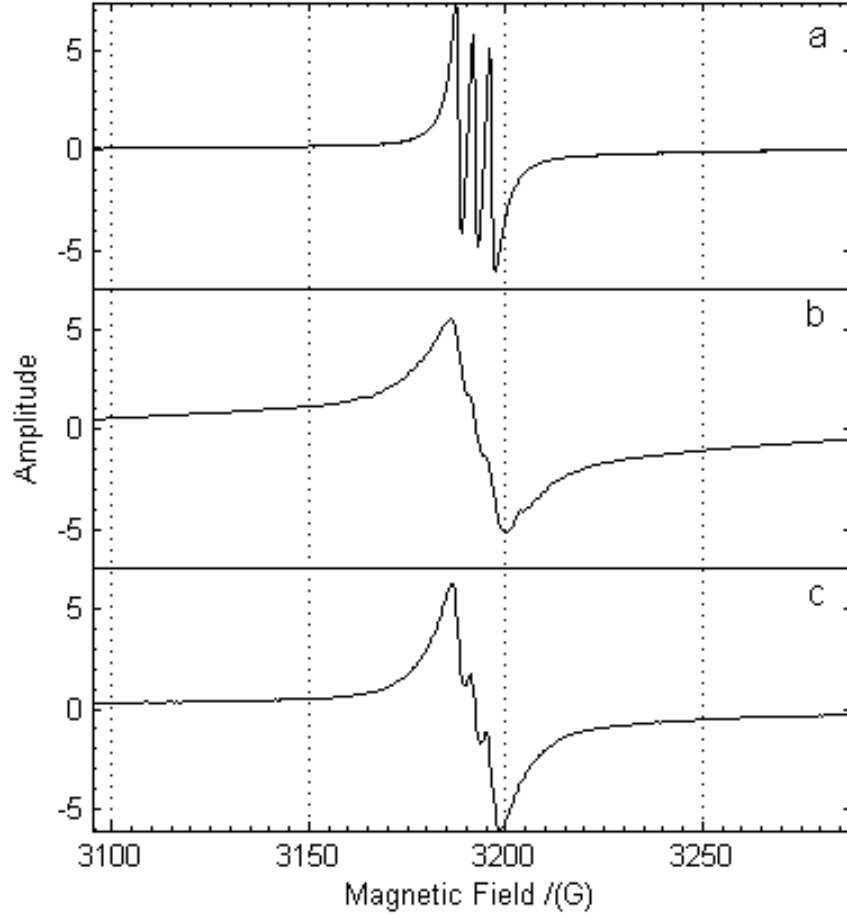


Figure 3.3: ESR spectra of N atoms in as-prepared N-N₂-Kr-He samples prepared from different gas mixtures: a from gas mixture [N₂]/[Kr]/[He]=1/50/10000; b from gas mixture [N₂]/[Kr]/[He]=1/5/1200; c from gas mixture [N₂]/[Kr]/[He]=1/1/400. All spectra were obtained at T= 1.35 K.

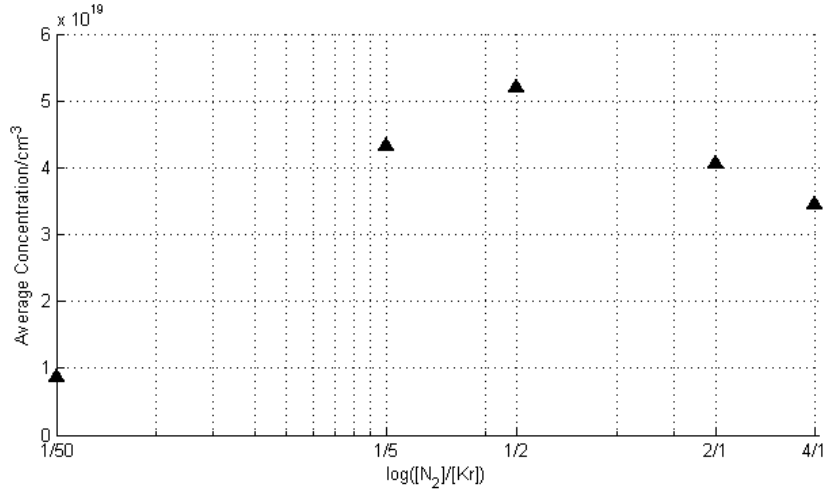


Figure 3.4: Dependence of average concentration of N atoms stabilized in nitrogen-krypton-helium samples on the ratio of N_2/Kr in various gas mixtures. The ratio between the impurity species ($[N_2]+[Kr]$) and He in the gas mixture was kept equal to 1/200 for all gas mixtures used for preparation IHC samples.

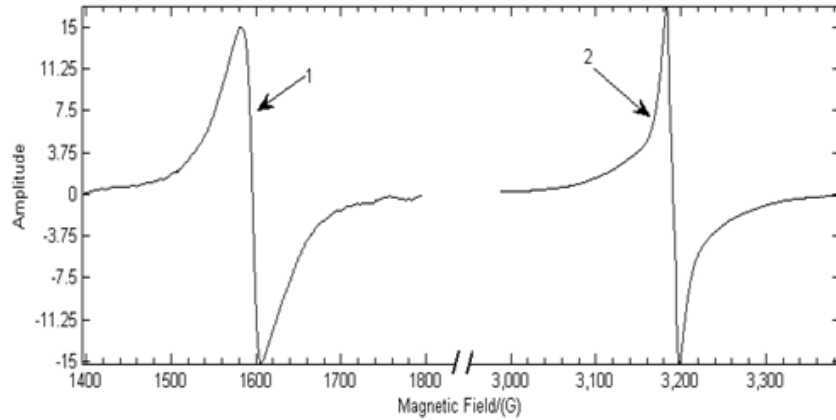


Figure 3.5: ESR spectra of spin pair radicals (1) and individual nitrogen atoms (2) in N- N_2 -Kr-He condensate at $T=1.35$ K. Intensity of spin pair radicals line was multiplied by a factor of 1875. The spectra are obtained in the sample prepared with the gas mixture $N_2/Kr/He=4/1/1000$.

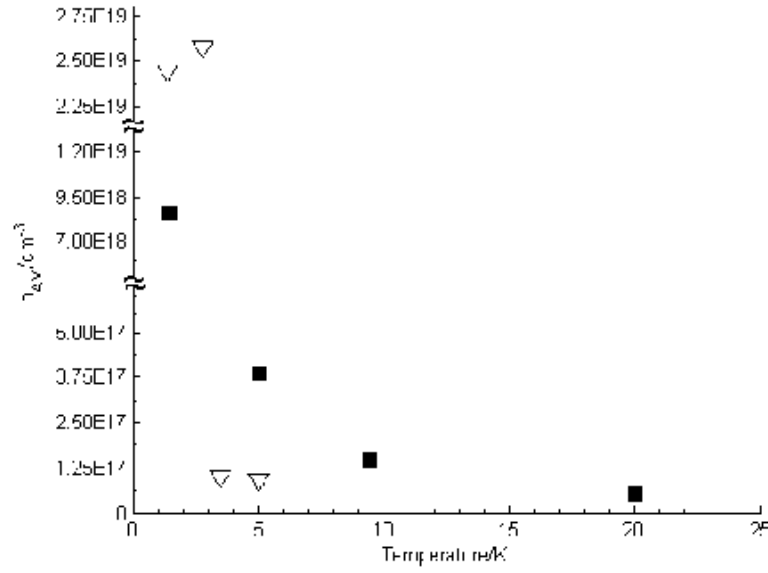


Figure 3.6: Dependence of average concentration of N atoms on the temperature for samples prepared from gas mixtures $[N_2]/[Kr]/[He] = 1/50/10000$ (■) and $[N_2]/[Kr]/[He] = 1/2/600$ (▽).

two spins separated by distances less than 1 nm to flip simultaneously. This corresponds to the $\Delta M = 2$ transition of spin pair radicals, for which two spins in the pair simultaneously change their orientation in the magnetic field due to absorption of one microwave photon. In our experiment, we observed ESR signals for NN spin pair radicals in N-N₂-Kr-He condensates. The ESR spectra of the N atoms and NN spin pair radicals are shown in figure 3.5. Spectra of NN spin pair radicals were observed at half the field compared to the main N atom transition. The ratio between the intensities of the main atomic line and the line of spin pair radicals was found to be 1875 in the experiment. The first observation of NN spin pair radicals in a neon matrix at T = 4.2 K was made by Knight et al.[65] and later our group observed the signal of NN spin pair radicals in nitrogen-helium condensates at T = 1.35 K.[13]

We studied the behavior of N atoms in nitrogen-krypton-helium samples during the annealing process. After observations of as-prepared samples were made at T = 1.35 K, the samples were gradually heated to 20 K. As a first step, we removed liquid helium from the sample cell at T = 2.8 K and performed measurements on N atoms for these dry IHCs. Usually all of the N atoms survived during the drying process at T = 2.8 K, and sometimes we observed an increase in the intensity of the N atom signals due to collapsing of the pores in the sample which led to an increase in the sample density and allowed an additional amount of sample to enter the sensitive zone of the ESR cavity. Upon further increase in temperature of the samples, the broad feature of the signal disappeared and only a small signal remained, which corresponded to the atoms stabilized in the Kr matrix. During sample annealing, rapid diffusion occurred for the N atoms residing on the surface of the nanoclusters, initiating an explosive recombination of the N atoms. This led to sublimation of a substantial part of the sample, which was accompanied by bright light flashes.[23, 24] Only a small fraction of the initial clusters agglomerated into larger crystallites, preserving a small population of N atoms trapped in the Kr matrices. The explosive destruction of the

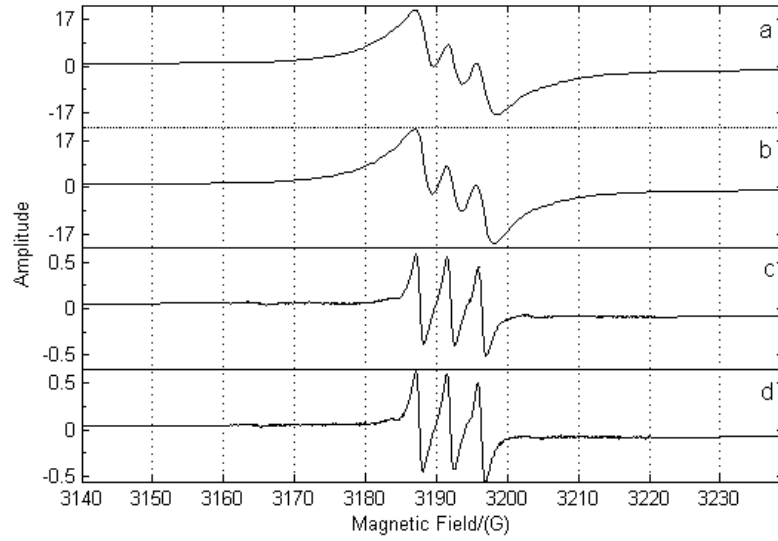


Figure 3.7: Transformation of ESR spectra of nitrogen atoms stabilized in samples prepared with gas mixture $[\text{N}_2]/[\text{Kr}]/[\text{He}]=1/2/600$. Spectra were obtained at temperatures 1.401 K (a), 2.8 K (b), 3.5 K (c) and 5.02 K (d).

Table 3.1: Hyperfine structure constants, A, g factors, peak to peak widths, ΔH_{pp} , and local concentrations for N atoms in N/Kr/He condensates obtained from ESR lines fittings.

Sample	Curve Type	A/G	$\Delta H_{pp}/G$	Local concentration	Weight	g-factor
[N ₂]:[Kr]:[He] =1:50:10000	Lorentzian	4.12	23.25	6.28×10^{20}	74.9%	2.0011
	Lorentzian	4.39	2.19	5.90×10^{19}	25.0%	2.0011
	Lorentzian	4.20	0.45	1.23×10^{19}	0.1%	2.0011
[N ₂]:[Kr]:[He] =1:5:1000	Lorentzian	4.12	67.44	1.82×10^{21}	86.0%	2.0022
	Lorentzian	4.39	3.38	9.11×10^{19}	0.8%	2.0022
	Lorentzian	4.97	11.85	3.20×10^{20}	13.5%	2.0017
[N ₂]:[Kr]:[He] =1:2:600	Lorentzian	4.12	76.97	2.08×10^{21}	84.4%	2.0019
	Lorentzian	4.39	1.99	5.39×10^{19}	0.6%	2.0021
	Lorentzian	4.97	9.47	2.56×10^{20}	15%	2.0019
[N ₂]:[Kr]:[He] =2:1:600	Lorentzian	4.12	74.95	2.02×10^{21}	83.5%	2.0020
	Lorentzian	4.39	9.60	2.59×10^{20}	16.4%	2.0020
	Lorentzian	4.20	1.83	4.94×10^{19}	0.1%	2.0020
[N ₂]:[Kr]:[He] =4:1:1000	Lorentzian	4.12	62.74	1.69×10^{21}	85.6%	2.0019
	Lorentzian	4.39	10.99	2.97×10^{20}	14.3%	2.0019
	Lorentzian	4.20	2.09	5.65×10^{19}	0.1%	2.0019

N-Kr-He samples with high concentrations of N atoms occurred at temperatures in the range 3.5-5 K. Dependence of the average concentration on temperature during annealing of nitrogen-krypton-helium samples prepared from gas mixtures with ratios $[N_2]/[Kr]/[He] = 1/50/10000$ and $1/2/600$ is shown in figure 3.6. In the sample prepared with the former mixture, N atoms were observed even at $T \sim 20$ K, while for the latter mixture, a signal was observed only up to $T \sim 5$ K. Figure 3.7 shows the transformations of the N atom ESR spectra during annealing of the samples prepared with gas mixture $[N_2]/[Kr]/[He] = 1/2/600$. The spectra became more and more resolved with increasing temperature due to a reduction in the concentrations of stabilized N atoms in the samples, leading to a reduced dipole-dipole interaction of the atoms.

The characteristic features of the spectra of N atoms in as-prepared samples of N-N₂-Kr-He condensates are the broad wings and weak triplet at the central part (see curve 1 in figure 3.2). All these features of spectra obtained for as-prepared samples were fitted with a sum of three triplets of Lorentzian lines as shown in figure 3.8. The fitting process was performed by a Graphic User Interface (GUI) program written in Matlab. This GUI program can simulate the experimental signal using up to eight Lorentzian/Gaussian function components. It automatically searches the best hyperfine splitting constant and linewidth for each component. When difference between the simulated curves and the experimental curve becomes minimal, it stops searching and gives the corresponding parameters. Figure 3.8a shows an experimental ESR spectrum for N atoms in an IHC prepared from a gas mixture $[N_2]/[Kr]/[He] = 1/2/600$, and the sum of fitting lines which provide a rather good fit to the experiment. Figure 3.8b shows three fitting lines composed from the triplets with different hyperfine splittings and line widths. Each of the triplets is assigned to the atoms in specific environment. A similar analysis was performed for all spectra obtained for different nitrogen-krypton-helium condensates. The results of this analysis were presented in Table 3.1.

Table 3.2: Hyperfine structure constants, A, and g factors for N atoms in N₂ and Kr matrices.

Matirx	A/G	$(A_{free} - A)/A_{free}(\%)$	g-factor
Free	3.73	0	2.00215(3)
N ₂ (subst.)	4.31	15.6	2.00200(6)
N ₂ (subst.)	4.22	13.6	2.00200(6)
N ₂ (subst.)	4.21	13.4	2.002155(5)
N ₂ (subst.)	4.25	14.0	2.00201(12)
N ₂ (subst.)	4.31	15.6	2.00200(6)
N ₂ (interst.)	4.85	30.1	2.00100(6)
N ₂ (interst.)	4.5	20.67	2.00000(6)
Kr(subst.)	4.47	19.8	2.0012
Kr(subst.)	4.4	17.9	2.0019
Kr(subst.)	4.39	17.7	2.0021(6)

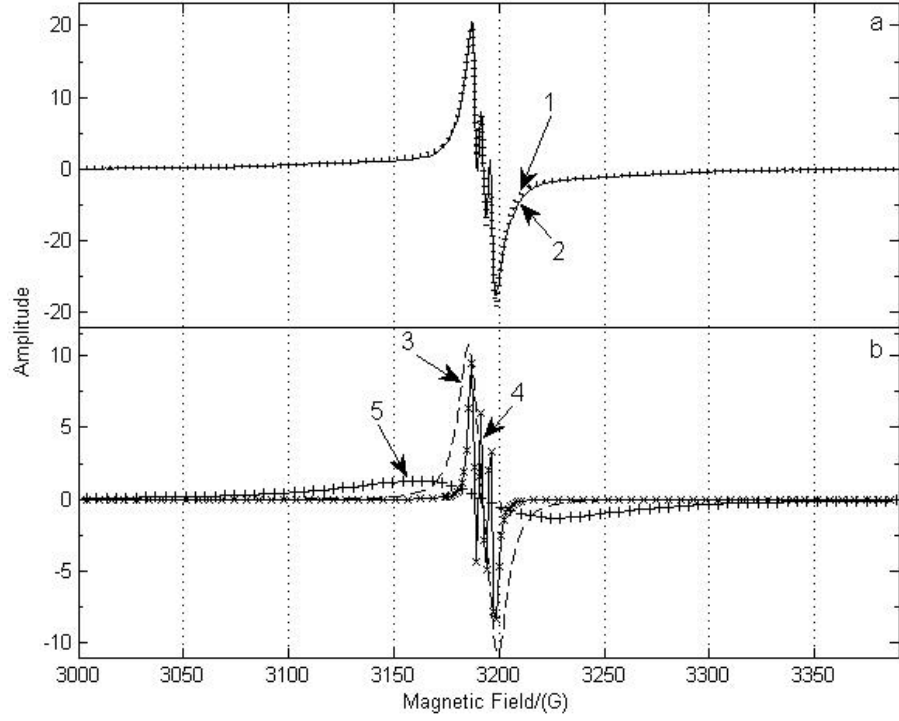


Figure 3.8: a) Experimental ESR spectrum of N atoms for as-prepared nitrogen-krypton-helium sample formed by gas mixture $[N_2]/[Kr]/[He]=1/2/600$ is shown as a solid line (1). The sum of the fitting lines is shown as a dotted line (2). b) Three triplets of fitting lines used for decomposition of the experimental ESR spectrum: 3-triplet of Lorentzian lines with line width 9.47 G and hyperfine splitting, $A=4.97$ G, 4- triplet of Lorentzian lines with line width 1.99G and $A= 4.39$ G, 5- triplet of Lorentzian lines with line width 76.97 G and $A=4.12$ G. The weights of each triplet in the spectra were found to be 13.5%, 0.6% and 84.4%, respectively.

In Table 3.2 the spectroscopic characteristics of N atoms in different matrices are shown. These results were obtained from earlier studies.[54, 66, 67, 68, 69, 70, 71, 63] The spectroscopic characteristics for N atoms as obtained from the fitting procedure were compared with the characteristics for N atoms in different matrices shown in Table 3.2. From these comparisons we found that there are three separate groups of N atoms in a given sample each stabilized in a different environment. We identify triplet 3 in figure 3.8b with N atoms trapped in the Kr matrix ($g= 2.0021$, $A = 4.39$); the narrow triplet 4 in figure 3.8b is assigned to the N atoms inside the N₂ layer ($g= 2.0019$, $A = 4.97$) and the broad triplet 5 in figure 3.8b corresponds to N atoms on the surface of the N₂ layer ($g= 2.0019$, $A = 4.12$). We assigned the latter triplet to N atoms on the surface of N₂ layer because the A value for these atoms is equal to 4.12 G, which is between the value for N in N₂ (4.2 G) and that for the free N atoms ($A = 3.73$ G). We assigned the N atoms with A values equal to 4.2 to substitutional sites in N₂ matrix and the N atoms with $A = 4.97$ G to interstitial sites in N₂ matrix. This is the first time during investigations of matrix isolated atoms that such broad ESR signals were observed. The line width of the signal assigned to the N atoms on the surfaces of the nanoclusters was found to be in the range 60-78 Gauss for different samples. Dipolar magnetic interaction of electron spins is the dominant line broadening mechanism in this system. The local concentration of N atoms might be estimated from formula: $n_l = 2.7 \times 10^{19} \cdot \Delta H_{pp}$, where ΔH_{pp} is the peak to peak width of the ESR lines in Gauss and n_l is the local concentration of the atoms per cm³. [72] Estimates of the local concentrations of N atoms for various samples are shown in Table 3.1. The highest local concentrations of N atoms ($\sim 2 \times 10^{21}$ cm⁻³) were achieved in the samples prepared with gas mixtures N₂:Kr:He=1:2:600 and N₂:Kr:He=2:1:600.

We also found that the addition of Kr atoms to N₂-He gas mixtures leads to increasing the overall efficiency of stabilization of N atoms produced in an RF discharge. For example, for a gas mixture N₂:Kr:He=1:50:10000, the efficiency of N atom capture is 44%,

whereas for gas mixtures with the ratios $\text{N}_2:\text{Kr}:\text{He}=1:5:1200$ and $\text{N}_2:\text{Kr}:\text{He}=4:1:1000$, the efficiencies of N atom capture are 25% and 5%, respectively.

3.3.2 Simultaneous registration of ESR and optical spectra of $\text{N}(^4\text{S})$ atoms during warming up of $\text{N}-\text{N}_2-\text{Kr}-\text{He}$ samples

Luminescence of N atoms embedded in solid matrices and in nanoclusters at low temperatures has been extensively studied.[73, 22, 74, 21, 23] In our experiments, we applied a step-wise temperature controlling method for warming of the sample to study the ESR spectra of N atoms as well as chemiluminescence from the sample simultaneously.

Figure 3.9(a) shows the time dependence of both the temperature in the beaker and the integral of the α -group emission of N atoms. Figure 3.9(b) is the time dependence of the average concentration of $\text{N}(^4\text{S})$ atoms based on the ESR measurement. After the sample was prepared, the temperature of the sample cell was kept at 1.5 K for about 4500 sec (75 min). The sample was immersed in superfluid helium and was very stable without showing any luminescence during this period of time. After that, we evaporated the liquid helium from the sample cell and the temperature was increased gradually to 2.7 K. During the warming up process, the "green" luminescence of the sample was observed, indicating the recombination of N atoms. Figure 3.10 shows the optical spectrum taken during the warming up from 1.5 K to 2.7 K of the sample. In the spectrum, only the α -group and weak β -group emissions were observed. The α -group emission is due to the transition $^2\text{D}\rightarrow^4\text{S}$ of N atoms embedded in nitrogen molecular solids with wavelength centered at 522 nm, while the β -group emission is due to the transition $^1\text{S}\rightarrow^1\text{D}$ of O atoms embedded in nitrogen molecular solids. The β -group is very broad with a span of about 50 nm centered at ~ 560 nm. It is known that both of transitions are extremely forbidden in the gas phase but dramatically enhanced in the solid phase due to the perturbation by the crystal field and phonons. The average

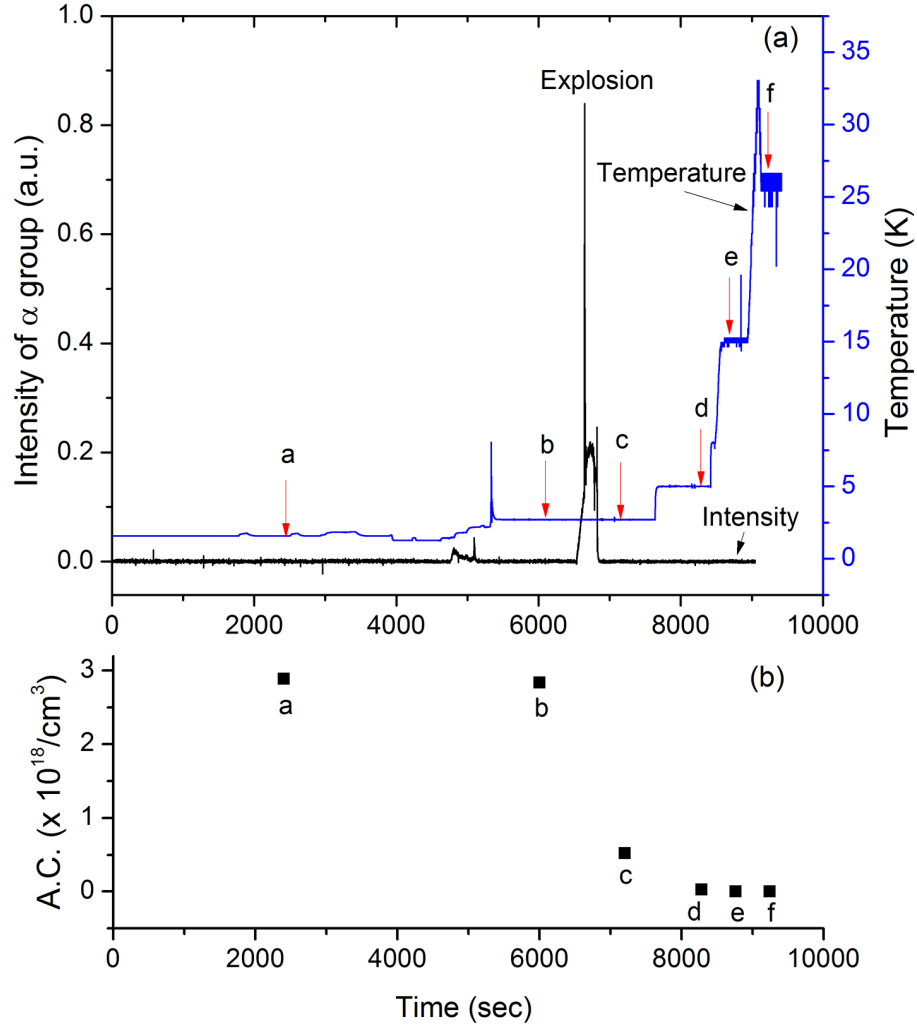


Figure 3.9: (a) Dependence of temperature of the cell and intensity of α -group emission of N atoms on time during warming of N-N₂-Kr-He condensate. (b) Dependence of N(⁴S) atom average concentration (A.C.) on time during warming of the condensate. The concentration of N atoms in figure (b) are measured at the moments shown by arrows in figure (a).

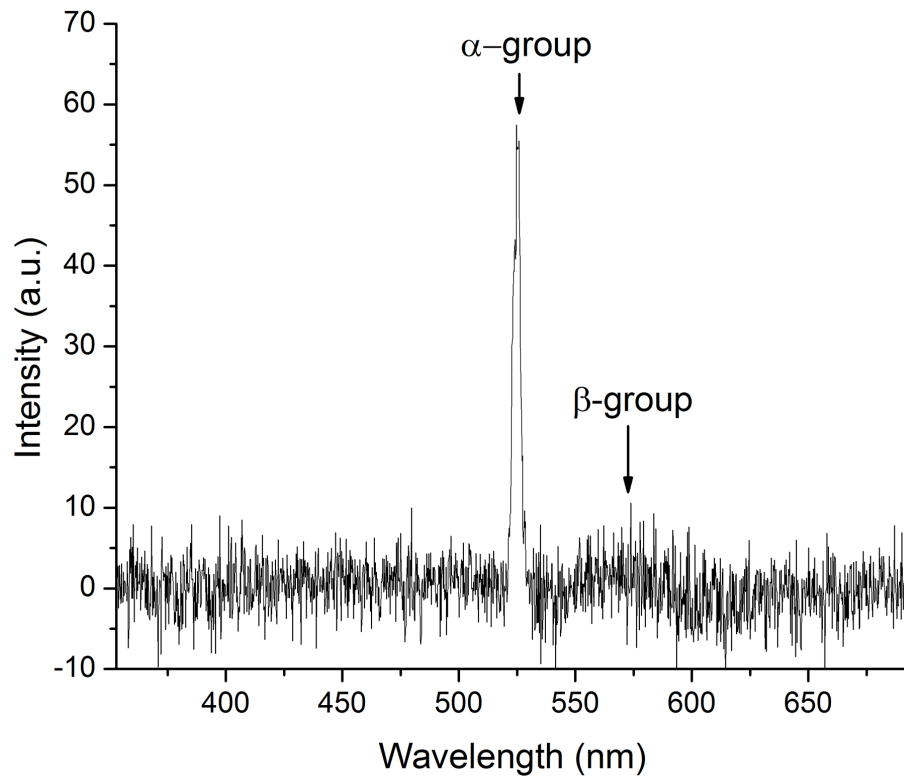


Figure 3.10: Example of optical spectrum during warming up process of the sample from 1.5 K to 2.7 K. The exposure time for spectrum registration is 3 msec.

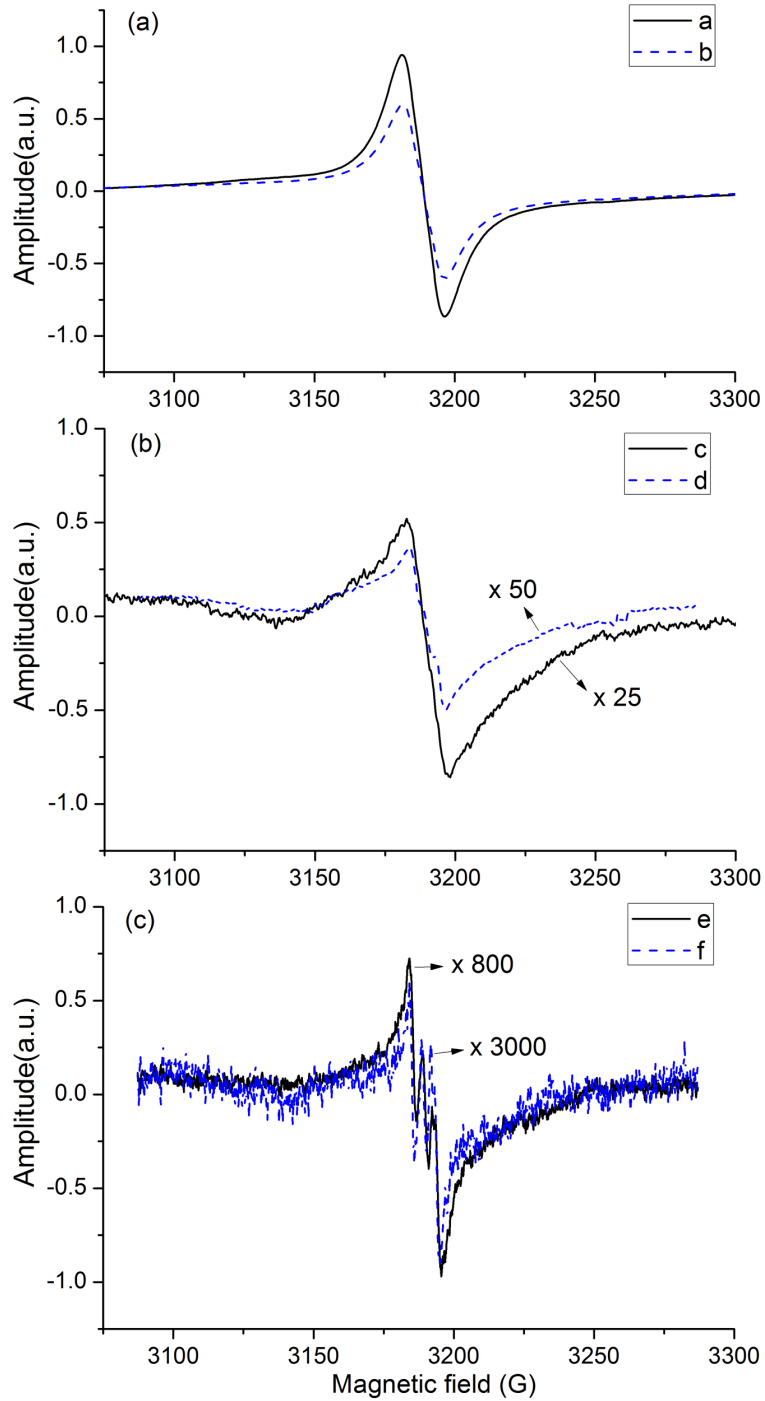


Figure 3.11: Dynamic of ESR spectra of N atoms in N-N₂-Kr-He sample during warming. The letters correspond to the moments determined by letters and arrows in Fig.10(a), i.e. a- T=1.5 K, b- T=2.7 K (before explosion), c- T=2.7 K (after explosion), d- T=5 K, e- T=15 K, f- T=27 K.

concentration of $N(^4S)$ atoms (see figure 3.9(b)) showed a slight decrease during the warming up process, providing further evidence for the recombination of the N atoms.

Explosive sample destruction occurred at around 1500 sec after the temperature was stabilized at 2.7 K. The integral of α -group emission showed a dramatic increase with one extraordinary high intensity flash during the luminescence which corresponds to the moment when the sample exploded (see figure 3.9a). The average concentration of N atoms also showed a 25 fold decrease after this explosive destruction. Further increase of the temperature in steps to 5 K, 15 K and 27 K did not induce any luminescence of the remaining sample. However, the intensity of the ESR signals at higher temperatures continued decreasing. The shapes of ESR lines at different temperatures are shown in figure 3.11. At low temperatures, the ESR signal is very broad without any resolved structure (see figure 3.11a and 3.11b). During the warming up stage, the amplitude of the broad components decreased and the resolved triplet started to be more and more prominent in the spectra although small in intensity (see figure 3.11b and c). After the temperature reached 27 K, the ESR signals of N atoms are almost entirely composed of a clear triplet shape but with intensity ~ 3000 times less than the as prepared sample. This result proves that at low average concentrations N atoms are much further apart from each other so that the line broadening is greatly reduced.

3.3.3 Optical spectra during final destruction of the sample

Figure 3.12(a) shows the dynamic spectra at the moment of the explosive destruction of the sample. The spectra were taken by the Andor spectrometer with the EMCCD camera cooled to -60°C . The exposure time was set at 3 msec. According to the figure 3.12(a), the biggest explosion happened during a short time period, within 3 msec. Figure 3.12(b) shows the optical spectrum of the biggest flash. In the spectrum, we can identify the α -group emission of N atoms, the β -group emission of O atoms and a blue band emission in the wavelength region 350 nm - 520 nm. The blue band is very diffuse

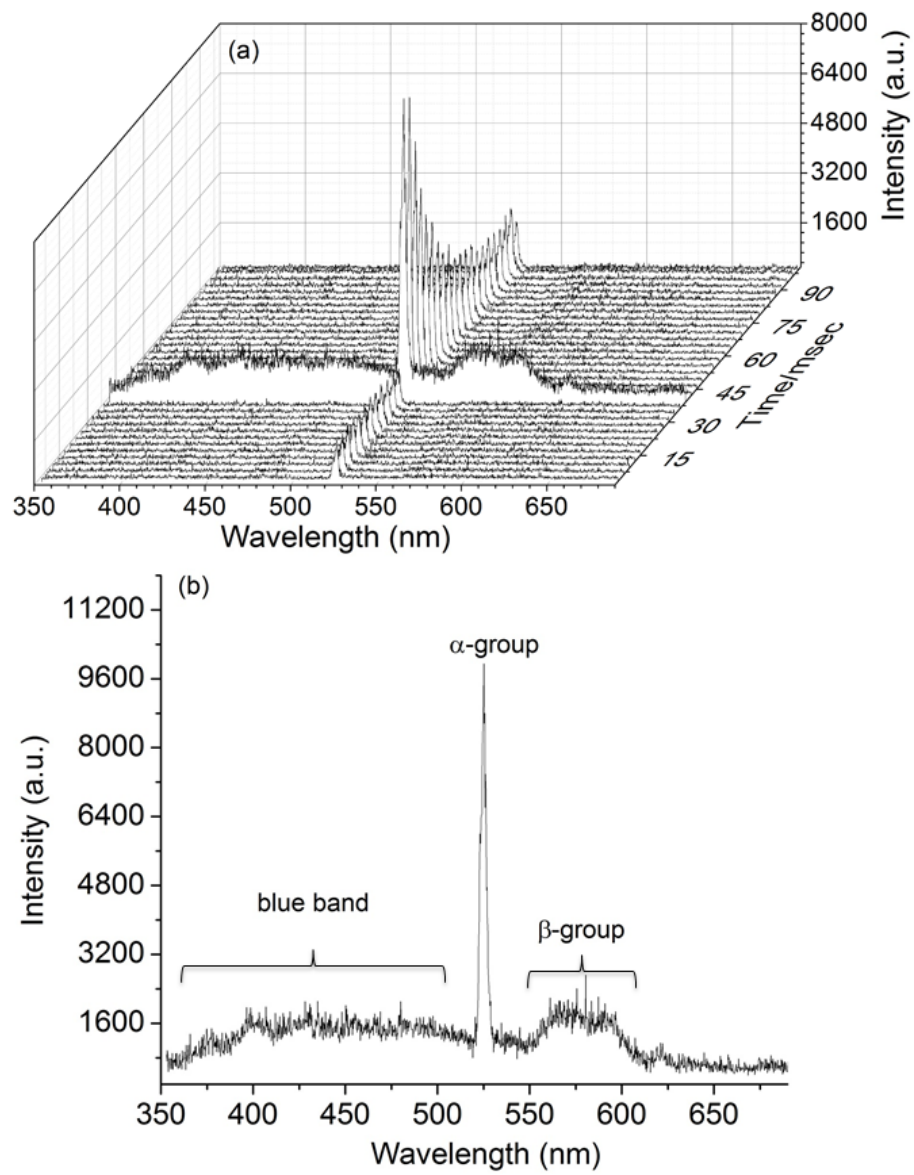


Figure 3.12: (a)Dynamic of the sample emission during explosive destruction. (b)Optical spectrum of the biggest flash during explosion.

without showing any resolved structure. We tentatively assign the blue band emission to NO₂ molecules following the work of Broida and Peyron.[73, 74]

The chemiluminescence mechanism in samples containing stabilized N and O atoms in an N₂ matrix is well known.[21, 23, 75] As temperature increases, the thermal diffusion of N atoms becomes possible and they recombine to create metastable N₂(A³Σ_u⁺) molecules. The molecular excitation may be transferred through the N₂ matrix to stabilized N and O atoms in their ground states. The emission from N(²D) and O(¹D) so excited produces the α-group and the β-group, respectively. Although, in our sample, the concentration of O atoms is about three orders of magnitude smaller than that of N atoms, the probability of the transition O(¹S-¹D) is ∼10⁵ times larger than that of N(²D-⁴S). Therefore, the β-group emission can be easily detected. When the recombination of N atoms becomes more frequent, more and more energy will be released, and as a result, it induces a chain reaction to allow a large number of N atoms to recombine. Such a large amount of released energy is transferred to excite the residual N or O atoms in a short period of time providing a very intense emission spectrum. During destruction of the sample, most of the N atoms recombine to form N₂ molecules, leaving only a small portion of the N atoms having survived inside the solid N₂ matrix formed as a result of the association of nanoclusters.

3.3.4 IHCs with N₂/Xe/He mixtures

Apart from krypton atoms, xenon atoms were also used to prepare IHC samples containing N atoms. It is known that the xenon atom has an even larger atomic weight than krypton and they both are noble gas elements. Therefore, xenon atoms should have greater van der Waals force than krypton and furthermore a higher average concentrations of N atoms is expected. Several N₂/Xe/He mixtures with different ratios have been prepared to make samples containing N atoms. Figure 3.13 shows the ESR spectra of N atoms in as-prepared samples by using these gas mixtures. The calculated

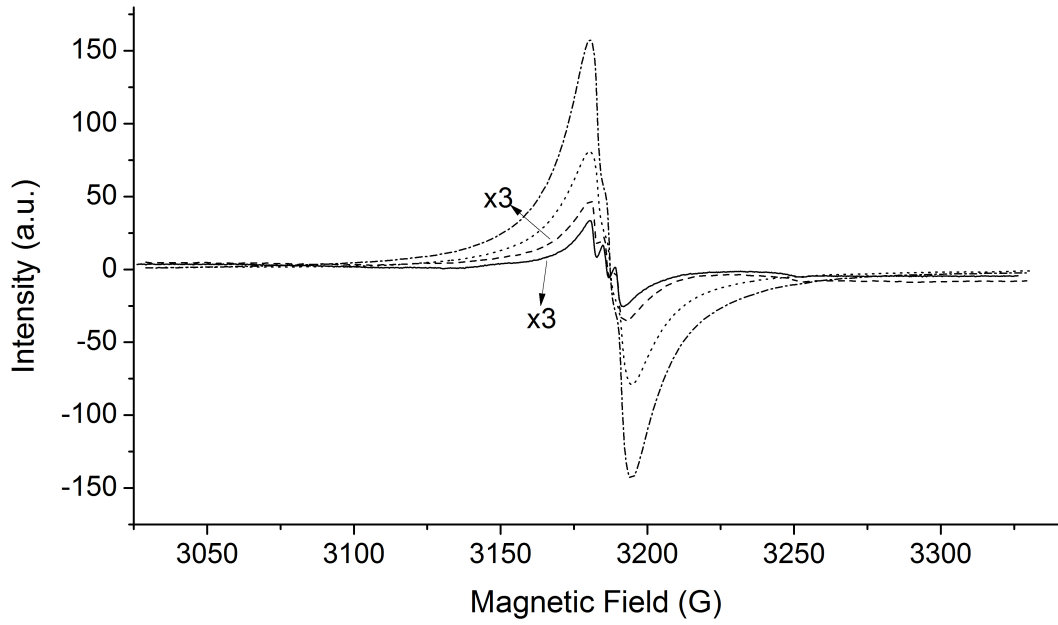


Figure 3.13: ESR spectra of $N(^4S)$ atoms in nanoclusters prepared from different mixtures. Solid- $[N_2]/[Xe]/[He]=1/50/10000$, dash- $[N_2]/[Xe]/[He]=1/10/2000$, dot- $[N_2]/[Xe]/[He]=1/1/400$, dashed dot- $[N_2]/[Xe]/[He]=10/1/2000$. For better comparison, the intensities of former two mixtures were enlarged by a factor of 3.

Table 3.3: Average concentration of N atoms in different N/N₂/Xe samples.

$[\text{N}_2]/[\text{Xe}]/[\text{He}]$	1/50/10000	1/10/2000	1/1/400	10/1/2000
Average concentration/cm ⁻³	5.21×10^{17}	8.92×10^{17}	1.91×10^{18}	3.49×10^{18}

average concentrations of N atoms in the samples are listed in Table 3.3. From Table 3.3 we can see that with more content of N₂ in the gas mixture, the average concentration of N atoms stabilized in the samples is increasing, which indicates that N atoms are efficiently captured in the nitrogen-xenon nanoclusters. ESR spectra presented in figure 3.13 have different shapes. We can see more resolved triplets in the spectra for the samples prepared from gas mixtures with low content of N₂, while line broadening makes the triplet structure at the center almost impossible to detect for the high content nitrogen samples. For the high concentration samples, the wings could span about 100 G. The linewidth broadening definitely means that the local concentration of N atoms is very high and that the dipole-dipole interaction between neighboring spins dominates the spectra of the samples prepared from gas mixtures with a high content of N₂. However, even for samples with the highest content of N₂, i.e. [N₂]/[Xe]/[He]= 10/1/2000, there is still a barely seen triplet overlapping with the broad central region. This means that for these samples the N atoms are embedded in different lattice environments in the nanoclusters which provide different features in the ESR spectrum.

For a better understanding of the environment of trapped N atoms in the sample, we also tried to decompose the ESR spectra using a combination of several simple functions. As an example, in figure 3.14, the analysis is shown for the ESR spectrum of N atoms stabilized in nitrogen-xenon-helium samples prepared from a mixture [N₂]/[Xe]/[He]= 1/1/400. We obtained a good fit for the experimental spectrum when we used a sum of three triplets of Lorentzian functions with spacing 4.2 G between the centers of these functions, but with different linewidths; 5.6 G, 16 G and 45 G. The ratio of double integrations corresponding to these Lorentzian triplets is about 1/8/34, which indicates that most of the N atoms are stabilized in the regions with higher local concentrations: $\sim 19\%$ with $n_{loc} = 3.63 \times 10^{20} \text{ cm}^{-3}$ and $\sim 77\%$ with $n_{loc} = 1 \times 10^{21} \text{ cm}^{-3}$. Table 3.4 shows the decomposition analysis of all the samples we investigated.

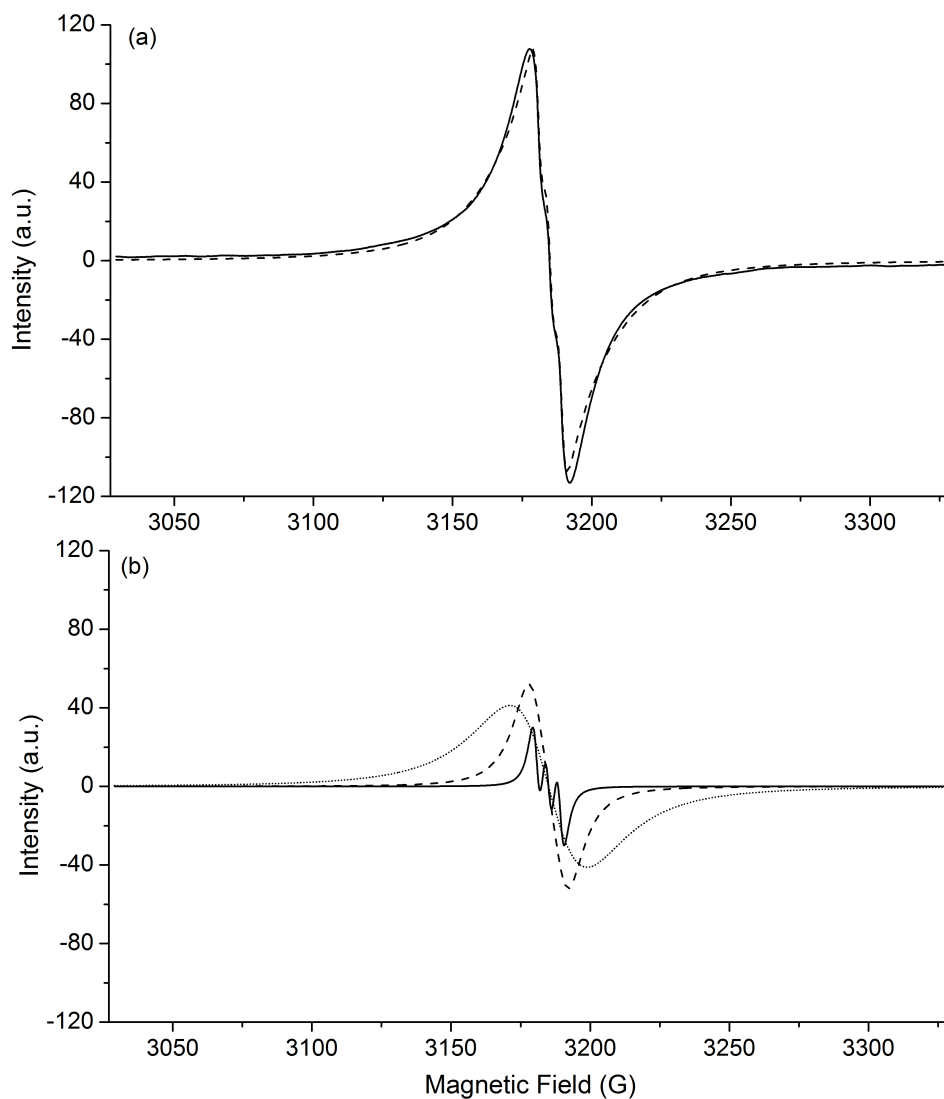


Figure 3.14: Decomposition of ESR spectra for sample prepared by mixture $\text{N}_2/\text{Xe}/\text{He}=1/1/400$. a) Solid- experimental ESR spectrum of N atoms for as-prepared sample, dash- the sum of the fitting lines. b) Three triplets of fitting lines used for decomposition of the experimental ESR spectrum: solid- triplet of Lorentzian lines with width 5.6 G , dash- triplet of Lorentzian lines with width 16 G, dot- triplet of Lorentzian lines with width 45 G. The hyperfine splitting for all triplets is 4.2 G.

Table 3.4: Analysis of ESR spectra of N atoms for different N/N₂/Xe samples, where A is the hyperfine structure constant and ΔH_{pp} is the peak to peak width.

Sample	Curve Type	A/G	$\Delta H_{pp}/G$	Local concentration	Weight
[N ₂]:[Xe]:[He] =1:50:10000	Lorentzian	4.2	5.7	1.27×10^{20}	39%
	Lorentzian	4.2	18	4.09×10^{19}	61%
[N ₂]:[Xe]:[He] =1:10:2000	Lorentzian	4.2	5.7	1.27×10^{20}	13%
	Lorentzian	4.2	18	4.09×10^{20}	13%
	Lorentzian	4.97	30	6.81×10^{20}	74%
[N ₂]:[Xe]:[He] =1:1:400	Lorentzian	4.2	5.6	1.27×10^{21}	2.3%
	Lorentzian	4.2	16	3.63×10^{19}	18.6%
	Lorentzian	4.2	45	1.02×10^{21}	79.1%
[N ₂]:[Xe]:[He] =10:1:2000	Lorentzian	4.2	5.7	1.27×10^{20}	4%
	Lorentzian	4.2	16	3.63×10^{20}	23.5%
	Lorentzian	4.20	35	7.95×10^{20}	72.5%

3.4 Discussion and conclusion

This study demonstrates the advantages of the method of injecting atoms into superfluid helium for producing samples with high concentrations of stabilized atoms. The addition of Kr atoms to the condensed N_2 -He gas mixture leads to a record high average ($\sim 5 \times 10^{19} \text{ cm}^{-3}$) and local ($\sim 2 \times 10^{21} \text{ cm}^{-3}$) concentration of stabilized N atoms in N- N_2 -Kr-He condensates. Observation of three different types of the environments for N atoms in N- N_2 -Kr-He condensates might be explained by a shell structure of the nanoclusters which formed the IHCs. (See figure 3.15) Such a situation was predicted[76] and later was established for atomic hydrogen atoms in matrix isolated H-Kr clusters.[27, 52, 53] During injection of the nitrogen-kryptonhelium jet into bulk superfluid helium at the early stages of cooling in the jet, the Kr atoms form clusters due to strong Van der Waals interactions between the Kr atoms. At the next stage, the N_2 molecules and N atoms bind to the surface of the Kr nanoclusters. The resulting structure of krypton-nitrogen clusters is shown in figure . From the results of an analysis of the shapes of the ESR spectra, we can conclude that part of the N atoms (0.6-25%) reside inside the Kr clusters, another portion of the N atoms reside in the N_2 layer (0.1-15%) covering the Kr core and the vast majority of the N atoms (75-85%) reside on the surfaces of N_2 layers. Thus the highest concentration of N atoms appears to be in this outer surface layer.

A great deal of progress has been made in the field of matrix isolation since the early experiments by Gordon, Mezhov-Deglin and Pugachev in 1974.[1] In the present discussion, we have described recent success in obtaining exceptionally high local and average concentrations of nitrogen atoms in impurity-helium condensates. Local concentrations of $\sim 2 \times 10^{21} \text{ cm}^{-3}$ and average concentrations of $\sim 5 \times 10^{19} \text{ cm}^{-3}$ were achieved. This means that a very large amount of chemical energy can be stored in these samples, with energies comparable to or exceeding those stored in the best chemical explosives. The

energy released by the recombination of two nitrogen atoms into a nitrogen molecule is 9.8 eV. The N atoms were mainly localized on the surfaces of the nanoclusters with much smaller populations contained in the cluster interiors. The ESR line shapes for N-Kr samples differed from those of N-N₂ samples, possibly indicating a different distribution of N atoms in the nanoclusters for the two cases.

The observed concentrations were high enough to permit observation of $\Delta M = 2$ spin pair radical transitions (see figure 3.5) corresponding to half the Larmor field used to observe the main ESR line. Dipolar coupling between nearby atoms is responsible for this phenomenon. The large size of the ESR signal for spin pair radicals indicates that a significant fraction of N atoms are participating in this process. This would suggest the possibility that magnetic phase transitions will occur at lower temperatures. It is also possible that if somewhat higher local concentrations can be achieved, the effect of exchange narrowing, a short range phenomenon, might be observed in this system.

Similar experiments have been performed for the samples prepared from N₂/Xe/He gas mixtures. Since Xe atom has atomic weight 131, which is much bigger than the Kr atomic weight 84, it is expected that even higher efficiencies should be obtained for capturing N atoms. However, only average concentrations as large as 3.49×10^{18} have been achieved, which is about one order of magnitude lower than that for N-N₂-Kr samples. This is very surprising, because the IHC samples are formed by van der Waals forces between atoms and molecules. Heavier Xe atoms have even greater van der Waals forces than Kr atoms and as a result are more efficient in capturing nitrogen atoms and molecules. We tentatively assign the reason for this inefficiency to the fact that we still have not found the best recipe ratio for the N₂/Xe/He gas mixtures. Another possible explanation is that the Xe atoms have different influence over the discharge process before the sample is formed so that the dissociation of the N₂ molecules is not very efficient. Further investigation is needed to make this question clear.

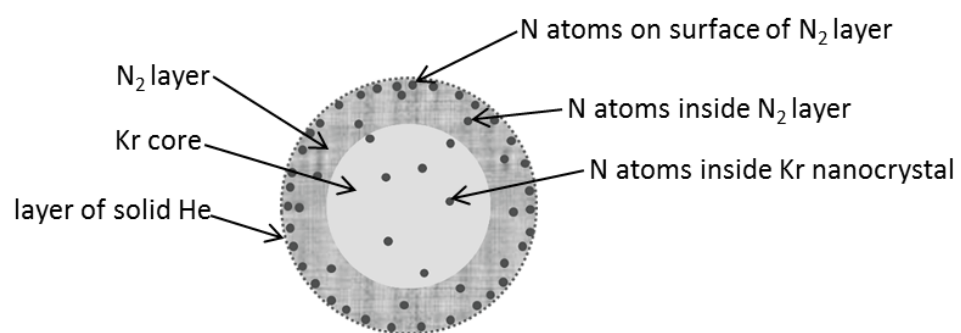


Figure 3.15: Structure of nitrogen-krypton-helium nanoclusters with stabilized N atoms

Also, simultaneous measurements of ESR and optical spectra have been performed for samples prepared from the $N_2/Kr/He$ mixtures. It is observed that when the temperature is stabilized at 1.35 K after sample preparation, the ESR signals do not show any change and no luminescence is observed. During the sample warming up process, α -group emission from $N(^2D)$ atoms is observed accompanying the decrease of the average concentration of N atoms from the ESR measurement. This indicates the recombination process is induced by the temperature increase and thus causes the decrease of the concentration of $N(^4S)$ atoms. An explosive emission happened when the temperature was stabilized at 2.7 K for some time. The spectrum consists of several bands including the α -group, the β -group and a broad blue band emission. The explosive emission was initiated by the destructive collapse of the sample structure so that a large number of recombination events for N atoms occurred, releasing huge energy. This energy was transferred by the matrix to different impurity species, exciting them so that a combination of emission bands were observed.

The capabilities of ESR and optical studies at cryogenic temperatures provided by the setup can be applied to a wide range of research. For example, this setup can also be used for optically detected magnetic resonance (ODMR). ODMR is a double resonance technique which combines optical measurements (fluorescence, phosphorescence, absorption) with electron spin resonance spectroscopy. After the first triplet-state ODMR experiments in zero magnetic field were reported in 1968 by Schmidt and van der Waals,[77] the number of double resonance studies on excited triplet states grew rapidly. Also, ODMR has been an important tool to investigate both defects and carrier recombination processes in semiconductor films due to its high sensitivity and high energy resolution.[78] Another important application of ODMR is to study the fluorescence of nitrogen-vacancy defect centers in diamond. Magnetic resonance on single centers at room temperature has recently been demonstrated[79] and low temperature measurements are expected to reveal interesting new information on magnetic ordering.

4. PERCOLATION IN AGGREGATES OF NANOCLOUDS IMMERSSED IN SUPERFLUID HELIUM*

Impurity-helium condensates created by injection of hydrogen (deuterium) atoms and molecules along with rare gas (RG) atoms (Ne and Kr) into superfluid ^4He have been studied via electron spin resonance (ESR) techniques. Measurements of the ground-state spectroscopic parameters of hydrogen and deuterium atoms show that the nanoclusters have a shell structure. H and D atoms reside in solid molecular layers of H_2 and D_2 , respectively. These layers form on the surfaces of RG (Ne or Kr) nanoclusters. By monitoring the recombination of H atoms in the collection of hydrogen-neon nanoclusters, we show that nanoclusters form a gel-like porous structure which enables the H atoms to be transported through the structure via percolation. Observation of percolation in the collection of nanoclusters containing stabilized hydrogen atoms opens new possibilities for a search for macroscopic collective quantum phenomena at ultralow temperatures accessible by a dilution refrigerator.

4.1 Introduction

The investigation of H atoms in a molecular H_2 matrix is a promising area of research. H atoms can move through solid H_2 via the tunneling exchange reaction $\text{H} + \text{H}_2 \rightarrow \text{H}_2 + \text{H}$. [80, 44, 81, 82] This phenomenon gives rise to the delocalization of H atoms and it opens up the possibility for the observation of quantum phenomena. For the observation of collective quantum phenomena, the thermal de Broglie wavelength must be longer than the distance between H atoms. High concentrations of H atoms and low temperatures are essential for this criterion to be satisfied. Unfortunately the same exchange reaction can lead to a recombination driven decay of the H atom concentration

*Part of this section is reprinted with permission from "Percolation in aggregates of nanoclusters immersed in superfluid helium", by S.Mao, A.Meraki, R.E.Boltnev, V.V.Khmelenko, and D.M.Lee, 2014. *Phys. Rev. B*, **89**, 144301, Copyright 2014 by APS.

at $T \geq 1$ K.[82] Recently it was found that decreasing the temperature to 150 mK leads to significant suppression of the H atom recombination process.[83] This makes a search for quantum phenomena possible in systems with high concentrations of H atoms at low temperatures in thin and thick H_2 films.[83, 84, 85, 86] Unusual behavior of H atoms in H_2 films was found at temperatures ~ 150 mK. The significant departure from the Boltzmann distribution of the relative populations of the two lowest hyperfine levels of H atoms was observed[83] at atom concentrations $\sim 10^{18} \text{cm}^{-3}$. A complete explanation of this effect will require additional experiments at higher H atom concentrations to test the quantum overlap hypothesis and to observe additional quantum effects.

Impurity-helium condensates (IHCs) consist of nanoscale clusters which adhere together to form a gel like solid.[17, 4, 87, 28] Each cluster is coated with a thin layer of solid helium which greatly retards the recombination of the stabilized atoms. IHCs are the best candidates for achieving record high concentrations of stabilized atoms.[2, 13, 27] The highest average ($\sim 10^{19} \text{cm}^{-3}$) and local ($\sim 6 \times 10^{19} \text{cm}^{-3}$) concentrations of H atoms were obtained in H_2 films formed in hydrogen-krypton helium samples.[27] The existence of a layer of H_2 molecules covering the Kr nanocluster surface provides an arena for the study of the diffusion and tunnelling of H atoms.[27] To observe macroscopic quantum effects in this system, it is important to determine whether or not the H atoms can move relatively freely between the nanoclusters. This process is known as percolation and is an important feature for the observation of macroscopic quantum overlap phenomena in impurity-helium condensates containing high concentrations of stabilized H atoms.

In this work, we present experimental studies for percolation between nanoclusters in IHCs containing stabilized H and D atoms. Our approach is based on the observation of H atom recombination or exchange tunnelling reactions between atoms and molecules of hydrogen isotopes from neighboring nanoclusters in the IHC samples using the ESR technique. H and D atoms each exhibit a different ESR spectrum, which makes it

straightforward to study the kinetics of the reactions involving these atoms. We studied percolation for two different types of IHCs in our experiments.

First, we studied the possibility of the transfer of H atoms between nanoclusters in hydrogen-neon-helium condensates. For this purpose, we prepared IHC samples in which the number of stabilized H atoms was less than the number of nanoclusters in the sample and studied the process of H atom recombination in these samples. We found that the recombination process continues even when the number of H atoms is 5 times less than the number of nanoclusters. This observation provides strong evidence for percolation between nanoclusters in hydrogen-neon-helium condensates.

Second, we studied the possibility of observing the transfer of D atoms in the layered IHCs in which layers of D-D₂ nanoclusters alternate with layers of H₂-Ne or H₂-Kr nanoclusters. If D atoms migrate to neighboring nanoclusters, the exchange tunnelling chemical reactions with H₂ molecules should lead to increasing concentrations of H atoms in the samples, which can be easily observed by ESR. In as-prepared layered samples we did not observe any evidence for D atoms traveling between nanoclusters. Annealing of the layered samples to 2.6 K results in the onset of the exchange tunnelling reactions, providing evidence of apparent connections between nanoclusters in these layered samples.

4.2 Theoretical background

In this section, we will introduce the theoretical background of the hyperfine splitting of hydrogen atoms, dipolar coupling of a hydrogen electron and neighboring nucleus, and quantum exchange chemical reactions. It will help us to explain the effects taking place in the experiments, such as satellite lines and the change of average concentrations of hydrogen atoms.

4.2.1 Hyperfine structure of hydrogen atom

A hydrogen atom has one unpaired electron with spin $\mathbf{S} = \frac{1}{2}$ orbiting around the nucleus with nuclear spin $\mathbf{I} = \frac{1}{2}$. The behavior of an atom in an external magnetic field \mathbf{H} is described by the equation 3.1 in section 3, where the first two terms are just the Zeeman energies of electrons and nuclei in a magnetic field. The last term is the hyperfine interaction of the electron spin \mathbf{S} and the nuclear spin \mathbf{I} . In systems with only one electron, Fermi shows that the interaction is isotropic and given by equation (3.2) in section 3. This describes so the called Fermi contact interaction. It is caused by the fact that $S = \frac{1}{2}$ electrons have nonzero probability of being at the nucleus. This probability is proportional to $|\Psi(0)|^2$, the electron wavefunction evaluated at the nucleus. For the hydrogen 1s wavefunctions,

$$\Psi_{1s} = \left(\frac{1}{\pi r_0^3}\right)^{\frac{1}{2}} \exp\left(-\frac{r}{r_0}\right), \quad (4.1)$$

is nonzero at $r = 0$. Here r_0 is the radius of the first Bohr orbit.

In a weak external magnetic field the $h\mathbf{AI} \cdot \mathbf{J}$ term in the equation 3.1 is largest, and the angular momenta indicated by \mathbf{I} and \mathbf{J} are coupled to form a resultant $\mathbf{F} = \mathbf{I} + \mathbf{J}$. F , the good quantum number in this limit, takes the values $I+J, I+J-1, \dots, |I-J|$. For each value of F there are $2F+1$ projections of \mathbf{F} in the field direction indicated by $m_F = F, F-1, \dots, -F$. In a very strong field, corresponding to the Paschen-Back effect, \mathbf{I} and \mathbf{J} are effectively acted upon separately by H , i.e., they are decoupled. F and m_F are no longer good quantum numbers and are replaced by m_J and m_I as defined previously. The numbers of levels is the same as in the weak field but is now $(2J+1)(2I+1)$. In intermediate fields m_F is replaced by $m = m_I + m_J$, and the Breit-Rabi equation,[88] which gives the energy levels, $E(F, m)$ over all fields, is, for $J = \frac{1}{2}$:

$$E(F, m) = \frac{-\Delta W}{2(2I+1)} - \left(\frac{\mu_I}{I}\right)Hm \pm \frac{\Delta W}{2} \sqrt{1 + \frac{4m}{2I+1}x + x^2} \quad (4.2)$$

where

$$\Delta W = h\left(\frac{A}{2}\right)(2I + 1), x = \frac{(g_J\beta_e - \mu_I/I)H}{\Delta W} \quad (4.3)$$

The plus sign in the equation (4.2) applies for $F = I + \frac{1}{2}$ and $m = +(I + \frac{1}{2}), \dots, -(I + \frac{1}{2})$, and the minus sign applies for $F = I - \frac{1}{2}$ and $m = +(I - \frac{1}{2}), \dots, -(I - \frac{1}{2})$. ΔW is the energy level spacing at zero magnetic field, which is $\frac{\Delta W}{h} = 1420$ MHz for hydrogen atoms.

Also, by solving the equation 3.1, we can calculate the energy eigenstates of the hydrogen atoms: $|m_S = 1/2, m_I = 1/2\rangle = |\uparrow\uparrow\rangle, |\downarrow\downarrow\rangle, |\uparrow\downarrow + \eta \downarrow\uparrow\rangle, |\downarrow\uparrow - \eta \uparrow\downarrow\rangle$. Here $\eta = \frac{\Delta W}{2g\beta H_0}$ determines the mixing of states $|\uparrow\downarrow\rangle$ and $|\downarrow\uparrow\rangle$ due to the hyperfine interaction. At a magnetic field of 3 kG, the mixing coefficient η equals to 0.077, indicating a substantial amount of mixing.

Figure 4.1 shows the energy levels of a hydrogen atom in external magnetic field, where \mathcal{P}_0 and \mathcal{P}_1 are the transition probabilities between the hyperfine states. According to the Fermi golden rule, these transition probabilities are calculated as:

$$\begin{aligned} \mathcal{P}(|\uparrow\uparrow\rangle \leftrightarrow |\downarrow\uparrow - \eta \uparrow\downarrow\rangle) &= \text{const}(H_{1x}^2 + H_{1y}^2)/4; \\ \mathcal{P}(|\downarrow\downarrow\rangle \leftrightarrow |\uparrow\downarrow + \eta \downarrow\uparrow\rangle) &= \text{const}(H_{1x}^2 + H_{1y}^2)/4; \\ \mathcal{P}(|\downarrow\uparrow - \eta \uparrow\downarrow\rangle \leftrightarrow |\uparrow\downarrow + \eta \downarrow\uparrow\rangle) &= \text{const} \cdot H_{1z}^2\eta^2; \\ \mathcal{P}(|\uparrow\uparrow\rangle \leftrightarrow |\downarrow\downarrow\rangle) &= 0 \end{aligned} \quad (4.4)$$

where H_{1x} and H_{1y} are x and y components of the microwave magnetic field H_1 . By calculating the transition probabilities we have effectively derived the magnetic dipole selection rules. The first two transitions have equal probabilities. They are transverse transitions because the microwave magnetic field H_1 has to be applied perpendicular to the steady magnetic field H_0 which is in the z -direction. On the other hand, the third transition is longitudinal. It is possible to induce only when H_1 has a component parallel to H_0 . This transition is called forbidden because of its suppression by the factor of

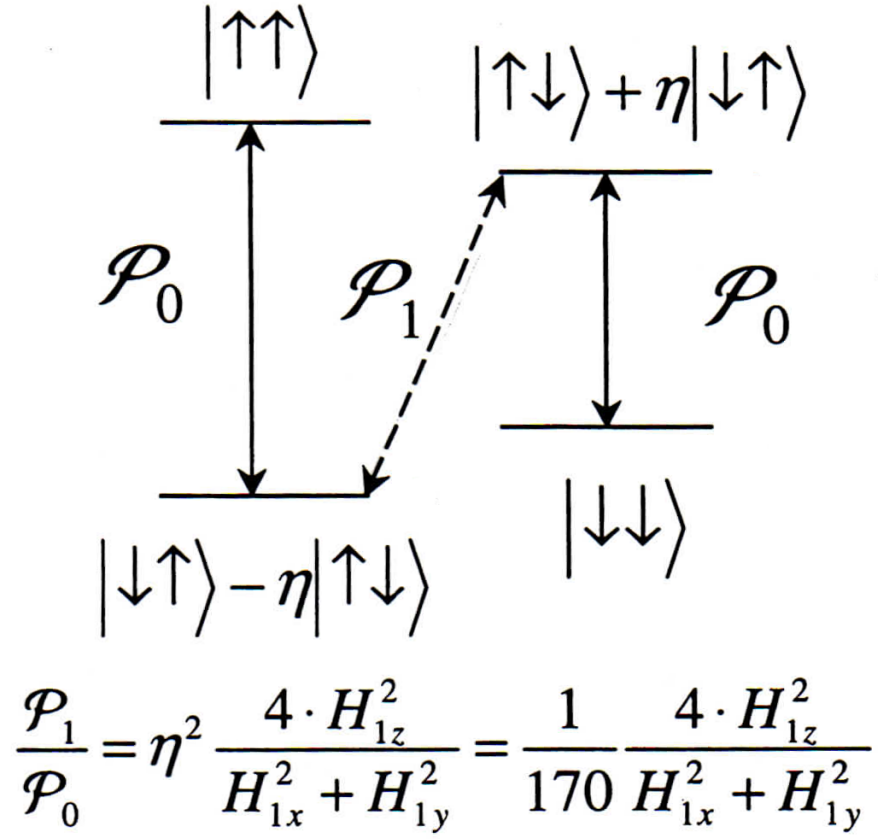


Figure 4.1: Transitions between hydrogen hyperfine levels calculated from Fermi golden rule. First entry in a ket is the electron spin state and the second entry corresponds to the spin state of a nuclear.

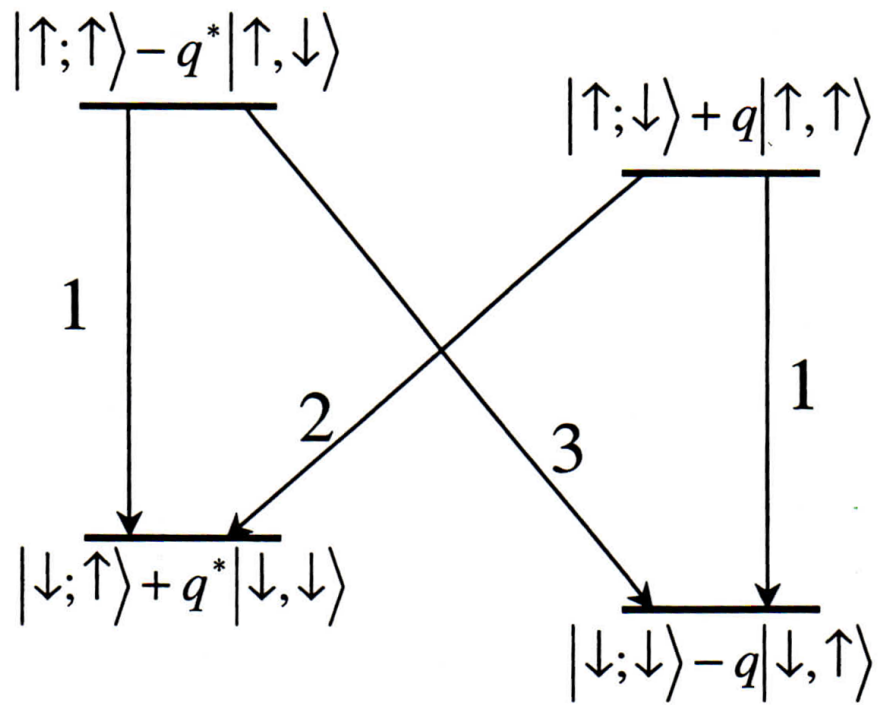


Figure 4.2: Energy spectrum of nucleus-electron pair of spins 1/2 in a high field coupled by dipole-dipole interaction.

η^2 compared to the first two allowed transitions ($\eta^2 = (\frac{\Delta W}{2g\beta H_0})^2 = \frac{1}{170}$ at $H_0 = 3$ kG). However, it was still observed in the IHC sample prepared by the gas mixture $[\text{H}_2]:[\text{D}_2]:[\text{He}]=1:4:100$ by S.I. Kiselev et al..[32] The last transition has probability zero, which indicates that it is strictly forbidden.

4.2.2 Dipolar coupling of hydrogen electron and neighboring nuclei

In the previous section the strong hyperfine coupling of the electron spin and nuclear spin of the hydrogen atom was considered. Another interesting case which takes place in our Im-He solids is the dipolar coupling between the electron spin \mathbf{S} of a hydrogen atom and the spin of a proton \mathbf{I} of a neighboring molecule separated from each other by a distance r . The spin Hamiltonian of this system in a magnetic field is given by:

$$\mathcal{H} = g_J\beta_e\mathbf{H} \cdot \mathbf{J} - g_I\beta_n\mathbf{H} \cdot \mathbf{I} + g_e\beta_e g_I\beta_n \left[\frac{\mathbf{I} \cdot \mathbf{S}}{r^3} - \frac{3(\mathbf{I} \cdot \mathbf{r})(\mathbf{S} \cdot \mathbf{r})}{r^5} \right] \quad (4.5)$$

As for the case of hyperfine coupling, the first two terms are Zeeman energies of the electron and nuclei in magnetic field \mathbf{H} . The last term is the dipole-dipole interaction energy. In fields large compared with the line width (this is certainly true in our ESR experiments!), the first two terms are dominant and the energy levels are given by:

$$E(m_S, m_I) = g_e\beta_e m_S H_0 + g_I\beta_n m_I H_0 \quad (4.6)$$

This means that each of the electron levels is split into two levels separated by $g_I\beta_n H_0$ for a proton associated with the ortho H_2 molecule as given by equation 4.5. Just as for the hyperfine case, the electronic states become not only split, but also slightly mixed by the amount $q \sim (\text{dipole energy})/(\text{nuclear Zeeman energy})$. Therefore the state $|\uparrow\uparrow\rangle$ before the dipolar interaction was turned on will become $|\uparrow\uparrow\rangle - q |\uparrow\downarrow\rangle$ (the exact expression for q is shown later in the section). Similar transformations will take place with the rest of the states. A diagram of these states is shown in figure 4.2. Using

exactly the same procedures as in hyperfine case, we find that magnetic dipole selection rules allow transitions marked by arrows in figure 4.2. Transitions designated by '1' are ordinary electron spin flip transitions at field \mathbf{H} determined by $h\nu_0 = g_e\beta_e H_0 \pm g_I\beta_n H_0$. Their intensities are $I \sim q^2 I_0$. Jeffries calculated the value of q for electron and proton coupled by dipole interaction:

$$q = \frac{3}{4}(g_e\beta_e/H_0 r^3)\sin\theta\cos\theta e^{-i\phi} \quad (4.7)$$

This leads to the observation of a satellite line on each side of the main ESR signals. For hydrogen atoms, the separation between the satellite lines and the low field ESR line is about 4.6 G and that for the high field line is about 5.3 G. Trammell et al.[89] averaged q^2 and calculated the ratio of the main and satellite line intensities:

$$\frac{I_{satellite}}{I_{main}} = \frac{3}{20}(g_e\beta_e/H_0)^2 \langle r \rangle^{-6} n \quad (4.8)$$

Here n is the number of protons next to a hydrogen atom and $\langle r \rangle$ is the average distance from the atom to these protons. Assuming that there are n protons neighboring a hydrogen atom we can solve equation 4.8 for $\langle r \rangle$:

$$\langle r \rangle = 0.73(g_e\beta_e/H_0)^{1/3} (I_{satellite}/I_{main})^{-1/6} \quad (4.9)$$

The first satellite lines were observed in ESR experiments involving atomic hydrogen in frozen acids. Satellite lines in a system similar to ours was observed for the first time by Miyazaki et al.[90] for H and D atoms contained in solid hydrogen. The atoms were produced in very low concentrations by γ -irradiation of solid H_2 , HD, and D_2 . As described above, the satellites were associated with forbidden ESR transitions involving an electron spin flip of a hydrogen or deuterium atom and a simultaneous spin flip of a proton on a neighboring HD or ortho-hydrogen molecule.

Table 4.1: Rate constants k for atom exchange reactions calculated by Takayanagi and Sato

Reactions	$k(\text{cm}^3\text{mol}^{-1}\text{s}^{-1})$
$\text{H}+\text{H}_2\rightarrow\text{H}_2+\text{H}$	4.6×10^{-1}
$\text{H}+\text{HD}\rightarrow\text{HD}+\text{H}$	2.1×10^{-3}
$\text{D}+\text{D}_2\rightarrow\text{D}_2+\text{D}$	7.3×10^{-7}
$\text{D}+\text{H}_2\rightarrow\text{DH}+\text{H}$	1.2×10^0
$\text{D}+\text{HD}\rightarrow\text{DH}+\text{H}$	4.5×10^{-4}
$\text{D}+\text{DH}\rightarrow\text{D}_2+\text{H}$	2.7×10^{-3}

4.2.3 Quantum exchange chemical reactions

The exchange chemical reactions were hypothesized by Gordon et al.[31] for impurity-helium solids to explain the unexpectedly high initial populations of hydrogen atoms when impurity-helium solids containing hydrogen and deuterium atoms were formed in their experiments. They were not able to determine the time evolution of the concentrations of the two species in their experiments, however. Later these chemical reactions have been employed to study chemical reactions in solid hydrogen matrices by Lukashevich et al.[91] via deposition of the products of H_2 and D_2 passing through a radio frequency discharge and Miyazaki et al.[80, 92] in experiments on γ -irradiated samples of solid mixtures of H_2 and D_2 . Both of these groups monitored the populations of atomic hydrogen and deuterium as a function of time following the deposition or irradiation. Although the concentrations of hydrogen and deuterium atoms were very dilute in their work, time evolutions were found to be similar to the results of our experiments.

Since all of the experiments involving these chemical reactions are performed at liquid helium temperatures, thermally activated processes can be effectively ruled out. When a deuterium atom is adjacent to an H_2 molecular, an intermediate state involving the metastable compound molecule HDH is formed. Then a hydrogen atom is emitted, leaving behind a stable HD molecule. The potential barrier for the formation of the compound molecule is typically of order 4000 K[93] which is for greater than liquid helium temperatures (1-4 K), justifying our statement that the reactions are not thermally activated. Therefore the reactions can be driven only by quantum mechanical tunnelling and are thus classified as exchange tunnelling reactions.

Quantum tunnelling reactions involving atoms and molecules of hydrogen isotopes have been extensively studied by theorists. These systems are quite unique for their simplicity. They are almost the only ones where the reaction rates can be calculated computationally. A number of groups used similar approaches as to calculate the rates

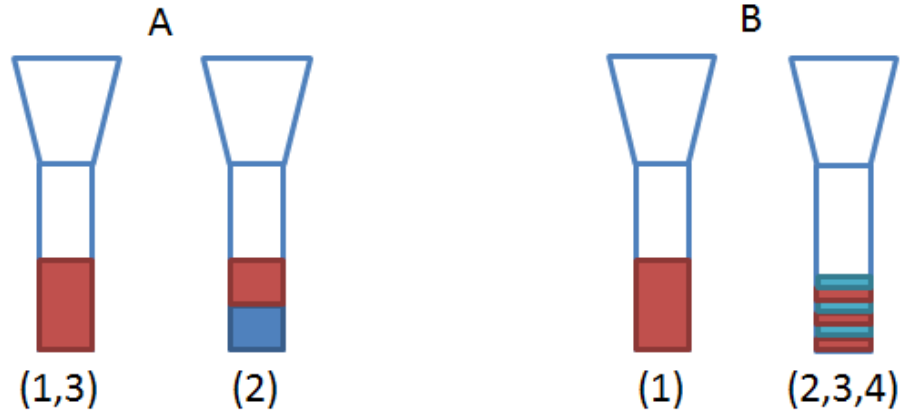


Figure 4.3: The position of the samples in the beaker and the structure of the samples. In experiments A the gas mixture used was $[\text{H}_2]:[\text{Ne}]:[\text{He}]=4:1:500$. In experiment A1 and A3 all samples were prepared by passing the entire condensing gas mixture through the discharge zone. In experiment A2 the lower part of the sample was prepared without discharge action. The gas mixtures used in experiment B are $[\text{D}_2]:[\text{He}]=1:100$ for the red layers of B1, B2, B3 and $[\text{D}_2]:[\text{He}]=1:25$ for the red layer of B4 with discharge action; the mixtures for blue layers for B2, B3 and B4 are $[\text{H}_2]:[\text{Kr}]:[\text{He}]=1:5:150$, $[\text{H}_2]:[\text{Ne}]:[\text{He}]=1:5:150$ and $[\text{H}_2]:[\text{Ne}]:[\text{He}]=1:5:150$, respectively, *without* discharge action.

of quantum tunnelling reactions involving atomic hydrogen (deuterium) and molecular H_2 , HD and D_2 . [94, 95, 96, 97, 98] In these studies, the authors start with the simplest system $\text{H}+\text{H}_2$ and then extend the results obtained to the more complicated systems, for example $\text{H}+\text{D}_2$ and $\text{D}+\text{H}_2$. The rate constant for the $\text{H}+\text{H}_2$ reaction was calculated using the LSTH (Liu-Siegbahn-Truhlar-Horowitz) potential surface of the H_3 complex. [99] First, the steepest descent path on this surface was calculated (this corresponds to the minimum-energy path, MEP). [95] Then, the zero point energy of stretching and bending vibrations was added to the MEP. The reaction rate was calculated using transition state theory outlined by Garrett and Truhlar. [100] The results obtained by different groups are in reasonable agreement. Table 4.1 summarizes the calculations of rate constants for different exchange reactions done by Takayanagi and Sato. [96]

4.3 Experimental results

The experimental setup for preparing and investigating stabilized atoms in IHCs at low temperatures has been described in more detail in the section 2. Two sets of samples were prepared with set A only containing H_2 molecules and set B containing both H_2 and D_2 molecules. The reason for using Ne atoms in set A samples is because that it is impossible to prepare IHCs purely composed of H_2 molecules due to its smaller density than liquid helium. Without the aid of Ne atoms as heavier species, H_2 nanoclusters cannot sink into superfluid helium. The position of the sample in the beaker and the constitution of each layer in the sample are illustrated in figure 4.3. Here we only present the experimental results.

4.3.1 Studies of condensates formed by $\text{H-H}_2\text{-Ne-He}$ nanoclusters

We performed long term (up to 10 hours) ESR investigations of the three samples formed by injecting the gas mixture $[\text{H}_2]:[\text{Ne}]:[\text{He}] = 4:1:500$ into HeII. The structure

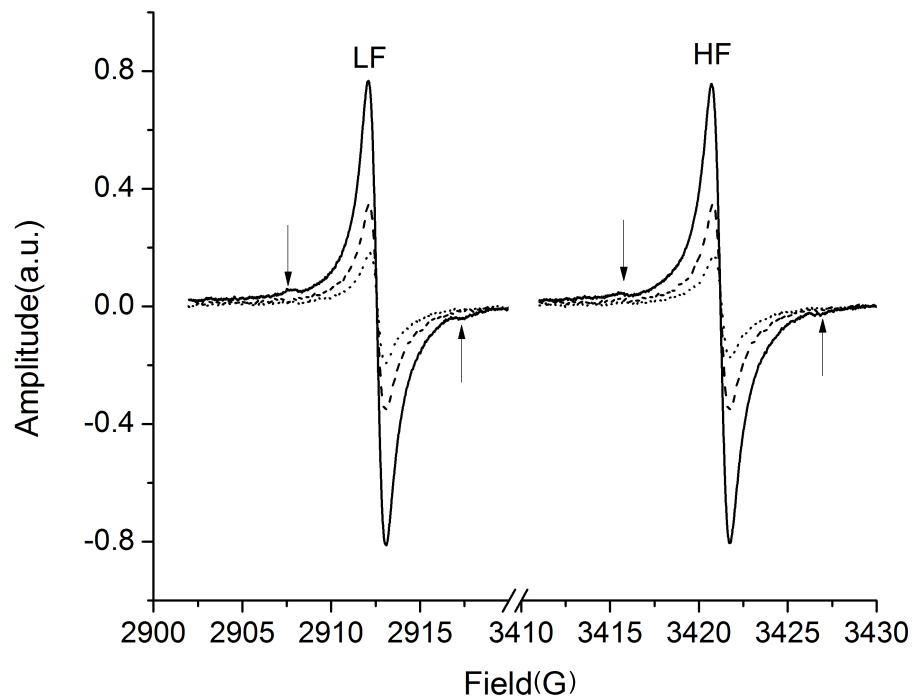


Figure 4.4: The ESR spectra of H atoms in sample A1 showing the high field and low field lines: for as prepared sample (solid), after waiting time of 4 hours (dashed) and after waiting time of 8 hours (dotted). The arrows show the satellite lines associated with nuclear spin flips on ortho H₂ molecules.[89]

of the samples is illustrated in figure 4.3A. Two samples (A1 and A3) were prepared by using the discharge during the period of sample accumulation. The radiofrequency discharge provided the atomic hydrogen through dissociation of H_2 , and soon afterward the H atoms were captured by nanoclusters growing in the cold helium gas jet. The H_2 -Ne-He nanoclusters were then collected at the bottom of the quartz beaker for ESR registration of H atoms. If the mixture is passed through the capillary without discharge, we should not expect the presence of free H atoms in the sample. On the other hand, if the discharge is on throughout the sample preparation, the H atoms should be uniformly distributed in the sample as shown in figure 4.3A (left). Figure 4.3A (right) illustrates the situation for which the lower part of the sample is prepared without discharge, and the upper part of the sample is accumulated when the discharge was running. Thus in sample A2, only in the top half of the sample are the H atoms present, and in the bottom half, initially H atoms are absent. Figure 4.4 shows the ESR spectra from the first sample (A1) at the beginning of experiments, after 4 hours and after 8 hours. The ESR spectra from other two samples (A2, A3) are very similar. The two main signals correspond to the atomic hydrogen low field and high field lines separated by 508.7G. Each main line is accompanied by two satellite lines, which result from the forbidden transitions involving an electron spin flip of an H atom and a simultaneous spin flip of a proton on a neighboring ortho- H_2 molecule. [89] The splitting observed between the left main line and satellite lines is $4.6 \pm 0.1G$, while that between the right main line and the satellite lines is $5.3 \pm 0.1G$.

The three spectra of figure 4.4 for sample A1 show a significant decrease of intensity over an eight hour period. The intensities of both the high field (HF) and low field (LF) ESR lines of hydrogen are reduced by a factor of 4 as compared to the signal for the initially prepared samples. This decline results from the process of recombination of H atoms. The reaction



allows the H atoms to move through the sample until they encounter other hydrogen atoms at which point recombination can occur, according to the reaction



The barely visible satellite lines in the last measured ESR spectrum indicate ortho-para conversion of H₂ molecules surrounding H atoms during the course of the experiment.

The dependence of the average concentration of H atoms in each of the three samples on time is illustrated in figure 4.5a. The initial average concentration of H atoms in each sample is in the range $(2-4) \times 10^{16} \text{cm}^{-3}$. During decay, the concentration of H atoms decreased to approximately 1/4 of the initial value. This clearly shows the result of H atom recombination in the collection of nanoclusters. Furthermore, as discussed below, since the cluster concentration is much greater ($n_{cl}=5 \times 10^{16} \text{cm}^{-3}$, see Discussion section) than the stabilized H atom concentration, percolation through the collection of nanoclusters must take place to allow a hydrogen atom to find a partner. The equation

$$\frac{dn_H}{dt} = -2k_H(T)n_H^2 \quad (4.12)$$

describes the decrease of the local concentration of H atoms (n_H) with time when the temperature of the sample is kept constant. The experimental dependence of the reciprocal concentration ($1/n_H$) on time should thus be linear, with slope equal to $2k_H(T)$. Figure 4.5b shows the dependence of $1/n_{ave}$ on time for each of these samples. From a previous ESR and X-ray study,[17, 4, 87] we know that in impurity-helium condensates formed with H₂ molecules and Ne atoms, the local concentration of H atoms inside nanoclusters is roughly two orders magnitude larger than the measured average concentration. So based on this fact and a linear fitting to the slope of each line, we can calculate the recombination rate of H atoms at T=1.35 K, which is shown

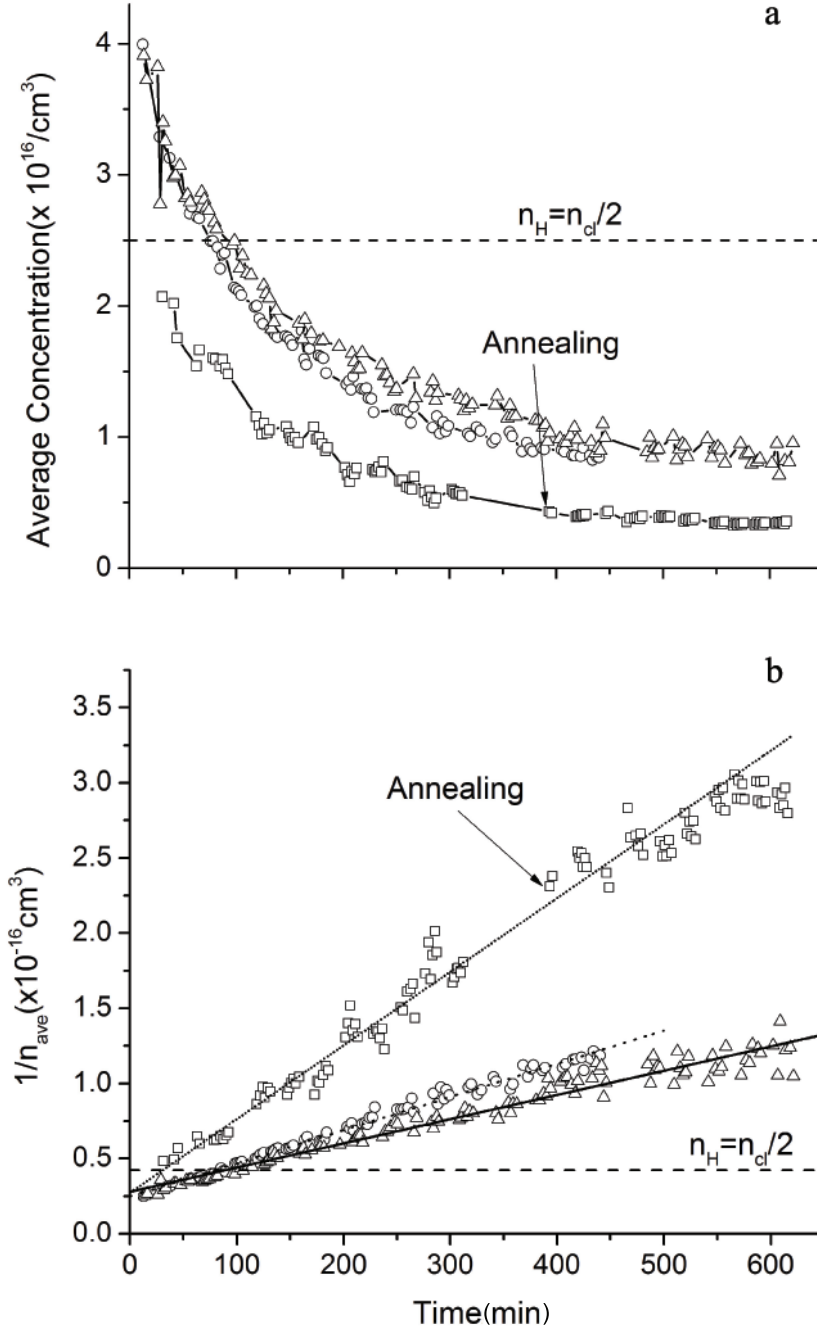


Figure 4.5: The dependence of the average concentration(a) of H atoms and its reciprocal $1/n_{ave}$ (b) on time for sample A1 (open circles), A2 (open triangles) and A3 (open squares). Only sample A3 was annealed at $t=400$ min. The dashed flat line shows the expected plateau level for disconnected clusters. The short dotted, solid lines and long dotted lines in figure (b) are the linear fitting lines for sample A1, A2 and A3, respectively.

Table 4.2: The recombination rate of H atoms for the three different H-H₂-Ne-He samples.

Sample	Calculated k_H at 1.35K, $\text{cm}^3 \cdot \text{s}^{-1}$
A1	1.83×10^{-23}
A2	1.50×10^{-23}
A3	4.08×10^{-23}

in Table 4.2. The estimated recombination rates are in good agreement with those obtained by the Nagoya group, $k_H(1.9-4.2 \text{ K})=(4.4-5.9)\times 10^{-23} \text{ cm}^3\cdot\text{s}^{-1}$ for bulk solid hydrogen samples irradiated by γ -rays.[101]

The actual rate of spatial diffusion of H atoms in the H_2 crystal is at least three orders of magnitude greater than that estimated from the recombination rate of H atoms.[102] Therefore, it should be possible to observe such rapid spatial diffusion of H atoms from the region in the sample with high concentration of H atoms to the region where H atoms are absent in a specially designed sample. The sample A2 was divided in half with the bottom half containing no H atoms due to the accumulation of this part of sample without discharge, and the top half containing H atoms as a result of preparing with the discharge. If the entire sample created is percolated due to the rapidly repeating chemical tunneling reaction (1), we should expect that the H atoms should also be able to move into the lower half. Since in our cavity the space in the bottom half of the beaker has a 2.2 times larger ESR signal sensitivity(see figure 2.4a and b), after a period of time the ESR signal from atoms in the lower half should grow and the overall decay of H atoms in the whole sample should be seen as a slower process compared to that in sample A1. From figure 4.5a, we see that from the start of observation, samples A1 and A2 have almost the same rate of decrease from the initial average concentration, but after about 200 mins, data for A2 starts to deviate from that of A1 and show a somewhat smaller recombination rate in figure 4.5b. This could be the direct evidence that the H atoms migrate from cluster to cluster and try to diffuse to the bottom half of the sample.

Sample A3, initially had a smaller concentration compared to that of samples A1 and A2. Also the recombination rate for this sample was 2-2.5 times larger than that for the A1 and A2 samples. We performed annealing of sample A3 after 400 mins of observation. During the annealing, the sample temperature was gradually increased from 1.35K to 2.6K. After that the sample was kept out of liquid helium for about 30

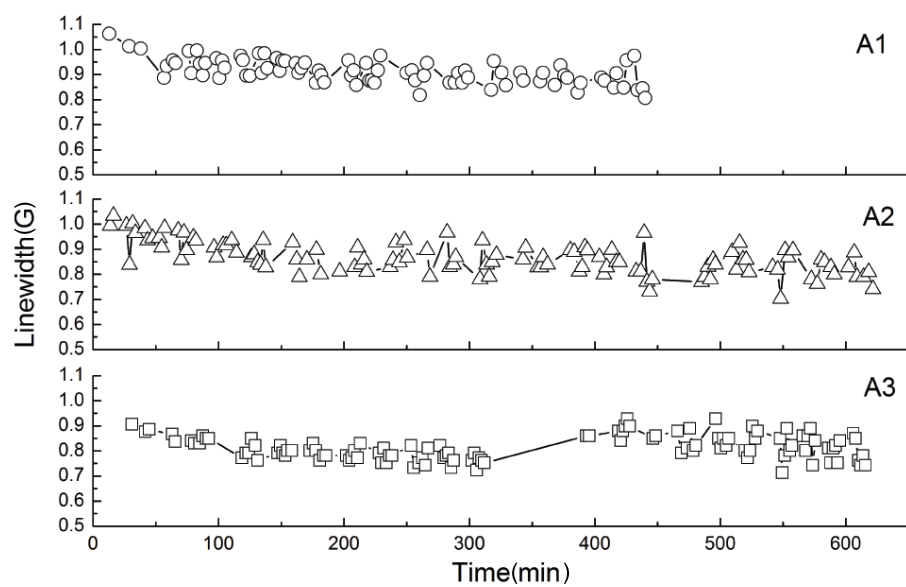


Figure 4.6: Dependence of ESR signal linewidths of H atoms for sample A1 (open circles), A2 (open triangles), and A3 (open squares) on time.

Table 4.3: Hyperfine structure constants, A, and g-factors of H atoms in H-H₂-Ne-He samples, in the gas phase, in solid H₂ and in Ne matrices.

Sample	A, MHz	$\Delta A/A_{free}$, %	g-factor
A1	1416.82(6)	-0.25	2.00242(6)
A2	1416.84(8)	-0.25	2.00242(5)
A3	1416.95(3)	-0.24	2.00242(2)
Gas phase[103, 104]	1420.40573(5)	0	2.002256(24)
H ₂ [105]	1417.13(45)	-0.23	2.00243(8)
Ne(subst.)[106]	1426.51(3)	0.43	2.00206(6)

mins at $T=2.6$ K and then cooled down with liquid helium back to 1.35 K. The behavior of the average concentration before and after annealing is more or less the same as for the unannealed samples without showing any additional increase or decrease of the quantity of H atoms. However, it is clearly seen that in figure 4.5b the experimental value starts to deviate from the fitted line at about 500 mins and tends to be more stable. The recombination rate of H atoms therefore seems to be reduced significantly in the last 100 mins of observation, as evidenced by the change in slope.

During the course of observation of the ESR signals of H atoms, their linewidths decreased. Figure 4.6 shows the dependence of the ESR signal linewidths of H atoms on time for the three samples. The initial linewidths of the H atoms are in the range 0.91G-1.06G, which are in good agreement with the previous result for the case of H atoms in an initially normal H_2 matrix.[107] During the observation time, the linewidth initially decreases almost linearly, indicating catalyzed ortho-para conversion of H_2 molecules. Assuming a linear fitting, we can calculate the rates of decrease for the linewidths, which are 2×10^{-4} G/min for the samples A1 and A2 and 4×10^{-4} G/min for A3. For sample A3, the annealing process led to the sudden increase ($\sim 15\%$) of the linewidth which could be a result of an increase of the local concentration of H atoms. After annealing, the linewidth again starts to decrease with almost the same rate.

The low and high field spectra of H atoms in H_2 -Ne-He samples were each fitted with a Lorentzian line. The results of the analysis are shown in Table 4.3, where we list the values of the g-factors and the hyperfine structure constants, A, obtained for H atoms from the experimental data for H- H_2 -Ne-He samples. The data for H atoms in the gas phase, in solid H_2 and in Ne matrices are also listed in Table 4.3 for comparison. The spectroscopic characteristics of H atoms in the H- H_2 -Ne-He samples are very similar to those obtained for H atoms in an H_2 matrix.[105] This observation is consistent with the shell model of the nanoclusters which form the impurity-helium condensates.[27] The H atoms are trapped in layers of solid H_2 which covered the surfaces of Ne cores of the

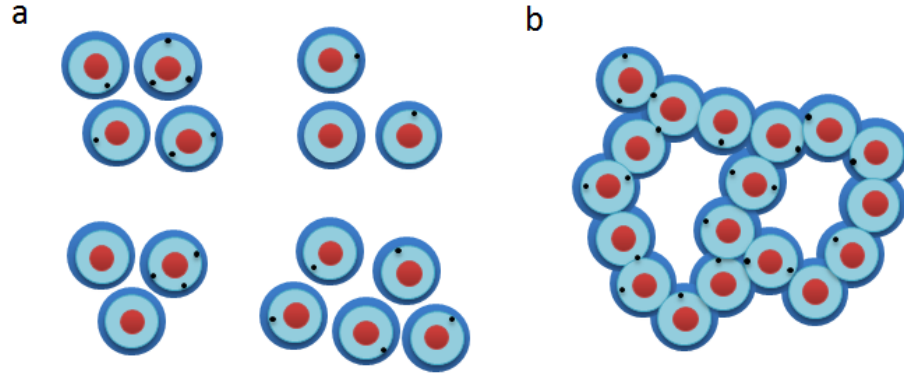


Figure 4.7: Two possible cases for collection of nanoclusters immersed in bulk superfluid helium. a) Collection of separated nanoclusters; b) Percolated aggregates of nanoclusters. The light blue color is the lighter impurity layers (H_2 or D_2) and the red color is the heavier impurity cores (Ne or Kr); dark blue is the solid helium layer covered outside the nanoclusters; black dots are free atoms (H or D) embedded on the surface of the nanoclusters.

clusters (see figure 4.7). The influence of the Ne atoms in the core on the spectroscopic characteristics of H atoms is minimal due to the formation of thick layers of H₂ molecules as a consequence of the large ratio H₂/Ne=4 in the condensed gas mixture.

4.3.2 Studies of condensates containing alternate layers of D-D₂-He and H₂-RG-He nanoclusters

For observation of possible migration of D atoms from one type of nanocluster to the H₂ molecule layers in another type of nanocluster, we also studied samples in which layers of D-D₂-He nanoclusters were separated by layers of H₂-Ne-He (or H₂-Kr-He) nanoclusters. Each layer of the sample was prepared during 2 minutes of condensation of the appropriate gas mixture and collected in the cylindrical part of the beaker (see figure 4.3B). In this set of experiments, the D₂-He mixtures were passed through the discharge zone in order to create D atoms while the H₂-Ne-He or H₂-Kr-He gas mixtures were injected into the HeII without action of the discharge so as to store H₂ molecules in the sample. In this approach we might expect that at the beginning of the experiment in the mixed sample, only an ESR signal from D atoms should be present. In the case of percolation between nanoclusters from different layers we can expect an observation of the rather fast chemical reaction



leading to an increase of the signal from the H atoms in the sample and a decrease of the signal from the D atoms. However, for all layered samples, we observed strong ESR signals for D atoms together with a weak signal for H atoms even at the onset of observations. The presence of H atoms in the samples was due to the small impurity(0.4%) of HD molecules in the Matheson D₂ gas, which we used in our experiments. That is why sample B1, which nominally contains *only* D-D₂-He nanoclusters, was prepared to

Table 4.4: Concentration and rate constants of sample series B.

Sample	Initial n_{ave} , cm^{-3}		Rate constants, cm^3s^{-1} .	
	D atoms	H atoms	k_D	k_{D-HD}
B1	7.92×10^{17}	2.60×10^{15}	8.05×10^{-26}	2.57×10^{-27}
B2	1.06×10^{18}	2.62×10^{15}	5.71×10^{-26}	3.28×10^{-27}
B3	1.45×10^{17}	1.17×10^{15}	5.74×10^{-26}	9.68×10^{-27}
B4	8.90×10^{17}	3.07×10^{15}	4.67×10^{-26}	2.45×10^{-27}

compare the behavior of the changing H and D concentration in this sample with that in the layered samples.

Figure 4.8 illustrates the dependence of the average concentrations of both D and H atoms on time for each of the samples studied. The four samples show very similar rates of decay of D atoms and the increase of H atoms. This gives evidence that the following reactions occurred in the samples:



Previous experimental studies[33] have shown that the rate constant for reaction 4.14 is about one order of magnitude larger than for reaction 4.15. Therefore, the decay of D atom concentrations is determined mostly by reaction 4.14, while the relatively small increase of H atom concentration and a corresponding small decrease of D atom concentrations is provided by reaction 4.15. Since this behavior was observed even in sample B1 prepared purely from the nominal D₂-He gas mixture, it was clear that HD molecules were present in this sample as a result of the presence of a small impurity of HD molecules in the D₂ gas used in the experiments. Due to the similar behavior of the kinetics of D and H atoms in layered samples and in the D-D₂-He sample, we can conclude that we do not obtain direct evidence for fast reaction 4.13 in the layered samples B2, B3 and B4 from these experiments. The only processes observed in those samples are occurring in the D-D₂-He layers. Otherwise, we should have observed an enhancement of H atom concentrations in these layered samples as compared with those in the D-D₂-He samples. Table 4.4 shows the initial concentrations of both D and H atoms as well as the rate constants for reaction 4.14 and 4.15 in each sample studied. The estimated k_D and k_{D-HD} are in agreement with the results of previous work.[33]

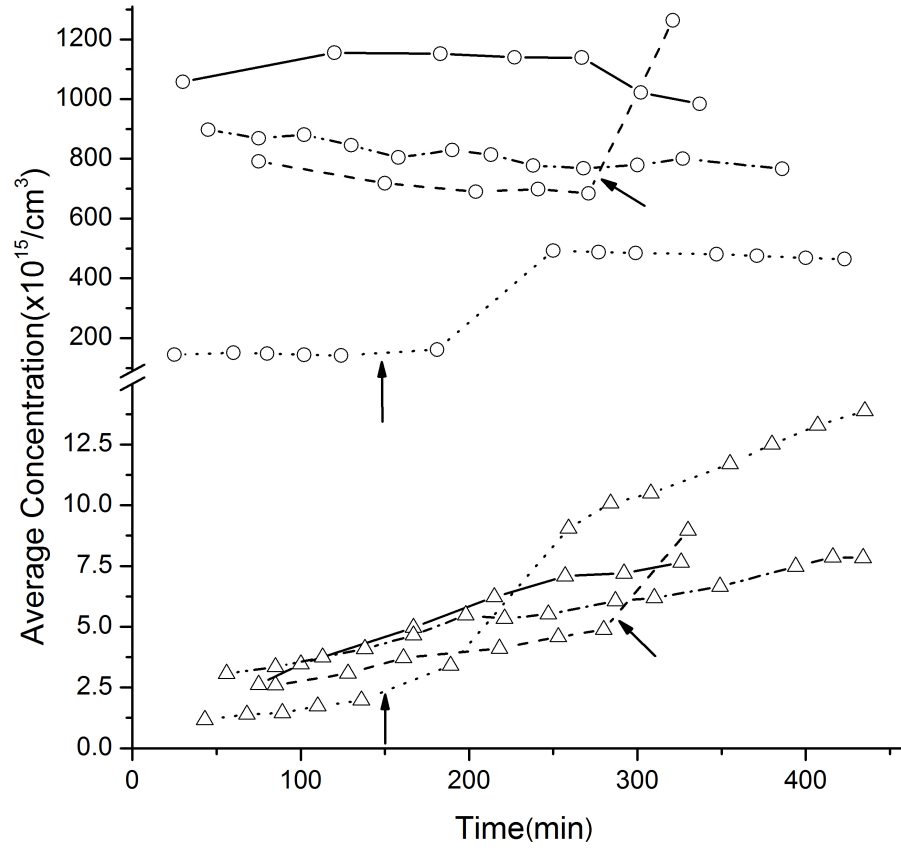


Figure 4.8: The time dependence of average concentration of D atoms (open circles) and H atoms (open triangles) in sample B1(dashed line), B2(solid line), B3(dotted line) and B4(dash dotted line). The arrows show times for starting annealing of the samples: B1(288min) and B3(150min).

Table 4.5: Hyperfine structure constants, A , and g -factors for ESR spectra of H and D atoms in layered samples, in D-D₂-He samples, in the gas phase and in solid H₂ and D₂ matrices.

Atoms, sample	A , MHz	$\Delta A/A_{free}$, %	g -factor
H,B1	1416.42(2)	-0.28	2.00225(3)
H,B2	1416.71(4)	-0.26	2.00226(9)
H,B3	1416.53(4)	-0.27	2.00215(6)
H,B4	1416.56(7)	-0.27	2.00218(4)
H, Gas phase[103, 104]	1420.40573(5)	0	2.002256(24)
H,H ₂ [105]	1417.13(45)	-0.23	2.00243(8)
H,Kr(subst.)[106]	1411.799	-0.61	2.00179(8)
H,Kr(subst.)[109]	1409	-0.80	2.0013
D,B1	217.663(8)	-0.27	2.00219(6)
D,B2	217.656(4)	-0.27	2.00220(3)
D,B3	217.659(6)	-0.27	2.00220(4)
D,B4	217.641(6)	-0.28	2.00219(9)
D, Gas phase[110, 111]	218.25601	0	2.002256
D,D ₂ [112]	217.71(18)	-0.25	2.00231(8)
D,D ₂ [113]	218.86(15)	-0.28	2.00220(16)
D,Kr(subst.)[114]	216.30	-0.896	2.0015
D,Ne(subst.)[114]	219.0(1)	0.345	2.0020(1)

Table 4.5 is a summary of the hyperfine structure constants, A , and g -factors for ESR spectra of H and D atoms in layered and D-D₂-He samples. The values of A and g in the gas phase as well as in solid H₂, D₂, Ne and Kr matrices are also given for comparison. In all samples studied in the experiments, the g factors and hyperfine constants of D atoms are closest to the values for a D₂ matrix, which is naturally reasonable due to the mixture we used. For H atoms, the g -factors are slightly smaller than those in an H₂ matrix. We think that H atoms should exist in the environment of D₂ molecules because of the low average concentration of H atoms. However, we were not able to find any reference containing hyperfine constant and g -factor values of H atoms in a D₂ matrix to compare with. Figure 4.8 shows the time dependence of the linewidths of D atoms and H atoms in the samples. The main fact in figure 4.8 is that the linewidths of H atom signals (1.7-2.6 G) are significantly larger than that for D atoms (1.2-1.4 G). Also, the linewidths of H atoms in mixed samples are higher than those for H atoms in an H₂ matrix (1-0.8 G). Miyazaki et. al.[108] have shown that H and D atoms in solid HD and D₂ are trapped in interstitial octahedral sites, while H atoms in solid H₂ are trapped in the substitutional sites. Therefore, H atoms in solid H₂ are trapped in larger sites than D atoms in solid D₂, corresponding to the longer distance between a trapped H atom and a nearest-neighbor molecules in solid H₂. Thus, the superhyperfine interaction in solid H₂ is weaker than that in solid D₂, resulting in a narrower spectrum of H atoms in H₂. However, this could not explain why the linewidths of H atoms are larger than those for D atoms in a D₂ matrix. The explanation will be given later.

More promising results were observed for annealed samples. The annealing was employed for samples B1 and B3 (see figure 4.8 and 4.9). After annealing the samples to 2.6 K and cooling back to 1.35 K, the average concentration of both D atoms and H atoms increased by a few times due to the compressing of the samples and collapsing pores. The elimination of the pores reduces the volume of the sample. If most of the H atoms survive during annealing, their average concentrations should increase. Table

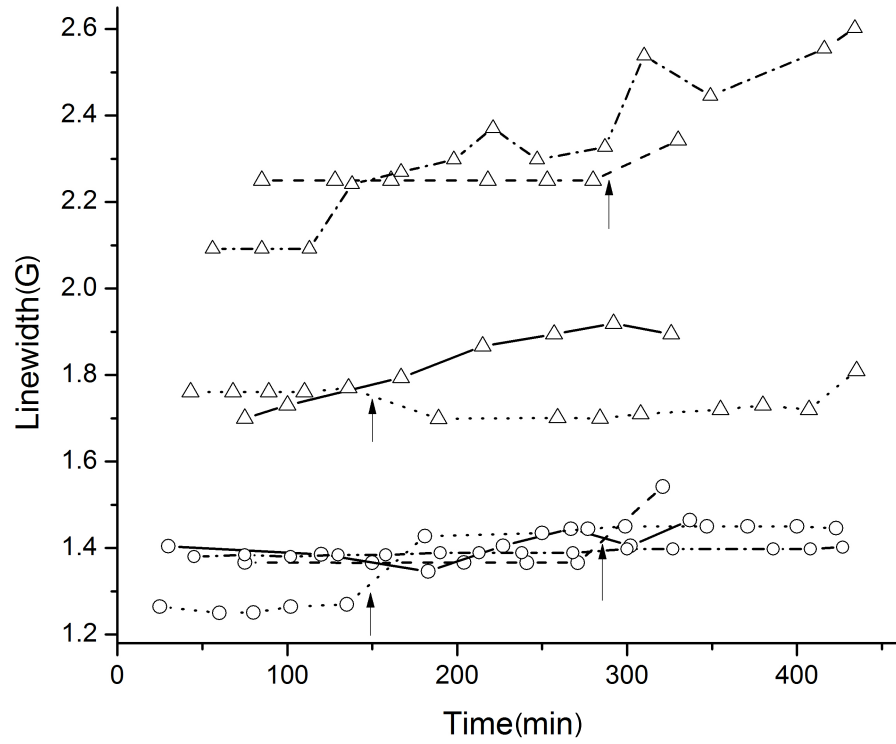


Figure 4.9: The time dependence of linewidth of D atoms (open circles) and H atoms (open triangles) in sample B1(dashed line), B2(solid line), B3(dotted line) and B4(dash dotted line). The arrows show times for starting annealing of the samples: B1(288min) and B3(150min).

Table 4.6: Average Concentrations of H and D atoms before and after annealing of the samples B1 and B3.

Sample	B1		B3	
	D atoms	H atoms	D atoms	H atoms
Before annealing, n_0	6.84×10^{17}	4.88×10^{15}	1.42×10^{17}	1.97×10^{15}
After annealing, n_{ann}	1.26×10^{18}	8.96×10^{15}	4.93×10^{17}	9.04×10^{15}
Ratio, n_{ann}/n_0	1.85	1.84	3.47	4.59

4.6 shows the average concentrations of H and D atoms and their ratio just before and after the annealing process. We can see from the Table 4.6 that for sample B1 the concentrations of both D and H atoms were increased by the same factor, about 1.84 times after annealing while for sample B3 the H atom concentration increased more than that for D atoms. This result indicates that in the sample B1, only the effect of increasing the average concentrations of H and D atoms due to collapsing pores were observed. In sample B3, in addition to the simultaneous increase of both concentrations of H and D atoms due to the collapsing pores in the sample (~ 3.47 times), an extra increase in concentration of H atoms was observed, which could not be explained by reaction 4.15 which has a rather small rate constant and during annealing time (~ 40 min) could not make substantial changes of H and D concentration. Therefore, the most plausible explanation is that the annealing process also helped to create paths available for D atoms to meet H_2 molecules. In this case, due to the fast reaction 4.13, more H atoms were produced. This annealing process has convinced us of the possibility of creating percolation in samples composed of nanoclusters containing mixtures of hydrogen isotopes. More evidence for percolation was also found in the linewidth study during the annealing process. For sample B1, the annealing was performed before the last measurement, which resulted in the line broadening of both H and D atom signals. This can be explained by the increase of the local concentration of both H and D atoms and thus by the enhanced electron spin dipole-dipole interaction. However, for sample B3, the annealing did not have the same effect on H and D atoms. Instead, the linewidth of H atoms shows a slight decrease while that of D atoms still increased. This might support the idea of percolation in which the new H atoms produced as a result of annealing are not in the same environment as for H atoms already in place. [42, 102] The fast spatial diffusion allows H atoms to find a partner in the connected layers of solid H_2 matrix and recombine.

4.4 Discussion

Impurity-helium condensates are porous gel-like materials created by injecting a mixed beam of helium gas and some impurity atoms and molecules into superfluid helium.[17, 4, 87] The collection of nanoclusters formed by impurities creates a porous structure with nanoscale pores inside HeII.[4, 3, 30] Isolation of highly reactive atoms in nanoclusters surrounded by HeII leads to the stabilization of high concentrations of these atoms.[13, 27] In the case of injection of two different impurities into HeII, the nanoclusters have shell structures in which heavier impurities form cores surrounded by lighter impurities plus solid helium. In experiments involving hydrogen-krypton-helium jets, high average and local concentration of H atoms were achieved.[27] These H atoms are stabilized in the H₂ films which cover the Kr cores of nanoclusters. The existence of a layer of H₂ molecules covering a Kr cluster surface provides an environment which allows the study of the diffusion and tunneling of H atoms. In this environment, samples containing high concentrations of H atoms may exhibit interacting macroscopic Bose-Einstein correlations at lower temperatures if H atoms can travel rather freely between H₂ layers of different nanoclusters. This requires that the thermal de Broglie wavelength be comparable or greater than the average spacing between H atoms. Hence investigations of the possibility of transport of atoms of the light hydrogen isotopes between nanoclusters at lower temperatures in impurity-helium condensates is of great interest. Experiments by John Reppy and coworkers have demonstrated Bose-Einstein correlations for very dilute films of liquid helium trapped in porous vycor glass. [115, 116]

In hydrogen-krypton samples prepared from a [H₂]:[Kr]:[He]=1:1:200 gas mixture, the average concentration of H atoms $n_H=1.4\times 10^{18}\text{cm}^{-3}$ was obtained.[27] According to x-ray investigations[28] the average density of impurities in these samples is of order 10^{20}cm^{-3} and the number of impurities in a cluster with diameter 5 nm is equal to

~ 2000 . This information allows one to calculate the concentration of clusters in the sample, $n_{cl}=5.0 \times 10^{16} \text{cm}^{-3}$ and make an estimate of the number of H atoms in each of the clusters, $n_H=28$ per cluster. Therefore, during studies of the recombination of H atoms in samples with high concentrations of atoms, it is difficult to distinguish processes occurring inside the clusters from those occurring between clusters. The lifetime for decay of H atoms in this sample was ~ 160 minutes.[27] Achieving a regime when only a single H atom is stabilized in a cluster [117, 118] allows one to monitor the process of recombination of H atoms from different clusters. For the above mentioned hydrogen-krypton samples, this requires continuation of experiments after observation times larger than 10 hours. Therefore, in this work we used a different approach for studying percolation between nanoclusters. Instead, we initially created hydrogen-neon samples in which the number of stabilized H atoms are close to or even less than the number of clusters in the samples. From the spectroscopic characteristics of H atoms presented in Table II, we can conclude that these atoms are mostly stabilized in the H_2 layers formed on the surfaces of Ne nanoclusters. We have not observed signals which may be assigned to the H atoms stabilized in the Ne matrix. In this situation, even from the beginning of the investigation, we should observe recombinational decay of H atoms only if there are connections between nanoclusters (see figure 4.7b). For the case of collections of non percolating clusters (see figure 4.7a), we should observe a plateau for $n_H=n_{cl}/2= 2.5 \times 10^{16} \text{cm}^{-3}$ on the dependence of H atom concentration on time. This value is calculated from considering the fact that in the clusters with even numbers of H atoms all atoms should eventually recombine, whereas in clusters with odd numbers of H atoms only one atom will remain per cluster. Initially on average half of the clusters should contain an even number of H atoms and other half should contain an odd number of H atoms.

Results presented in figure 4.5 show that recombination of H atoms continues even when the number of H atoms in the samples is much less than one half of number

of clusters. These results provide strong evidence for percolation in the collection of hydrogen-neon nanoclusters. The success of this experiment resulted from the rapid process of chemical diffusion of H atoms due to the exchange tunnelling reaction between H atoms and H₂ molecules. This allowed the H atoms to tunnel through the H₂ films covering the cluster core and pass into the H₂ layer covering an adjacent cluster core. The spatial diffusion coefficient for H atoms in an H₂ matrix, $D_{sp} \geq 10^{-13} \text{ cm}^2/\text{s}$, is four orders of magnitude larger than that obtained from the H atom recombination process $D_{rec} = 10^{-17} \text{ cm}^2/\text{s}$. [42, 102] The fast spatial diffusion allows H atoms to find a partner in the *connected layers* of solid H₂ matrix and recombine.

Completely different behavior was observed for layered samples. In the layers formed by a D-D₂-He gas mixture the nanoclusters of D₂ contain stabilized D atoms mainly on their surfaces. [26] In layers formed by H₂-Ne-He or H₂-Kr-He gas mixtures, the H₂ layers formed on the surfaces of Ne or Kr nanoclusters. In either case, if the nanoclusters from different layers are connected, we would expect to observe a rather fast (\sim minutes) reaction of D atoms with the H₂ molecules. [95, 119] From the comparison of the processes of D atom recombination and production of H atoms in the pure D-D₂-He sample and in the layered samples (see figure 4.7), we did not find any direct evidence for the percolation between nanoclusters. The dynamics of changes of D and H atom concentrations in those samples were similar. Only annealing of the layered samples gave evidence for enhancement of H atom concentrations and correspondingly for percolation in these samples. The absence of obvious effects of enhancing H atom concentrations in layered samples does not rule out the possibility of percolation in those samples. The reaction of D atoms with H₂ molecule occurs only when these species are in neighboring sites in a solid matrix. This means that D atoms should move to a position adjacent to a hydrogen molecule. The process of tunneling of D atoms through a D₂ matrix is four orders of magnitude slower as compared with the rate of tunneling H atoms in an H₂ matrix. [95] Because of this very slow process for migration of D atoms, we have not

observed the enhancement of the concentration of H atoms in layered samples. Only sample annealing involving the collapsing of the pores can produce additional points of contact between clusters where D atoms and H₂ molecules could interact occasionally, resulting in the tunnelling reaction, which leads to an increase of H atom concentration.

The rapid spatial migration of H atoms in an H₂ matrix helped us to observe changes in the distribution of H atoms with time in the presence of a gradient in H atom concentration in sample A2. In the lower part of the sample, which occupied the most sensitive region of the cavity, initially the hydrogen-neon sample did not contain H atoms. The volume above was filled with a hydrogen-neon sample which did contain H atoms. Luckily the concentration of H atoms in this sample was similar to that of another sample in which the H atoms were distributed throughout the entire sample (A1). If both samples are allowed to percolate and the rate of recombination of H atoms is comparable, we should observe decreasing decay in the sample with the H atom gradient due to the process of migration of H atoms from top of the sample to the bottom where the sensitivity of the signal is higher. This is exactly what we observed from a comparison of the decay of H atom concentrations in these samples. In the first 200 minutes of the experiment the points for samples A1 and A2 almost coincided (see figure 4.5). However, after this period, the effective decay of H atoms in the sample with a gradient of H atoms became slower. This observation clearly supports the existence of percolation between nanoclusters and effective transport of H atoms from the region containing nanoclusters with stabilized H atoms to the region with nanoclusters containing only layers of H₂ molecules.

Differences in initial concentrations of H and D atoms in different samples (see figure 4.5 and 4.8) could perhaps be explained by poor reproducibility of conditions in the discharge zone during the process of sample preparation. The observed ranges in the rates of H atom recombination in hydrogen-neon samples (see Table 4.2) $(1.5-4.8) \times 10^{-23} \text{cm}^3/\text{s}$ and D atom recombination in the layered samples (4.67-

$8.05 \times 10^{-26} \text{cm}^3/\text{s}$ (see Table 4.4) might be related to different ortho-para ratios of H_2 and D_2 molecules, respectively.[120] The linewidths of H atoms in as-prepared H_2 -Ne samples are of order 1G and have a tendency to decrease as time progress. The concentrations of H atoms in these samples are rather small, so therefore electron spin dipole-dipole interactions do not contribute significantly to the broadening of the ESR lines. The broadening results from the interactions of electron spins of H atoms with nuclear spins in neighboring ortho H_2 molecules. The decrease of the linewidths of H atoms with time might be explained by the slow ortho-para conversion of H_2 molecules at distances larger than the first coordination sphere surrounding each of H atoms. The nearest-neighboring ortho- H_2 molecules are converted into para- H_2 molecules very rapidly ($\tau = 10\text{s}$). [121, 122] The rate of decrease of the linewidths [$(2-4) \times 10^{-4} \text{G}/\text{min}$] in our experiments are very similar to those observed in earlier experiments in which stabilized nitrogen atoms were added to the H_2 matrix.[123]

In the layered samples and in the D- D_2 -He sample, the linewidth of H atoms ($\sim 2\text{G}$) is larger than that for D atoms ($\sim 1.4\text{G}$). In both types of samples, most of the H and D atoms are stabilized in the D_2 matrix. In the D_2 molecular matrix the para state ($J=1$) of D_2 molecules is 85K more energetic than the ortho states of D_2 molecules ($J=0,2$). The presence of H and D atoms in the D_2 matrix catalyze the conversion from the para to the ortho state of D_2 molecules. The $J=0$ ortho state must be accompanied by either the $I=0$ or $I=2$ spin states. The $I=2$ state is $2I+1=5$ (fivefold degenerate), whereas the $I=0$ state is nondegenerate. The energy splitting between the $I=0$ and $I=2$ states is negligible at liquid helium temperatures meaning that each of the five $I=2$ states and the singlet $I=0$ state are equally populated. As a result, a D atom on a substitutional site in an fcc D_2 matrix has 12 nearest neighbor D_2 molecules in the first coordination shell, 10 of which correspond to spin $I=2$. The increase in linewidth of D atom in D_2 as compared to the linewidth of H in H_2 is, therefore, due to the interaction of the electron spins of the D atoms with the nuclear spins of ortho- D_2 molecules having spins $I=2$.

The even larger broadening of H atom ESR lines in a D₂ matrix can be explained by the larger zero-point energy of H atoms in comparison with stabilized D atom in a D₂ matrix. The electron spin interacts with the same number of ortho-D₂ molecules, but the larger amplitude of zero point motion leads to an increase of the dipole-dipole interaction between the electron spin of H atoms and the nuclear spins of the ortho-D₂ molecules.

Based on the results of this work, we can conclude that it is possible to create hydrogen-RG-helium condensates which contain high concentrations of H atoms residing in the layers of H₂ molecules. The layer of H₂ molecules are percolated throughout the whole sample providing a unique system for studying quantum overlap effects of H atoms in the solid phase. For a H-H₂-Kr sample with a local concentration of H atoms $n_H=6\times 10^{20}\text{cm}^{-3}$ the mean distance between atoms in an H₂ layer is $d_m=10^8\text{\AA}/\sqrt[3]{n_H}=25\text{\AA}$. The thermal de Broglie wavelength $\lambda(T) = \sqrt{2\pi\hbar^2/mkT}$ for free H atoms will be comparable to the mean distance between atoms at T=484 mK. The effective mass of H atoms in an H₂ matrix must be larger than that for free H atoms. But even if the effective mass of H atoms in H₂ is 10 times larger than that of free atoms, the temperature where the mean distance between H atoms is equal to the thermal de Broglie wavelength will be equal to ~ 153 mK. This range of temperatures is easily accessible using a dilution refrigerator.

The process of formation and investigation of impurity-helium condensates is a challenging task. However, we are working on the design of the cell for creating and investigating impurity-helium condensates at temperatures below 1 K. The experimental setup will be similar to that used in experiments for studying H atoms in H₂ matrices[83, 84, 85, 86] and spin-polarized atomic hydrogen gas[124] at ultralow temperatures. The modifications of the sample cell should allow filling it with superfluid helium and injecting the impurities into the superfluid helium at temperatures 0.5-0.7 K. The cell is thermally anchored to the dilution refrigerator mixing chamber. The

sensitivity of the 130 GHz ESR spectrometer,[83] which we plan to use in these experiments, is high enough for studying small quantities of the samples obtained during 10-20 minutes with a flux of 10^{16} impurity atoms and molecules per second. This regime has been successfully realized in our recent experiments by using a dilution refrigerator.[125] After finishing preparation, the sample can be cooled to 100 mK or lower.

4.5 Conclusions

The impurity-helium solids created by injection of hydrogen and deuterium atoms and molecules together with rare gas atoms (Ne or Kr) into superfluid helium have been studied by the ESR method. Processes of atomic recombination and exchange chemical tunnelling reactions between atoms and molecules of hydrogen isotopes have been investigated at temperatures 1.35-2.6K. Observation of H atom recombination have been performed in a situation for which the number of H atoms in the sample is less than the number of nanoclusters. It was shown for this case that H atoms could travel freely between clusters. This fact provides evidence for percolation between nanoclusters.

Measurements of ground state spectroscopic parameters of hydrogen atoms provide clear evidence that nanoclusters have shell structures with the cores of hydrogen-neon nanoclusters formed by the heavier neon atoms and the outer layer formed by lighter hydrogen molecules in which most of H atoms are stabilized. These outer layers of the nanoclusters are connected, which allowed the H atom to travel via rapid spatial diffusion through the porous structure.

We observed a large isotope effect when we designed an experiment for the observation of an exchange tunnelling reaction between D atoms on one cluster with H_2 molecules residing on another nanocluster. We did not observe the effect of an increasing concentration of H atoms expected from the tunneling exchange reactions between D atoms and H_2 molecules. This is a result of the very slow spatial diffusion of D atoms in a D_2 matrix.

Observation of percolation in aggregates of hydrogen-neon nanoclusters immersed in HeII is an important step in the search for quantum correlation phenomena of H atoms in the solid phase at low temperatures. The combination of high concentrations of H atoms in H₂ layers on surfaces of Kr nanoclusters and the percolation of H atoms through the sample makes this system very attractive for the study of quantum overlap phenomena. The temperatures for the onset of possible quantum phenomena require a mean distance between H atoms in the system to be comparable to the thermal de Broglie wavelength of the H atoms. This temperature region should be accessible using a dilution refrigerator.

REFERENCES

- [1] E.B. Gordon, L.P. Mezhov-Deglin, and O.F. Pugachev. *JETP Lett.*, 19:63, 1974.
- [2] E.B. Gordon, V.V. Khmelenko, E.A. Popov, A.A. Pelmenev, and O.F. Pugachev. *Chem. Phys. Lett.*, 155:301, 1989.
- [3] S.I. Kiselev, V.V. Khmelenko, and D.M. Lee. *J. Low Temp. Phys.*, 121:671, 2000.
- [4] S.I. Kiselev, V.V. Khmelenko, D.M. Lee, V. Kiryukhin, R.E. Boltnev, E.B. Gordon, and B. Keimer. *Phys. Rev. B*, 65:024517, 2002.
- [5] V.V. Nesvizhevsky. *Phys. At. Nucl.*, 65:400, 2002.
- [6] G. Frossati. *J. Low Temp. Phys.*, 111:521, 1998.
- [7] R.E. Boltnev, G. Frossati, E.B. Gordon, I.N. Krushinskaya, E.A. Popov, and A. Usenko. *J. Low Temp. Phys.*, 127:245, 2002.
- [8] B. Palaszewski, L.S. Ianovski, and P. Carrick. *J. of Prop. and Power*, 14:641, 1998.
- [9] E.P. Bernard, R.E. Boltnev, V.V. Khmelenko, V. Kiryukhin, S.I. Kiselev, and D.M. Lee. *Phys. Rev. B*, 69:104201, 2004.
- [10] E.P. Bernard, R.E. Boltnev, V.V. Khmelenko, and D.M. Lee. *J. Low Temp. Phys.*, 134:169, 2004.
- [11] P. Brusov, J.M. Parpia, P. Brusov, and G. Lawes. *Phys. Rev. B*, 63:140507(R), 2001.
- [12] E.P. Bernard, R.E. Boltnev, V.V. Khmelenko, and D.M. Lee. *J. Low Temp. Phys.*, 134:175, 2004.
- [13] V.V. Khmelenko, H. Kuntuu, and D.M. Lee. *J. Low Temp. Phys.*, 148:1, 2007.
- [14] L.P. Mezhov-Deglin and A.M. Kokotin. *J. Low Temp. Phys.*, 119:385, 2000.
- [15] V.E. Efimov, A.V. Lokhov, L.P. Mezhov-Deglin, C. Dewhurst, V.V. Nesvizhevsky, and G.V. Kolmakov. *JETP Lett.*, 99:32, 2014.
- [16] V.V. Khmelenko, R.E. Boltnev, E.B. Gordon, I.N. Krushinskaya, M.V. Martynenko, A.A. Pelmenev, E.A. Popov, and D.Y. Stolyakov. *Proceedings of Second International Conference on Low Temperature Chemistry, University of Missouri-Kansas City, Kansas City*, page 163, 1996.
- [17] V. Kiryukhin, B. Keimer, R.E. Boltnev, V.V. Khmelenko, and E.B. Gordon. *Phys. Rev. Lett.*, 79:1774, 1997.

- [18] R.E. Boltnev, E.B. Gordon, I.N. Krushinskaya, A.A. Pelmenev, E.A. Popov, O.F. Pugachev, and V.V. Khmelenko. *Fiz. Nizk. Temp.*, 18:819, 1992.
- [19] E.B. Gordon, V.V. Khmelenko, A.A. Pelmenev, E.A. Popov, O.F. Pugachev, and A.F. Shestakov. *Chem. Phys.*, 170:411, 1993.
- [20] R.E. Boltnev, E.B. Gordon, I.N. Krushinskaya, M.V. Marynenko, A.A. Pelmenev, E.A. Popov, V.V. Khmelenko, and A.F. Shestakov. *Fiz. Nizk. Temp.*, 23:753, 1997.
- [21] E.B. Gordon, A.A. Pelmenev, O.F. Pugachev, and V.V. Khmelenko. *Chem. Phys.*, 61:35, 1981.
- [22] R.E. Boltnev, E.B. Gordon, V.V. Khmelenko, I.N. Krushinskaya, M.V. Marynenko, A.A. Pelmenev, E.A. Popov, and A.F. Shestakov. *Chem. Phys.*, 189:367, 1994.
- [23] R.E. Boltnev, I.N. Krushinskaya, A.A. Pelmenev, D. Yu Stolyarov, and V.V. Khmelenko. *Chem. Phys. Lett.*, 305:217, 1999.
- [24] V.V. Khmelenko, D.M. Lee, I.N. Krushinskaya, R.E. Boltnev, I.B. Bykhalo, and A.A. Pelmenev. *Low Temp. Phys.*, 38:688, 2012.
- [25] R.E. Boltnev, A.A. Krushinskaya, I.N. and Pelmenev, E.A. Popov, D. Yu Stolyarov, and V.V. Khmelenko. *Low Temp. Phys.*, 31:547, 2005.
- [26] E.P. Bernard, V.V. Khmelenko, and D.M. Lee. *J. Low Temp. Phys.*, 150:516, 2008.
- [27] R.E. Boltnev, E.P. Bernard, J. Jarvinen, V.V. Khmelenko, and D.M. Lee. *Phys. Rev. B*, 79:180506, 2009.
- [28] V. Kiryukhin, E.B. Bernard, V.V. Khmelenko, R.E. Boltnev, N.V. Krainyukova, and D.M. Lee. *Phys. Rev. Lett.*, 98:195506, 2007.
- [29] N.V. Krainyukova, R.E. Boltnev, E.P. Bernard, V.V. Khmelenko, V. Kiryukhin, and D.M. Lee. *Phys. Rev. Lett.*, 109:245505, 2012.
- [30] S.I. Kiselev, V.V. Khmelenko, and D.M. Lee. *Low Temp. Phys.*, 26:641, 2000.
- [31] E.B. Gordon, A.A. Pelmenev, O.F. Pugachev, and V.V. Khmelenko. *JETP Lett.*, 37:283, 1983.
- [32] S.I. Kiselev, V.V. Khmelenko, and D.M. Lee. *Phys. Rev. Lett.*, 89:17, 2002.
- [33] V.V. Khmelenko, E.P. Bernard, S. Vasiliev, and D.M. Lee. *Russ. Chem. Rev.*, 76:1107, 2007.
- [34] R.S. Alger. *Electron Paramagnetic Resonance: Technique and Applications*. (John Wiley and Sons, New York, 1968) p. 22.
- [35] A.M. Bass. *Formation and Trapping of Free Radicals*, Academic Press New York, London (1960).

- [36] E.B. Gordon, L.P. Mezhov-Deglin, O.F. Pugachev, and V.V. Khmelemko. *Chem. Phys. Lett.*, 54:282, 1978.
- [37] E.B. Gordon, V.V. Khmelemko, A.A. Pelmenev, and O.F. Pugachev. *Physica B & C*, 108:1311, 1981.
- [38] E.B. Gordon, M.V. Martynenko, A.A. Pelmenev, O.F. Pugachev, and V.V. Khmelemko. *Khim. Fiz.*, 13:15, 1994.
- [39] R.E. Boltnev, E.B. Gordon, V.V. Khmelenko, M.V. Martynenko, A.A. Pelmenev, E.A. Popov, and A.F. Shetakov. *J. Chim. Phys.*, 92:362, 1995.
- [40] E.B. Gordon, A.A. Pelmenev, O.F. Pugachev, and V.V. Khmelenko. *J. Low Temp.*, 8:299, 1982.
- [41] E.B. Gordon, A.A. Pelmenev, O.F. Pugachev, and V.V. Khmelenko. *Doklady Physical Chemistry*, 280:145, 1985.
- [42] E.B. Gordon, A.A. Pelmenev, O.F. Pugachev, and V.V. Khmelenko. *Sov. J. Low Temp.*, 11:307, 1985.
- [43] S.I. Kiselev, V.V. Khmelenko, C.Y. Lee, and D.M. Lee. *J. Low Temp. Phys.*, 128:37, 2002.
- [44] S.I. Kiselev, V.V. Khmelenko, and D.M. Lee. *Phys. Rev. Lett.*, 89:175301, 2002.
- [45] S.I. Kiselev, V.V. Khmelenko, E.P. Bernard, and D.M. Lee. *Low Temp. Phys.*, 29:505, 2003.
- [46] S.I. Kiselev, V.V. Khmelenko, E.P. Bernard, C.Y. Lee, and D.M. Lee. *Physica B*, pages 329–333, 2003.
- [47] Bernard E.P., R.E. Boltnev, V.V. Khemelenko, and D.M. Lee. *J. Low Temp. Phys.*, 138:829, 2005.
- [48] S.I. Kiselev, V.V. Khmelenko, D.M. Lee, V. Kiryukhin, R.E. Boltnev, E.B. Gordon, and B. Keimer. *Phys. Rev. B*, 65:024517, 2002.
- [49] S.I. Kiselev, V.V. Khmelenko, D.M. Lee, V. Kiryukhin, R.E. Boltnev, E.B. Gordon, and B. Keimer. *J. Low Temp. Phys.*, 126:335, 2002.
- [50] S.I. Kiselev, V.V. Khmelenko, D.A. Geller, D.M. Lee, and J.R. Beamish. *J. Low Temp. Phys.*, 119:357, 2000.
- [51] S.I. Kiselev, V.V. Khmelenko, D.A. Geller, J.R. Beamish, and D.M. Lee. *Physica B*, 284:105, 2000.
- [52] R.E. Boltnev, E.P. Bernard, J. Jarvinen, I.N. Krushinskaya, V.V. Khmelenko, and D.M. Lee. *J. Low Temp. Phys.*, 158:468, 2010.

- [53] R.E. Boltnev, V.V. Khmelenko, and D.M. Lee. *Low Temp. Phys.*, 36:382, 2010.
- [54] M.A. Heald and R. Beringer. *Phys. Rev.*, 96:645, 1954.
- [55] H. Kopfermann. *Nuclear Moments*. (Academic Press, New York, 1958), Chapter I, Parts I, II, and III, pages 1-161.
- [56] N.F. Ramsey. *Molecular Beams*. (Oxford University Press, London, 1956), pages 68-88, particularly pages 76-80.
- [57] S. Larsson, R.E. Brown, and V.H. Smith. *Phys. Rev.*, 6:1375, 1972.
- [58] H. Lew and G. Wessel. *Phys. Rev.*, 90:1, 1953.
- [59] C.K. Jen, V.A. Bowers, E.L. Cochran, and S.N. Foner. *Phys. Rev.*, 126:1749, 1962.
- [60] G.L. Pollack. *Rev. Mod. Phys.*, 36:748, 1964.
- [61] B. Meyer. *Low Temperature Spectroscopy: Optical Properties of Molecules in Matrices, Mixed Crystals, and Organic Glasses*. (Elsevier, New York, 1970).
- [62] F.J. Adrian. *Phys. Rev.*, 127:837, 1962.
- [63] G.S. Jackel, W.H. Nelson, and W. Gordy. *Phys. Rev.*, 176:453, 1968.
- [64] J.H. Van der Waals and M.S. de Groot. *Mol. Phys.*, 2:333, 1959.
- [65] L.B. Knight, B.A. Bell, D.P. Cobranchi, and Davidson E.R. *J. Chem. Phys.*, 111:3145, 1999.
- [66] S.N. Foner, C.K. Jen, E.L. Cochran, and V.A. Bower. *J. Chem. Phys.*, 28:351, 1958.
- [67] Yu Dmitriev and R.A. Zhitnikov. *Low Temp. Phys*, 24:44, 1998.
- [68] P.H.H Fisher, S.W. Charles, and C.A. McDowell. *J. Chem. Phys.*, 46:2162, 1967.
- [69] D.D. Delannoy, B. Tribollet, F. Valadier, and A. Erbeia. *J. Chem. Phys.*, 68:2252, 1978.
- [70] D.M. Lindsay. *J. Chem. Phys.*, 81:3356, 1984.
- [71] J. Eloranta, K. Vaskonen, H. Hakkanen, T. Kiljunen, and H. Kunttu. *J. Chem. Phys.*, 109:7784, 1998.
- [72] C. Kittel and E. Abrahams. *Phys. Rev.*, 90:238, 1953.
- [73] M. Peyron and H.P. Brioda. *J. Chem. Phys.*, 30:139, 1959.
- [74] H.P. Brioda and M. Peyron. *J. Chem. Phys.*, 32:1068, 1960.
- [75] V.V. Khmelenko, A.A. Pelmenev, I.N. Krushinskaya, I.B. Bykhalo, R.E. Boltnev, and D.M. Lee. *J. Low Temp. Phys.*, 171:302, 2013.

- [76] E.B. Gordon. *Low Temp. Phys.*, 30:756, 2004.
- [77] J. Schmidt and J.H. Van der Waals. *J. Low Temp. Phys.*, 2:8, 1968.
- [78] E.R. Glaser, T.A. Kennedy, H.C. Crookham, J.A. Jr. Freitas, M. Asif Khan, D.T. Olsen, and J.N. Kuznia. *Appl. Phys. Lett.*, 63:19, 1993.
- [79] A. Gruber, A. Drabenstedt, C. Tietz, L. Fleury, J. Wrachtrup, and von Borczykowski. *Science*, 276:2012, 1997.
- [80] H. Tsuruta, T. Miyazaki, and N. Azuma. *J. Phys. Chem.*, 87:5422, 1983.
- [81] T. Kumada. *Phys. Rev. B*, 68:052301, 2003.
- [82] T. Miyazaki. *Atom Tunneling Phenomena in Physics, Chemistry and Biology, Springer Series on Atomic, Optical and Plasma, Vol. 36 (Springer, Berlin, 2004)*.
- [83] J. Ahokas, J. Jarvinen, V.V. Khmelenko, and D.M. Lee. *Phys. Rev. Lett.*, 97:095301, 2006.
- [84] J. Ahokas, O. Vainio, J. Jarvinen, V.V. Khmelenko, D.M. Lee, and S. Vasiliev. *Phys. Rev. B*, 79:220505, 2009.
- [85] J. Ahokas, O. Vainio, S. Novotny, J. Jarvinen, V.V. Khmelenko, D.M. Lee, and S. Vasiliev. *Phys. Rev. B*, 81:104516, 2010.
- [86] J. Jarvinen, V.V. Khmelenko, D.M. Lee, J. Ahokas, and S. Vasiliev. *J. Low Temp. Phys.*, 162:96, 2011.
- [87] E.P. Bernard, R.E. Boltnev, V.V. Khmelenko, V. Kiryukhin, S.I. Kiselev, and D.M. Lee. *Phys. Rev. B*, 69:104201, 2004.
- [88] G. Breit and I.I. Rabi. *Phys. Rev.*, 38:2082, 1931.
- [89] G.T. Trammell, H. Zeldes, and R. Livingston. *Phys. Rev.*, 110:630, 1958.
- [90] T. Miyazaki. *J. Phys. Chem.*, 94:1702, 1990.
- [91] A.V. Ivliev. *JETP Lett.*, 38:379, 1983.
- [92] T. Miyazaki. *J. Phys. Chem.*, 88:4959, 1984.
- [93] R.N. Porter and M. Karplus. *J. Phys. Chem.*, 40:1105, 1964.
- [94] T. Takayanagi et al. *J. Phys. Chem.*, 86:6133, 1987.
- [95] Takayanagi T., K. Nakamura, and S. Sato. *J. Phys. Chem.*, 90:1641, 1989.
- [96] Takayanagi T. and S. Sato. *J. Phys. Chem.*, 92:2862, 1990.
- [97] G.C. Hancock, C.A. Mead, D.G. Truhlar, and A.J.C. Vandas. *J. Phys. Chem.*, 91:3492, 1989.

- [98] V. Engel, R. Schinike, and E. Pollak. *J. Phys. Chem.*, 87:1596, 1987.
- [99] B. Liu. *J. Phys. Chem.*, 58:1925, 1973.
- [100] B.C. Garrett and D.G. Truhlar. *J. Phys. Chem.*, 83:1079, 1979.
- [101] T. Miyazaki, N. Iwata, K. Lee, and K. Fueki. *J. Phys. Chem.*, 93:3352, 1989.
- [102] A.S. Iskovskikh, A.Y. Katunin, I.I. Lukashevich, V.V. Sklyarevskii, V.V. Suraev, V.V. Filippov, N.I. Filippov, and V.A. Shevtsov. *Sov. Phys. JETP*, 64:1085, 1986.
- [103] P. Kusch. *Phys. Rev.*, 100:1188, 1955.
- [104] R. Beringer and M.A. Heald. *Phys. Rev.*, 95:1474, 1954.
- [105] C.K. Jen, S.N. Foner, E.L. Cochran, and V.A. Bower. *Phys. Rev.*, 104:846, 1956.
- [106] S.N. Foner, E.L. Cochran, V.A. Bower, and C.K. Jen. *J. Chem. Phys.*, 32:963, 1960.
- [107] A.S. Iskovskikh, A.Y. Katunin, I.I. Lukashevich, V.V. Sklyarevskii, and V.A. Shevtsov. *JETP Lett.*, 42:30, 1985.
- [108] T. Miyazaki, H. Morikita, K. Fueki, and T. Hiraku. *Chem. Phys. Lett.*, 182:35, 1991.
- [109] K. Vaskonen, J. Eloranta, T. Kiljunen, and H. Kunttu. *J. Chem. Phys.*, 110:2122, 1999.
- [110] W. Gordy and R. Morehouse. *Phys. Rev.*, 151:207, 1966.
- [111] A.G. Prodel and P. Kusch. *Phys. Rev.*, 88:184, 1952.
- [112] C.K. Jen, S.N. Foner, E.L. Cochran, and V.A. Bowers. *Phys. Rev.*, 112:1169, 1958.
- [113] M. Sharnoff and P.V. Pound. *Phys. Rev.*, 132:1003, 1963.
- [114] L.B. Knight, W.E. Rice, L. Moore, E.R. Davidson, and R.S. Daily. *J. Chem. Phys.*, 109:1409, 1998.
- [115] B.C. Crooker, B. Hebral, E.N. Smith, Y. Takano, and J.D. Reppy. *Phys. Rev. Lett.*, 51:666, 1983.
- [116] J.D. Reppy, B.C. Crooker, B. Hebral, A.D. Corwin, J. He, and G.M. Zassenhaus. *Phys. Rev. Lett.*, 84:2060, 2000.
- [117] E.B. Gordon. *Dokl. Phys. Chem.*, 378:156, 2001.
- [118] V.V. Khmelenko, D.M. Lee, and S. Vasiliev. *J. Low Temp. Phys.*, 162:105, 2011.
- [119] T. Kumada. *J. Chem. Phys.*, 124:094504, 2006.

- [120] T. Kumada, M. Sakakibara, T. Nagasaka, H. Fukuta, J. Kumagai, and T. Miyazaki. *J. Chem. Phys.*, 116:1109, 2002.
- [121] V. Shevtsov, A. Scherbakov, P. Malmi, E. Ylinen, and M. Punkkinen. *J. Low Temp. Phys.*, 104:211, 1996.
- [122] T. Kumada, S. Mori, T. Nagasaka, J. Kumagai, and T. Miyazaki. *J. Low Temp. Phys.*, 122:265, 2001.
- [123] R.A. Zhitnikov, Yu.A. Dmitriev, and M.E. Kaimakov. *Fizika Nizkikh Temperatur*, 15:367, 1989.
- [124] B.R. Johnson, J.S. Denker, N. Bigelow, L.P. Levy, J.H. Freed, and D.M. Lee. *Phys. Rev. Lett.*, 52:1508, 1984.
- [125] S. Sheludiakov, J. Ahokas, O. Vainio, J. Jarvinen, D. Zvezdov, V.V. Vasiliev, S. Khmelenko, S. Mao, and D.M. Lee. *Rev. Sci. Instrum.*, 85:053902, 2014.